論文 / 著書情報
Article / Book Information

題目(和文)	Si母材中自己組織化Ge量子ドットの作製と太陽電池応用
Title(English)	Fabrication of Self-organized Ge Quantum Dot in Si Matrix and its Application to Solar Cells
著者(和文)	後藤和泰
Author(English)	Kazuhiro Gotoh
出典(和文)	学位:博士（工学）, 学位授与機関:東京工業大学, 報告番号:甲第10180号, 授与年月日:2016年3月26日, 学位の種別:課程博士, 審査員:近藤 道雄,小田原 修,吉本 護,和田 裕之,半那 純一
Citation(English)	Degree:, Conferring organization: Tokyo Institute of Technology, Report number:甲第10180号, Conferred date:2016/3/26, Degree Type:Course doctor, Examiner:,,,,
学位種別(和文)	博士論文
Type(English)	Doctoral Thesis

Doctoral Thesis

Fabrication of Self-organized Ge Quantum Dot in Si Matrix and its Application to Solar Cells

Kazuhiro Gotoh

Department of Innovative and Engineered Materials

Tokyo Institute of Technology

March 2016

Preface

Photovoltaics utilizing solar cells are much effective to reduce green-house gases such as CO_2 as well as to improve energy self-sufficiency. Soar cell is a key device in solar photovoltaics and its conversion efficiency from sun light to electricity is the most important factor. There have been extensive studies to achieve higher efficiency utilizing a variety of materials and device structures. At present, crystalline silicon solar cells account for the most of market. Recently, the record conversion efficiency of 25.6% has been realized for heterojunction Si solar cells. Its value is close to theoretical limit of about 29%. To overcome this limit, multi-junction solar cells are needed with a combination of different band gap materials. However, high efficiency multi-junction solar cells over 30% mostly employ precious and rare elements such as Ga, Ge and In to result in 100 times more expensive cost as compared to silicon solar cells. Alternative ideas such as intermediate band solar cells using quantum dots have been proposed. For application to the IBSCs, it is desirable to prepare dense and uniform QDs with short inter-dot spacing in direction to photo-current. So far, many studies have been conducted for realization of the QD-IBSCs based on self-assembled quantum dots using III-V compound semiconductors, however there are not enough evidences to prove the concept of QD-IBSCs. Therefore, fundamental approach to understand mechanism of QDSCs is needed by means of comprehensive study upon fabrication of the QD structure, characterization of material, and its solar cell applications.

There have been a few reports on the QDSCs employing IV group semiconductors. Self-assembled Ge/Si QDs have interesting features for application to solar cells as follows. Both Ge and Si are indirect gap semiconductors, which leads to charge carrier separation in reciprocal space, i.e. *k* space. Furthermore, Ge/Si heterointerface shows type-II band lineup, which results in charge carrier separation in real space. Hence, Ge/Si QDSCs are expected to improve carrier collection efficiency.

With these backgrounds in mind, our purpose is growth of multi-stacked Ge QDs with high uniformity and density as well as short inter-dot spacing, and application of the Ge QD structure to solar cells.

This thesis consists of 8 chapters: (i) chapter 1 “General Introduction”, (ii) chapter 2 “Experimental”, (iii) chapter 3 “Single Layer Ge QDs on Si”, (iv) chapter 4 “Multi-stacked Ge QDs in Si Matrix”, (v) chapter 5 “Ge QDs in $Si_{1-x}C_x$ Matrix for Strain Compensation”, (vi) chapter 6 “Application of Multi-stacked Ge QDs to Solar Cells”, (vii) chapter 7 “General Discussion”, (viii) chapter 8 “General Conclusion”.

In chapter 1 “General Introduction”, backgrounds and purposes of this study are described.

In chapter 2 “Experimental”, brief explanation of equipment for growth and characterization are provided. Furthermore, growth procedures for Ge QDs and fabrication procedures for Ge QDSCs are given.

In chapter 3 “Single Layer Ge QDs on Si”, study on growth of Ge/Si QDs is described to achieve dense and uniform QDs. By employing both low temperature of 500 °C and high deposition rate of 0.28 nm/s, Ge QDs with high density of $\sim 5 \times 10^{10}$ cm^{-2} and better uniformity of 11% were grown due to suppressed surface migration of Ge adatoms.

In chapter 4 “Multi-stacked Ge QDs in Si Matrix”, Fabrication of multi-stacked Ge/Si QDs is described. By employing pulse growth technique consisted of high deposition rate of 0.28 nm/s and growth interruption of 5 seconds, highly-stacked Ge/Si QDs with 30 nm-thick spacer layer were fabricated up to 100-layer-stacked thank to weak strain fields induced by QDs.

In chapter 5 “Ge QDs in $Si_{1-x}C_x$ Matrix for Strain Compensation”, study on fabrication of $Ge/Si_{1-x}C_x$ QDs is shown to realize short inter-dot spacing. 20-layer-stacked $Ge/Si_{1-x}C_x$ QDs with spacer layer thickness of 6 nm were fabricated without generation of aggregated Ge islands.

In chapter 6 “Application of multi-stacked Ge QDs to solar cells”, the Ge QDs are applied to solar cells. Extended external quantum efficiency up to 1300 nm were observed for 100-layer-stacked Ge/Si

QDSCs, however properties of the QDSCs became worse due to increased recombination, because both stronger PL emission and worse transport properties were observed with increase in number of stacks. Better transport property was obtained in 50-layer-stacked Ge/$Si_{0.9995}C_{0.0005}$ QDs possibly due to improvement of suppressed recombination in Ge QDs. Furthermore, effect of spacer layer thickness on the properties of 20-layer-stacked Ge/$Si_{0.9995}C_{0.0005}$ QDSCs was investigated. The properties were not strongly affected by inter-dot spacing probably due to weak absorption process using energy levels of Ge QDs and dominant recombination process in Ge QDs.

In chapter 7 “General Discussion”, results in this thesis are summarized and discussion of this thesis is described. Employing low growth temperature and high deposition rate help to grown dense and uniform Ge QDs due to suppressed migration of Ge adatoms. Furthermore, utilization of $Si_{0.9995}C_{0.0005}$ spacer layer suppresses aggregation of Ge QDs in spacer layer thickness of 6 nm, however QD size become larger. Further effort is necessary to prevent strain filed created by each QDs from overlapping. Inserting Ge QD layers in p-n junction of solar cells makes recombination of photo-generated carriers dominant and thus solar cells properties become worse.

In chapter 8 “General Conclusion”, conclusion of this thesis is described. Employing low growth temperature and high deposition rate help to grow dense and uniform Ge QDs due to suppressed surface migration of adatoms. Furthermore, utilization of $Si_{0.9995}C_{0.0005}$ spacer layer prevents Ge QDs from generation of aggregated Ge islands in spacer layer thickness of 6 nm due to weaker strain fields induced by smaller QDs and slightly compensated strain fields. The performance of the solar cells inserting Ge QD layers becomes worse due to increase in recombination in Ge QDs. So, utilizing down or up convertor has possibility to improve conversion efficiency significantly.

Contents

Chapter 1. General Introduction

In this chapter, backgrounds, significance and purpose of this study are given. Physics of conventional solar cells are briefly explained first and next new concept solar cells using quantum dots are concisely described. Then, purpose of this work is described.

1.1. Solar Photovoltaics

Solar photovoltaics have been much attractive for sustainable development and prevention of global warming because solar photovoltaics are able to convert solar energy to electricity without consuming fossil fuels in operation. Carbon dioxide (CO_2) is a representative green-house gas originated from fossil fuels. Table 1.1 summarizes the CO_2 emission amount of power generation methods in Japan. The photovoltaics are possible to reduce CO_2 emission efficiently. Furthermore, the photovoltaics are capable of improving energy self-sufficiency since the solar energy is provided whole countries although it depends on latitude, which is different from fossil fuels. Moreover, solar energy is enormous and inexhaustible. Total solar energy coming to the earth is equivalent to electric power of about 1×10^{14} kW, while human beings consume the total electric power of order of 10^{11} kW per year. For this striking feature, research and development of solar photovoltaics are very important for humanity and the countries which possess few energy resources.

Table 1.1: CO_2 emission amount for power generation methods in Japan [1].

Power generation methods	CO_2 emission amount
Total electric power	360 g/kWh
Thermal power generation (fossil fuels)	690 g/kWh
Photovoltaics	17-48 g/kWh

Basic component of solar photovoltaics is solar cells which convert solar energy to electric energy. This energy conversion in solar cells is mainly composed of three successive processes: charge carrier generation, charge carrier separation and charge carrier transport. For realization of these processes in a device, structure of the conventional single junction solar cells illustrated in Fig.1.1 is developed. Solar cells generally consist of light absorbing materials and metal electrodes. In general, p-n junction of same semiconductor is widely used as light absorbing materials for collection of photo-generated charge carriers.

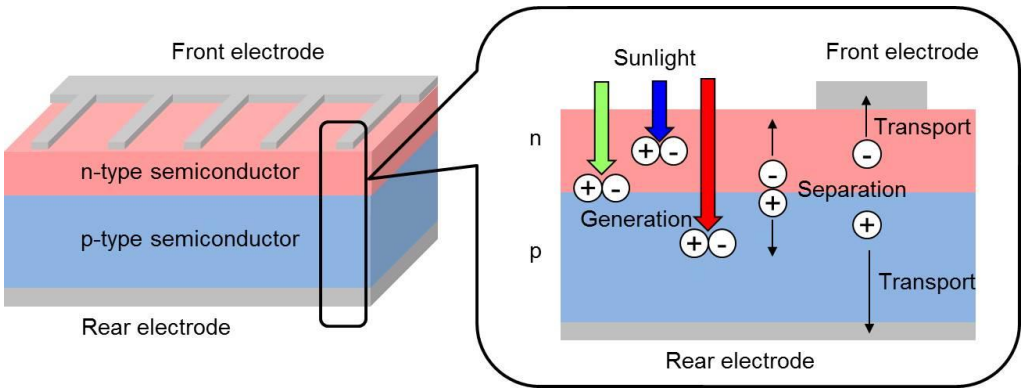

Fig. 1.1: Structure of typical single junction solar cells and successive processes in the solar cells.

1.2 Solar Cells

Semiconductors have their own energy gap and the energy gap dominates absorption of the light and electron-hole pairs are generated by photons with energy larger than the energy gap. The electrons and holes are spatially separated by electric fields established by p-n junction. In this section, physics of solar cells are provided. In particular, silicon is focused on as a semiconductor material because silicon is a mainly used material in solar cells.

1.2.1 Semiconductors

Semiconductors have inherent band gap between valance band (VB) and conduction band (CB) as a results of interaction of electron wave function. Figure 1.2 shows a schematic band diagram of semiconductors. The VB is the lower energy states occupied by electrons, while the CB is the higher energy states unoccupied by electrons. For this energy structure, electrons are excited from VB to CB and holes are generated in VB when a semiconductor is irradiated by light with energy higher than the band gap energy (E_g) between CB minimum (CBM) and VB maximum (VBM). The E_g of semiconductors are about 1-3 eV, which is appropriate to absorb visible photons from the sun since the photons reaching the earth is mainly composed of visible photons. The E_g of representative semicondustors are summarized in Table 1.2. Figure 1.3 shows the solar spectrum under Air Mass 1.5 (AM 1.5) condition. The AM is a factor considering attenuation of sun light by the atmosphere and it depends on attitude. The AM 1.5 corresponds to the sun being at an angle of elevation of 42°. The solar spectrum refers to the data provided by National Renewable Energy Laboratory (NREL) in USA [3].

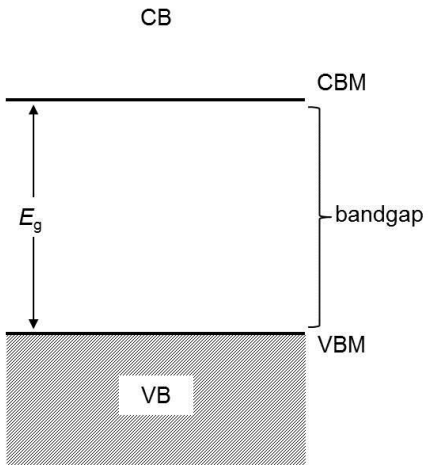

Fig. 1.2: Band diagram of semiconductors.

Table 1.2: Band gap energy of representative semiconductors [2].

Semiconductors	Si	Ge	GaAs	InP	InAs	CdTe	GaN
E_g [eV]	1.12	0.66	1.42	1.35	0.36	1.56	3.44

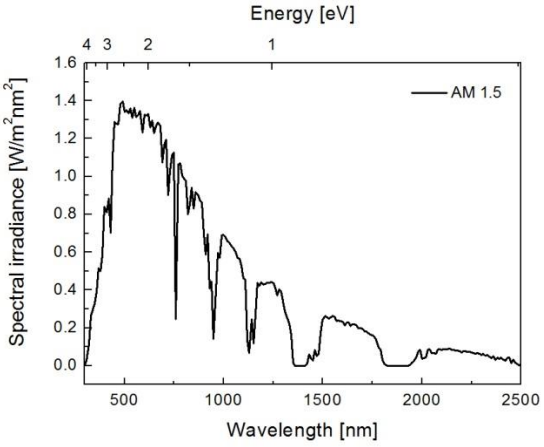

Fig. 1.3: Solar spectrum under Air Mass 1.5 [3].

1.2.2. Intrinsic and impurity doped semiconductors

An n-type semiconductor and a p-type semiconductor are prepared by doping impurities into the intrinsic semiconductor which is high purity semiconductor. Figure 1.4 schematically shows three basic bond representations of intrinsic, n-type and p-type. In intrinsic silicon, four valence electrons are shared with the four neighboring silicon atoms by each silicon atom, which leads to formation of four covalent bonds. The Fermi energy indicating the probability of electron is 1/2 lies close to middle of bandgap for intrinsic semiconductors. For n-type semiconductors, majority carrier is the electron due to donor impurities and thus the Fermi energy lies close to conduction band. For p-type semiconductor, major carrier is the hole and hence the Fermi energy level lies close to valence band. The position of fermi energy is summarized in Fig. 1.5.

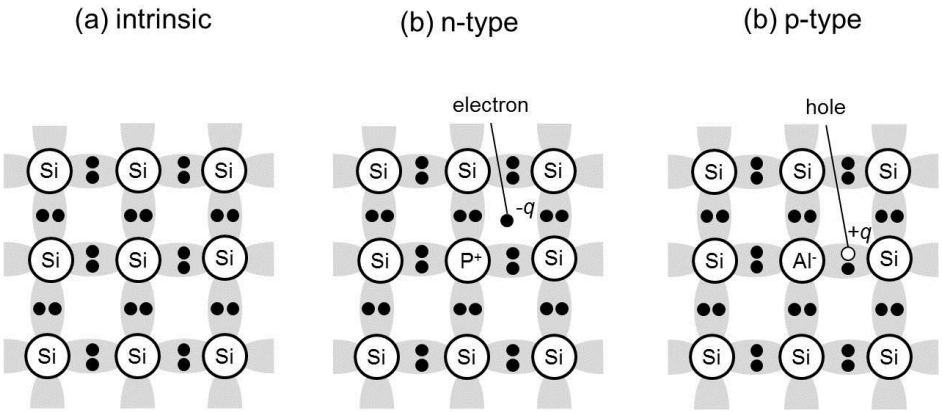

Fig. 1.4: Bond representations of (a) intrinsic, (b) n-type and (c) p-type semiconductors.

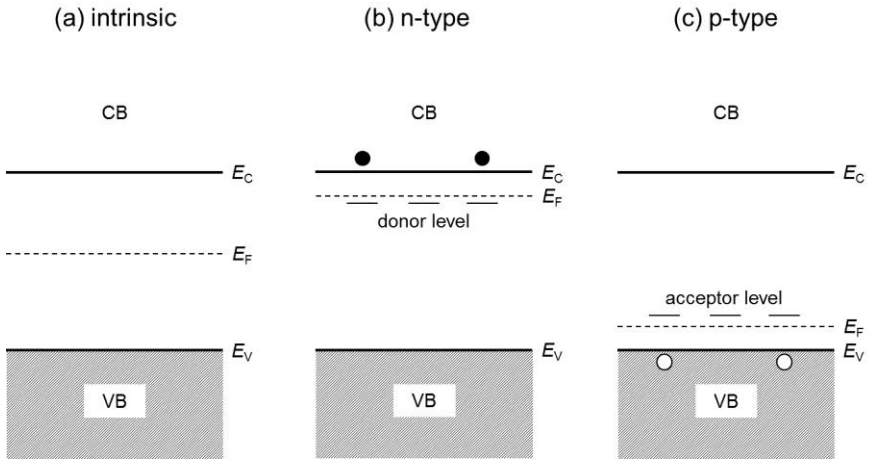

Fig. 1.5: Position of Fermi energy (E_F) and impurity levels in (a) intrinsic, (b) n-type and (c) p-type semiconductors. The CBM and VBM is illustrated as E_C and E_V, respectively.

1.2.3. P-N junction

The p-n junction is formed by doping different regions of the same semiconductor, which means that an interface between p-type and n-type layers is created in the same semiconductor. Electric field is established at the p/n interface, so called built-in potential, since Fermi energy level must be identical in the semiconductor under equilibrium. The built-in potential V_{bi} is determined by the differences in work functions of the n-type Φ_n and p-type semicondutors Φ_p, i.e. $V_{bi} = (\Phi_n - \Phi_p)/q$. In general, the V_{bi} depends on doping concentration of each layer. Figure 1.6 shows the band profile of (a) before and (b) p-n junction in equilibrium. The V_{bi} established at p-n junction drives the photo-generated electrons and holes towards n-type and p-type semiconductor, respectively.

Figure 1.7 shows the operation principal of the basic solar cells using p-n junction. Electrons and holes are created by absorbing photons with larger energy than E_g. Then, the electrons and holes are separated and head for n-layer and p-layer, respectively. As a consequence of higher population of photo-generated electrons and holes in n-layer and p-layer, respectively, the quasi Fermi energy is introduced in each layer. Therefore, voltage is created in solar cells between n-layer and p-layer the

solar cells under light illumination and it principally depends on the difference in quasi Fermi energy of n-layer and p-layer, i.e. bandgap energy and doping concentration.

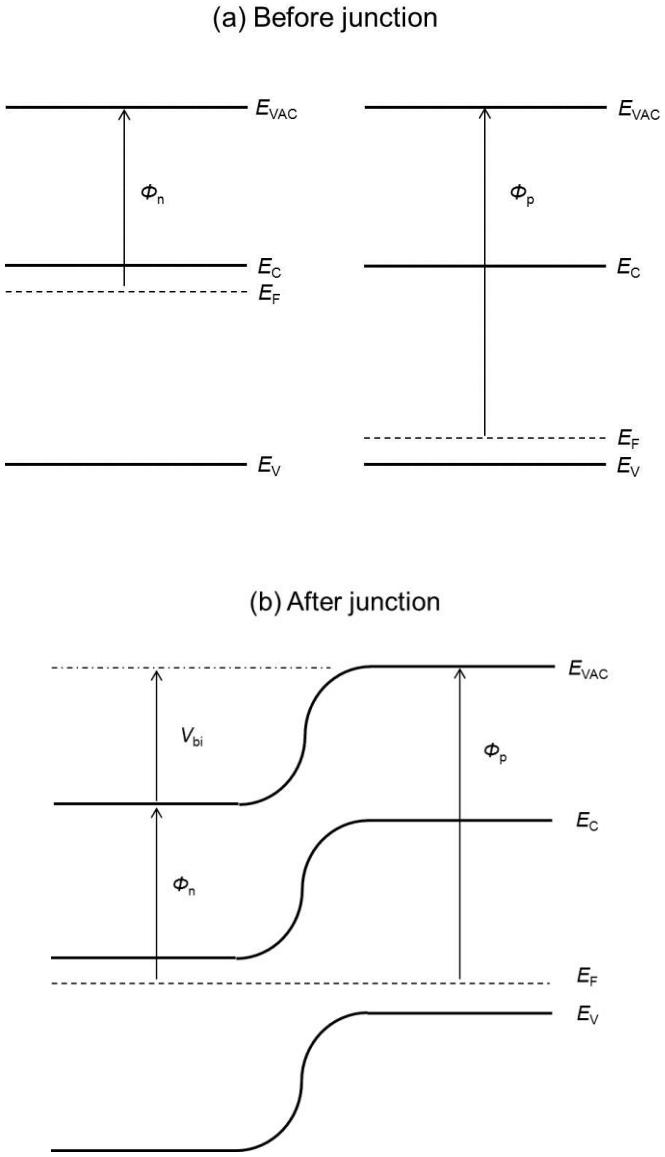

Fig. 1.6: Band profile of (a) before and (b) after p-n junction in equilibrium.

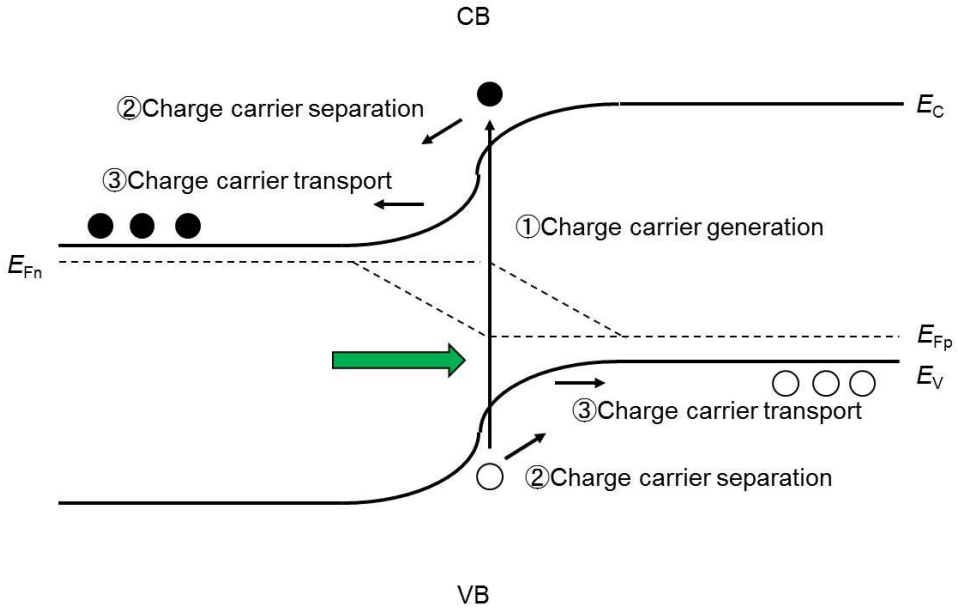

Fig. 1.7: Operation principal of basic solar cells using p-n junction.

1.2.4. Parameters of solar cells

As mentioned above, p-n junction of semiconductors is most widely used in solar cells since it is able to achieve charge carrier generation, charge carrier separation and charge carrier transport. The key parameters of a solar cell are short-circuit current density (J_{SC}), open circuit voltage (V_{OC}), fill factor (FF) and conversion efficiency (η). The J_{SC} is the photo-current density generated by a solar cell under illumination under short-circuit condition. The schematic energy band diagram of solar cells in short-circuit is shown in Fig. 1.8 (a). The J_{SC} is given by following equation.

$$J_{sc} = q \int b_s(E)\mathrm{QE}(E)dE$$

The q, $b_s(E)$ and QE(E) are the electronic charge, the incident spectral photon flux density of and the quantum efficiency, respectively. The quantum efficiency QE(E) is given by product of the absorption and collection efficiencies. The V_{OC} is the voltage of a solar cell generated by a solar cell under illumination under open circuit condition and described as follows

$$V_{\mathrm{oc}} = \frac{kT}{q} \ln\left(\frac{J_{\mathrm{sc}}}{J_0} + 1\right)$$

, where k is Boltzmann's constant, T is temperature and J_0 is a constant, respectively. The schematic energy band diagram of solar cells in open circuit is given in Fig. 1.8 (b). In operation, the power density P is given by

$$P = JV$$

, where J is current density and V is voltage of a solar cell. P becomes maximum at operating point (current density of J_{m} and voltage of V_{m}). The FF is defined as ratio

$$\mathrm{FF} = \frac{J_{\mathrm{m}} V_{\mathrm{m}}}{J_{\mathrm{sc}} V_{\mathrm{oc}}}$$

and indicates quality of p-n junction. The conversion efficiency of solar cells η is defined as

$$\eta = \frac{J_{\mathrm{m}} V_{\mathrm{m}}}{P_{\mathrm{s}}} = \frac{J_{\mathrm{sc}} \cdot V_{\mathrm{oc}} \cdot \mathrm{FF}}{P_{\mathrm{s}}}$$

, where P_{s} is the incident light power density. The typical current-voltage (J-V) curves of a solar cell under illumination are given in Fig. 1.9.

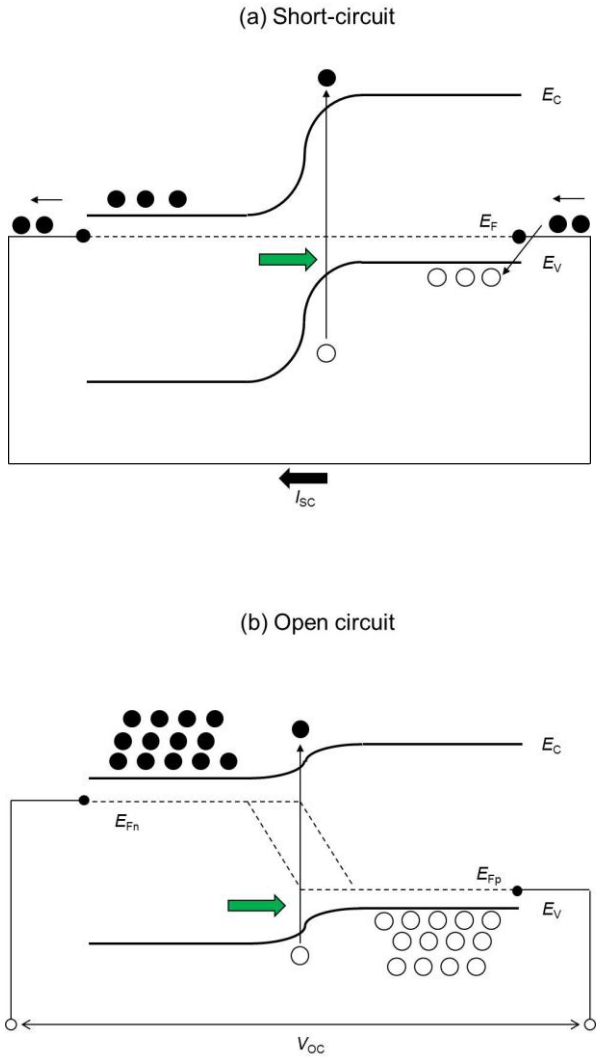

Fig. 1.8: Energy band diagram of solar cells at (a) short circuit and (b) open circuit.

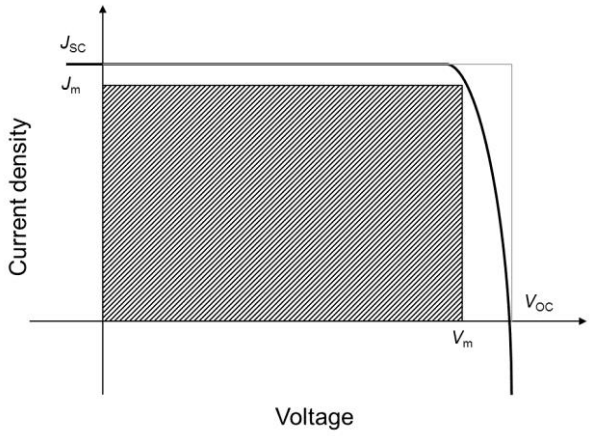

Fig. 1.9: *J-V* curve of a solar cell under illumination.

The equivalent circuit of a solar cell is illustrated in Fig.1.10. The solar cell is equivalent to a current generator with a diode, series resistance and parallel resistance. The power generator produces photocurrent depending on light intensity (I_{SC}). The diode generate dark current (I_{dark}) and related to minority carriers recombination in the solar cell. The series resistance (R_s) is caused from the resistance of the cell material and the electrode contacts, which affect carrier transport. The parallel resistance termed as shunt resistance (R_{sh}) arises from leakage of current in the solar cells at surface or p-n junction. The output current of the equivalent circuit is described as following equation

$$I = I_{sc} - I_0 \left\{ \exp\left(\frac{q(V + R_s I)}{nkT} \right) - 1 \right\} - \frac{V + R_s I}{R_{sh}}$$

, where V is the output voltage, q is elementary charge, n is the diode factor, k is Boltzmann constant and T is temperature. The effect of resistivity of R_s and R_{sh} are shown in Fig. 1.11. The I_{SC} and FF decrease with increasing the resistivity of $R_{s,}$ while the V_{OC} and FF decrease with increasing the resistivity of R_{sh}. For higher conversion efficiency, the value of I_0 and R_s should be small, and that of R_{sh} should be larger.

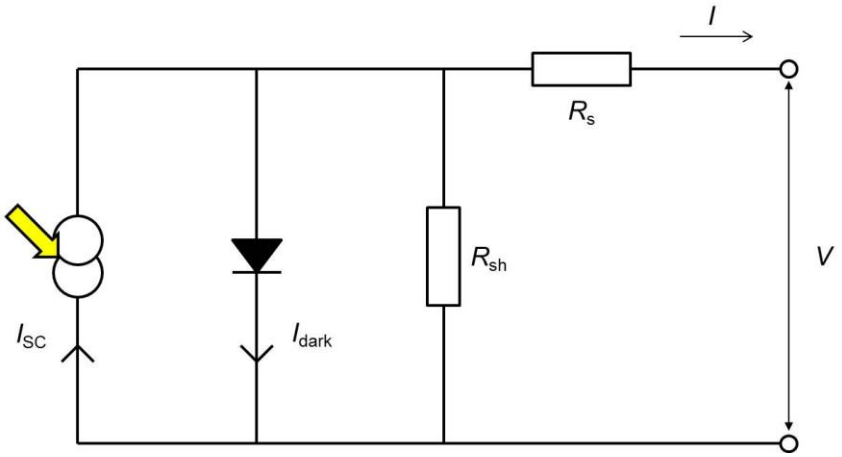

Fig. 1.10: Equivalent circuit of a solar cell

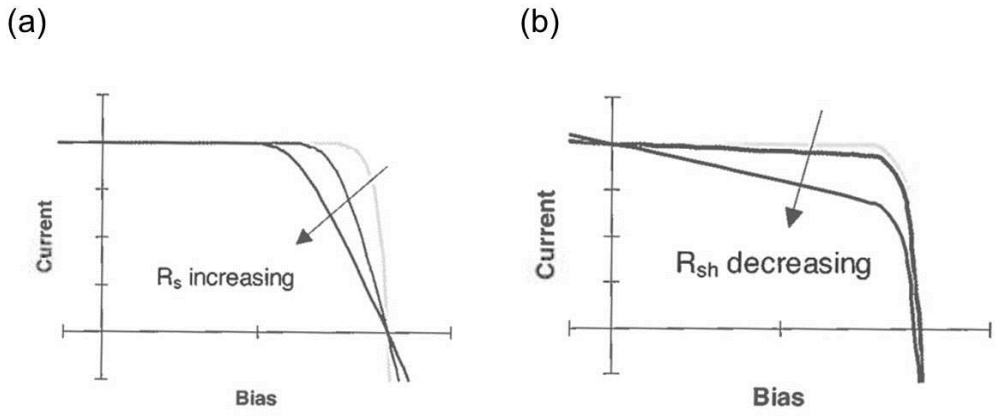

Fig. 1.11: Effect of (a) increasing series and (b) decreasing shunt resistances [4].

1.2.5. Heterojunction solar cells

In typical heterojunction Si solar cells, p-n junction is formed by deposition of hydrogenated amorphous Si (a-Si:H) on crystalline Si (c-Si) and thin i-type a-Si:H is inserted between doped a-Si:H and c-Si. Figure 1.12 shows schematic structure of double heterojunction solar cells. In general, n-type c-Si substrates are used. For front side, i-type a-Si:H and p-type a-Si:H are formed on the Si substrates. Similarly, i-type and n^+-type a-Si:H are deposited on rear side of the Si substrates. The i-type a-Si:H reduce surface recombination due to effective passivation of surface states and therefore higher V_{oc} is obtained [5-7]. The n^+-type a-Si:H create potential barrier for holes and suppress carrier recombination at back surface of c-Si, so called back surface fields (BSF). Transparent conductive oxide (TCO) layer and metal contact are fabricated on the a-Si:H deposited on c-Si substrate.

Figure 1.13 shows energy band diagram of heterointerface at a-Si:H/c-Si. Band discontinuity accrues at heterointerface because bandgap energy of a-Si:H is larger than that of c-Si. Hence, the conduction band offset ΔE_C and valence band offset ΔE_V are created in conduction band and valence band edges, respectively. The value of band offset is determined by electron affinity and bandgap

energy of each semiconductor. The band offsets reflect minority carriers away from the surface and hence recombination at surface is suppressed.

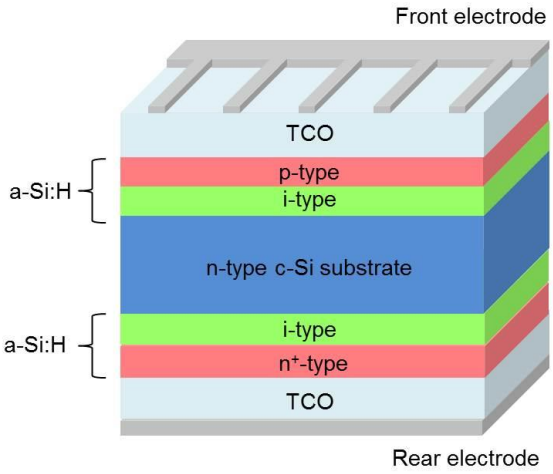

Fig. 1.12: Schematic structure of heterojunction Si solar cells.

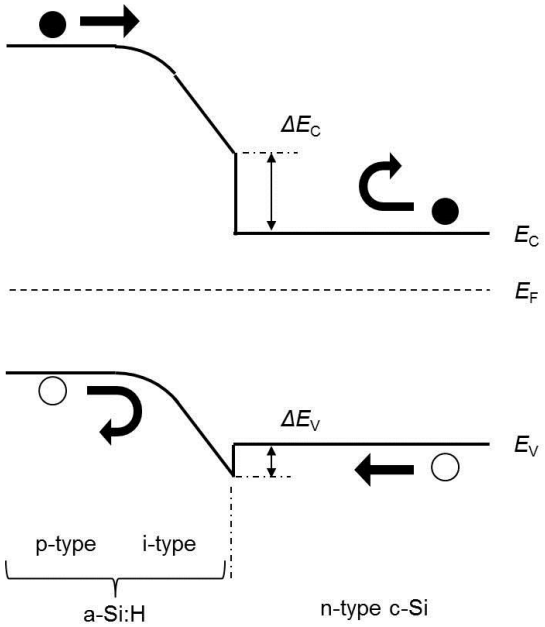

Fig. 1.13: Energy band diagram of heterointerface at a-Si:H/c-Si.

1.2.6. Limiting efficiency

The conversion efficiency is principally dependent on bandgap energy of semiconductors (E_g). Figure 1.14 shows the dependence of theoretical conversion efficiency η and intrinsic loss on bandgap energy E_g. W. Shockley and H. J. Queisser calculated the theoretical conversion efficiency of solar cells by using the principal of detailed balance considering generation and radiative recombination of carriers between VB and CB [8]. Generally, small band gap energy leads to large J_{sc} and small V_{oc}, while large band gap energy results in small J_{sc} and large V_{oc} due to transmission of lower energy photons and thermalization of photo-generated carriers by higher energy photons than E_g. Semiconductors are not able to absorb lower energy photons than E_g, which limits current density owing to decrease in photo-generated carriers. Furthermore, charge carriers generated by higher energy photons than E_g relax to the band edges quickly by losing excess energy as heat, which limits voltage. Therefore, the η become maximum at E_g of around 1.4 eV. In 2015, the conversion efficiency of Si hetero junction solar cells is 25.6 %, which is close to theoretical conversion efficiency of ~30%. Further approaches are important to improve conversion efficiency significantly.

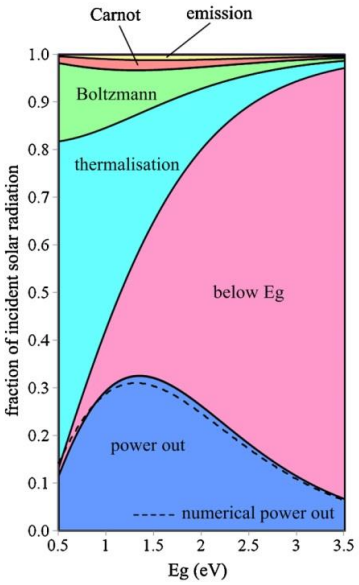

Fig. 1.14: Intrinsic power loss and power out of solar cells [9]. The power out corresponds to the conversion efficiency depending of E_g.

1.2.7. Multi-junction solar cells

To overcome the limiting efficiency, multi-junction solar cells have been developed. Multi-junction solar cells are multiply stacked solar cells possessing different bandgap energy [10]. In the multi-junction solar cells, solar cells with larger bandgap energy installed on solar cells with smaller bandgap energy by tunnel junction, and hence spectral mismatch loss is reduced. Figure 1.15 shows schematic illustration of triple junction solar cells. For example, triple junction solar cells are fabricated and it shows higher conversion efficiency of 41.1% under sun light concentration condition [11]. Although multi-junction solar cells are possible to improve conversion efficiency, a weak point of the multi-junction solar cells is connecting solar cells in series. If one in multi-junction solar cells is not able to generate charge carriers, for example, by weak sun light in cloudy sky, its resistivity increases and thus the conversion efficiency of multi-junction solar cells significantly decrease. Additionally, high efficiency multi-junction solar cells over 30 % mostly employ precious and rare elements such as Ga, Ge and In, which results in more expensive cost as compared to silicon solar cells.

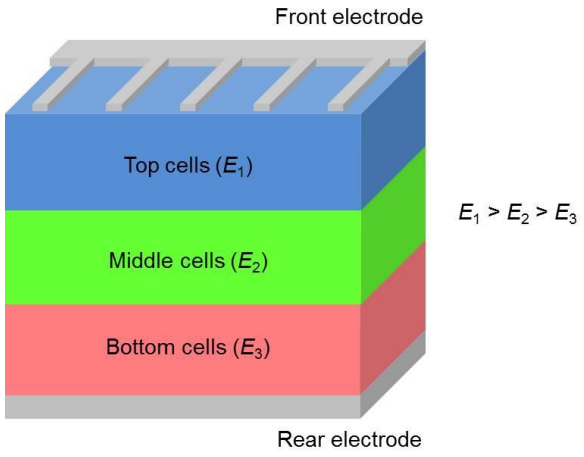

Fig. 1.15: Schematic of triple junction solar cells (bandgap energy $E_1 > E_2 > E_3$).

1.3. Intermediate Band Solar Cells

For overcoming the limiting efficiency of conventional single junction solar cells, solar cells utilizing intermediate state have been proposed, so called intermediate band solar cells (IBSCs) [12]. In this section, the IBSCs are briefly explained.

1.3.1. Concept of intermediate band solar cells

Intermediate band solar cells (IBSCs) were proposed to achieve significant improvement of conversion efficiency. Figure 1.16 shows the simplified energy band profile in IBSCs. In ideal IBSCs, two-step optical transition from VB to IB and IB to CB are utilized in addition to conventional transition from VB to CB, which leads to increase in J_{sc} thanks to enhancement of matching to solar spectrum. Furthermore, the V_{oc} is determined by incremental differences of quasi Fermi energy between CB and VB, i.e. E_{FC} minus E_{FV}. That means the IBSCs are expected to increase J_{sc} without significant decrease in V_{oc} in theory. The simplified equivalent circuit model of IBSCs is shown in Fig. 1.17. The circuit includes three current generators and three diodes. The diodes represent reverse current associated with photo-generated carrier recombination. The current generators and diodes represent the photocurrent generated by absorption and recombination in each transition, respectively. The transition from VB to CB and transition via IB are carried out in parallel, which results in parallel connection of CV cell with VI and IC cells. Thus, it is possible for the IBSCs to improve the problem of multi junction solar cells caused by series connection.

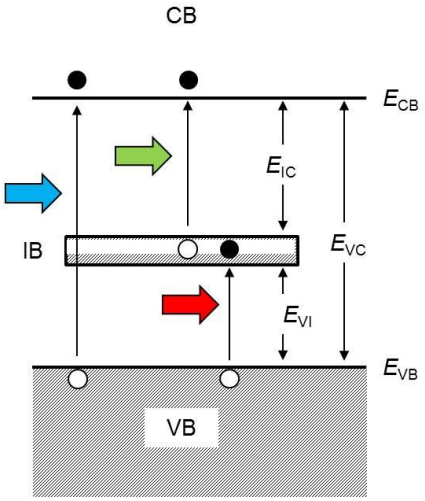

Fig. 1.16: Simplified energy band diagram of IBSCs.

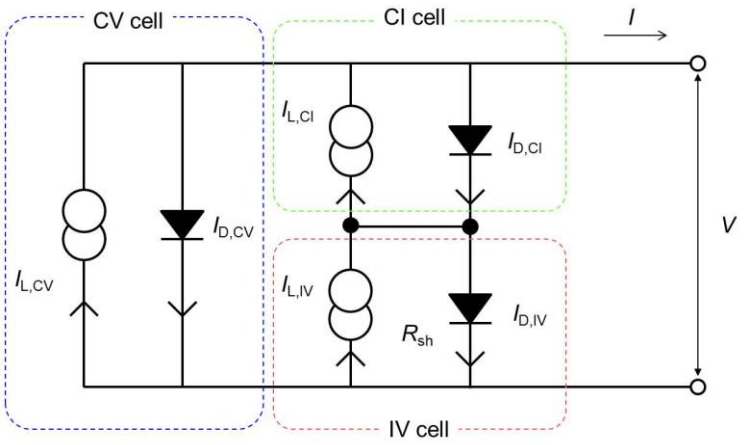

Fig. 1.17: Concise equivalent circuit model of IBSCs.

1.3.2. Limiting efficiency

Limiting efficiency of IBSCs is firstly calculated by A. Luque and A. Matin. Figure 1.18 shows the efficiency limit for solar cells with intermediate band. The calculation employed seven conditions: (I) nonradiative transitions between any two of three bands are prohibited, (II) carrier mobility is infinite, (III) no carriers can be extracted from IB, (IV) the solar cells is thick enough to absorb the photons with enough energy to induce any one of the transition, (V) a perfect mirror is assumed at back of the

solar cells, (VI) only one of the three absorption length is important for every range of energies, and (VII) the solar cell illumination is isotropic. By assuming so, total current of IBSCs (I_{Total}) is adding the current generated by transition between VB and CB (I_{VC}) and the current generated by transition between IB and CB (I_{IC}), that is $I_{Total} = I_{VC} + I_{IC}$. The I_{IC} is equal to the electron generated by transition between VB and IB (I_{IC}) due to preservation of number of electron in IB, which means $I_{IC} = I_{VI}$. Furthermore, the value of voltage in IBSCs is as same as that of the conventional single junction solar cells. It is determined the difference between chemical potential between CB and VB, i.e. the split between electron and hole quasi-Fermi energy levels.

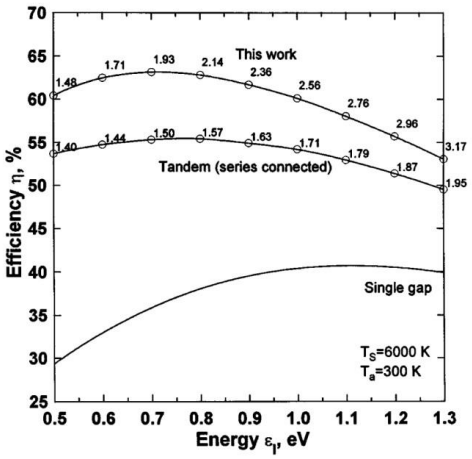

Fig. 1.18: Limiting efficiency of IBSCs [12]. “This work” indicates the efficiency limit of IBSCs.

1.4. Quantum Dot Intermediate Band Solar Cells

Quantum dot is a one of candidates to realize the IB state within the bandgap [13]. Concise features of the quantum dots and quantum dots solar cells (QDSCs) are presented in this section. The details of QDs are elaborated on in [14].

1.4.1. Quantum dots

Quantum dots (QDs) are the nanostructures of semiconductor materials exhibiting quantization effect as a result of confinement of charge carriers in small regions of three dimensional spaces by potential barriers. The term of nanostructure semiconductors depends on the dimensions of confinement. If the confinement is in one dimension, two dimensions and three dimensions, the nanostructure is termed as quantum wells, quantum wire and quantum dots, respectively. Figure 1.19 shows schematic images of quantum wells, quantum wire, quantum dot and each density of state in CB. The electrons and holes are able to move freely in respective bands in all three dimensions. The electrons in conduction band of bulk semiconductors are allowed to possess any energy above the band gap energy E_g and the density of states is proportional to $(E - E_g)^{1/2}$. In quantum well, electrons and holes are confined in one direction, which results in free movement in two directions. The density of state for quantum wells becomes step like function due to energy levels as a consequence of dimensional confinement. Similarly, it is possible for electrons and holes to move to one direction in quantum wire and zero direction in quantum dots. In quantum wire, the density of state depends on $E^{-1/2}$, which leads to peaks at each new quantized state. In case of quantum dots, the density of state indicates delta like function arisen from quantized motion in three dimensions, which means isolated energy levels are generated. For the features, quantum dots are regarded as ‘artificial atoms’.

The confinement of carriers is achieved by heterostructure of semiconductor materials. Figure 1.20 shows the heterostructure which semiconductor material 2 is sandwiched by semiconductor material 1 and the band lineup. Carriers are confined owing to band offset between material 1 and material 2.

When layer thickness of material 2 (d_2) is reduced to less than few tens of nm, quantized energy levels are created. The position of energy levels depends on valence band offset as well as width of well. For example of $Si/Si_{0.1}Ge_{0.9}$ quantum well, the quantum size effect become prominent when well width becomes less than about 10 nm [15]. Similarly, quantum dots are fabricated by heterostructure of semiconductors in three dimensions. The structure consists of quantum dots and matrix as show in Fig. 1.21 (a) and hence isolated energy levels from CB and VB are created within the bandgap in matrix semiconductor. The isolated energy levels are utilized as intermediate levels in IBSCs so quantum dots are promising candidates to realize IBSCs.

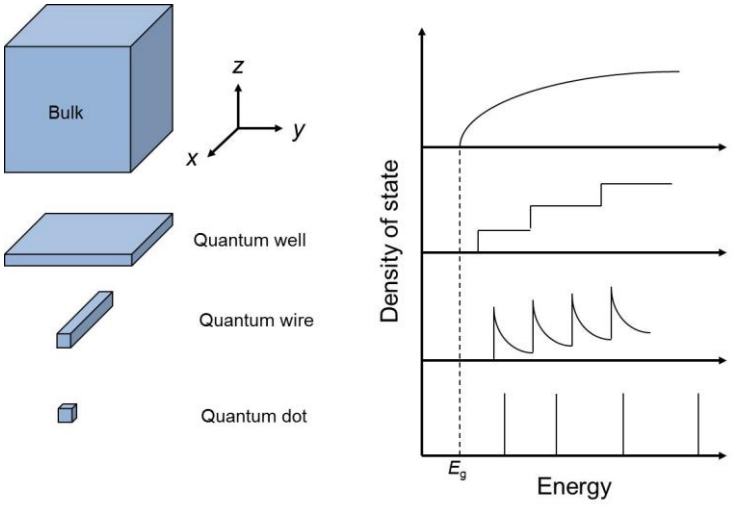

Fig. 1.19: Schematic images of bulk, quantum well, quantum wire, quantum dot and their density of state in CB.

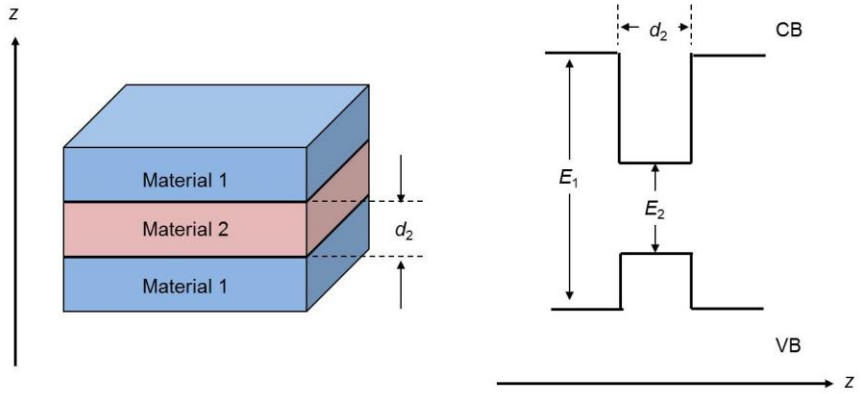

Fig. 1.20: Simplified images for hetero junction of semiconductor 1 (band gap energy: E_1) and semiconductor material 2 (band gap energy: E_2).

1.4.2. Quantum dot superlattice

Quantum dot superlattices (QDSLs) are the regularly arrayed QDs in there dimension. As mentioned above, the QDs resembles to atoms. Energy bands such as CB and VB in bulk are formed as a consequence of interaction between wave functions of valence electrons. Similarly, minibands are formed within the band gap due to interaction between wave function of QDs as shown in Fig. 1.21 (b). Inter-dot spacing is critical parameters for electrically coupled QDs, i.e. formation of the minibands. The formation of minibands is expected to be occurred when the inter-dot spacing is less than ~5 nm for In(Ga)As QDs in GaAs matrix [16,17], ~4 nm for InGaP QDs in InP matrix [18], and ~4 nm for Ge QDs in Si matrix [19-21]. Therefore, short inter-dot spacing is necessary to realize the minibands.

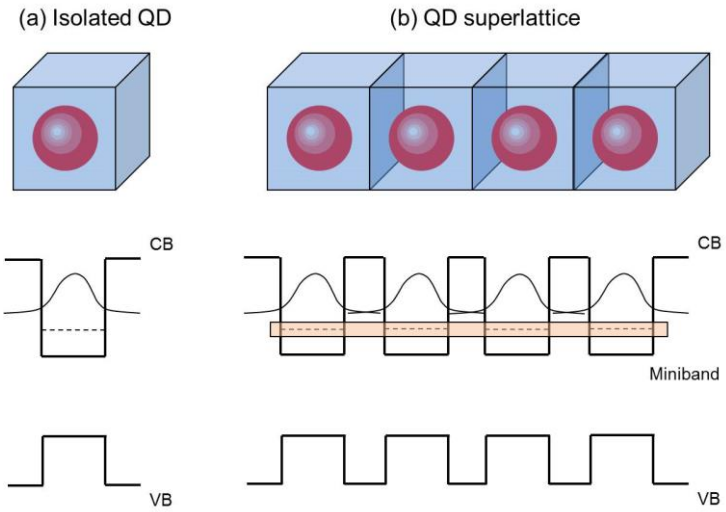

Fig. 1.21: Schematic images of (a) isolated QD and (b) QD superlattices and each band profile.

1.4.3. Quantum dot intermediate band solar cells

The minibands are utilized as IB states in quantum dot intermediate band solar cells (QD-IBSCs). The QDSLs are sandwiched by p and n-type semiconductors in QD-IBSC [22]. The schematic structure of QD-IBSCs is illustrated in Fig. 1.22 (a). Figure 1.22 (b) shows concise band profile of the QD-IBSCs using Ge QDs in Si matrix.

So far, self-assembled QDs using III-V semiconductor materials, mostly In(Ga)As/GaAs QDs, have been intensively studied for QD-IBSCs by several groups [23-29]. The short-circuit current density increase with increase in density of QD in matrix whereas the open circuit voltage decreased. Furthermore, some of them detected the two-step optical transition while the efficiency of QDSCs has not exceeded that of GaAs reference solar cells.

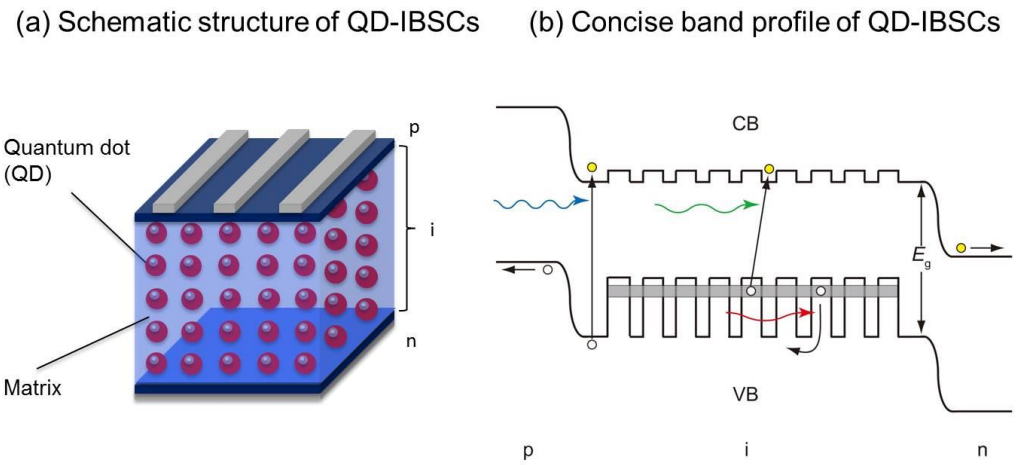

Fig. 1.22: (a) Schematic images of QD-IBSCs and (b) concise band profile of Ge/Si QD-IBSCs.

1.4.4. Ge/Si heterstructure

The Ge/Si QDs have some advantages for use in solar cells in comparison with In(Ga)As/GaAs QDs. Both Ge and Si are indirect gap semiconductors so the phonons are necessary for optical transition from VBM to CBM, which results in small absorption coefficient and longer radiative lifetime [30]. The simplified energy band structures of a direct gap semiconductor and indirect semiconductor are depicted in Fig. 1.23. In direct semiconductor, only photons involve the band to band optical transition. So, conservation of energy is demanded as follows

$$E_{\mathrm{f}} = E_{\mathrm{i}} + \hbar\omega$$

, where E_{i} and E_{f} are the energy of electron in VB and CB, respectively.

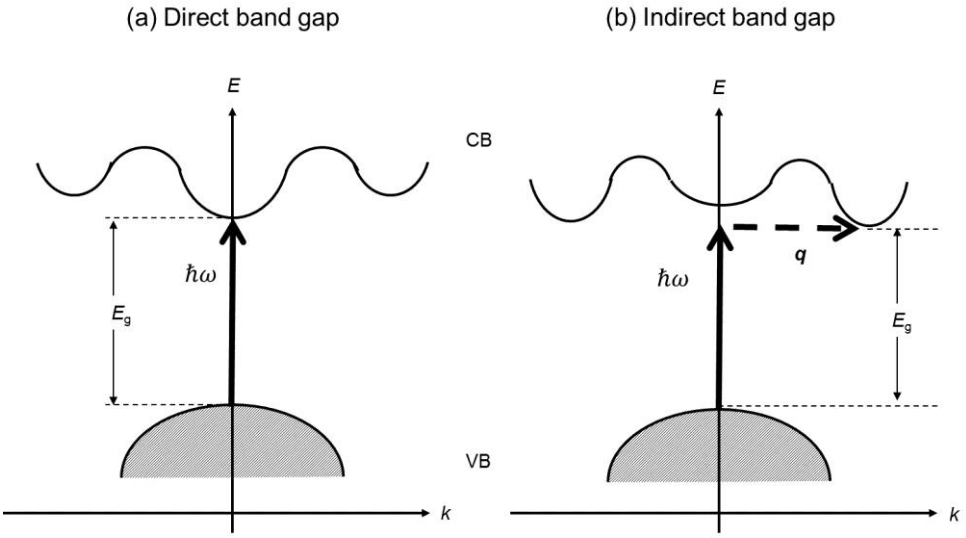

Fig. 1.23: Interband transitions in (a) indirect band gap and (b) indirect band gap semiconductors

In indirect gap semiconductor, energy and momentum must be conserved in the optical transition from VB to CB. The transition from VB in state (E_i, $\boldsymbol{k}_i$) to CB in state (E_f, $\boldsymbol{k}_f$) is given by following equations:

$$E_f = E_i + \hbar\omega \pm \hbar\Omega$$

$$\hbar\boldsymbol{k}_f = \hbar\boldsymbol{k}_i + \hbar\boldsymbol{q}$$

, where $\hbar\omega$, $\hbar\Omega$, $\boldsymbol{q}$ are photon energy, phonon energy and wave vector, respectively. Photons have very small wave vector so it is negligible. The absorption coefficient of indirect gap semiconductors is relatively weak in comparison with that of direct semiconductors, since the indirect transition needs both photon and phonon for the optical intrerband transitions. Conversely, electrons and holes are harder to recombine in indirect gap semiconductor than direct semiconductor. Thus, the radiative life time for indirect gap semiconductors is much longer than that for direct semiconductors [31].

Furthermore, Ge/Si hetero-structure exhibits type-II band lineup [32-34]. Figure 1.24 shows (a) type-I and (b) type-II band profile in hetero-structures. Electrons and holes are confined in same spatial region in type-I, while type-II is able to separate electron and holes in real space. The VB offset

leads to localization of holes in Ge region and the CB offset works as potential barrier for electron. Therefore, the type-II hetero-interface is expected to suppress the recombination of carriers, which leads to higher collection efficiency in solar cells. The effective valence band offset is thought to be about 400 meV for Ge/Si heterostructure [15].

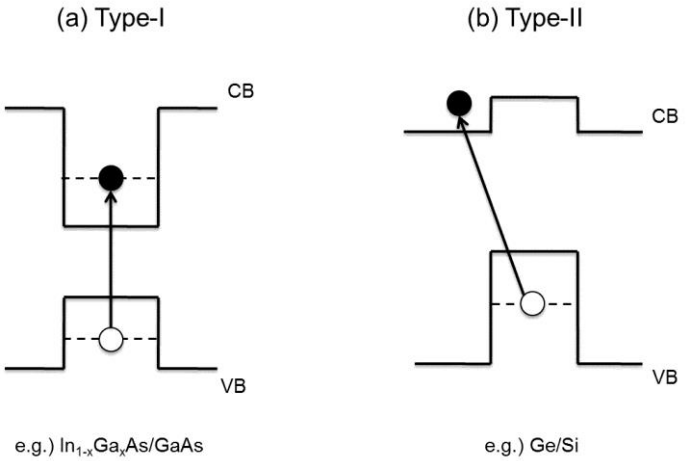

Fig. 1.24: Concise band lineups of (a) type-I and (b) type-II hetero-structure.

1.5. Purpose of this study

The QD-IBSCs are expected to achieve significant improvement of conversion efficiency so study on quantum dots and its application to solar cells is much attractive for higher conversion efficiency than conventional single junction solar cells. So far, In(Ga)As/GaAs QDs is widely studied for QD-IBSCs and interesting evidences such as two-step optical transition are reported, however significant increase in conversion efficiency is still not observed. The one of the reasons is thought to be high luminescence efficiency accrued from the energy band profile enhancing recombination. Both In(Ga)As and GaAs are direct bandgap semiconductors, which leads to short radiative life time. Furthermore, In(Ga)As/GaAs heterointerface shows the type-I band lineup resulting in confinement of electrons and holes in same space and thus enhancement of carriers recombination. Therefore, carriers in energy levels of QDs, electrons in case of In(Ga)As/GaAs QDs, are not able to stay enough long time to be pumped up in CB by second photons. On the other hand, Ge/Si QDs are expected to suppress the recombination thanks to indirect bandgap semiconductors and type-II band lineup. It is thought that the Ge/Si QDs could contribute to high carrier collection efficiency. Furthermore, In and Ga are precious metals while Si is relatively abundant so Ge QDs in Si matrix is relatively favorable in perspective of material consumption and cost.

Dense QDs are preferred for application to QD-IBSCs [35] to absorb sufficient photons. Although, the solar cells using Ge QDs in Si matrix have been reported by a few groups [36-41], previous studies on Ge/Si QDSCs have mainly concentrated on characterization of Ge/Si QD solar cells. There are few studies focusing on fabrication of dense and uniform Ge QDs for application to solar cells. So, we concentrated on fabricating multi-stacked Ge QDs with high density and high uniformity as well as short inter-dot spacing in direction to p-n junctions for studying concept of QD-IBSCs. Dense and uniform Ge/Si QDs are grown by using low growth temperature and surfactants such as antimony (Sb), however low growth temperature generally degrade crystal quality and Sb works as donor in IV group materials. The Sb doping in Si would cause difficulty to control doping profile in solar cells, since the

solar cells are devices using p-n junction. To overcome this issue, we employed high deposition rate of Ge. The details of fabrication of single layer Ge QDs on Si substrates and multi-stacked Ge/Si QDs are given in chapter 3 and chapter 4, respectively.

Furthermore, short inter-dot spacing in direction to p-n junction is achieved by thin spacer layer thickness in multi-stacked QD structures. The thinner spacer layer thickness results in accumulation of compressive stress induced by Ge QDs due to larger lattice constant of Ge than Si and eventually generation of dislocations. To achieve thinner spacer layer thickness, we focused on strain compensation technique. The compressive stress established by QDs is compensated by tensile stress in the spacer layers. Alternating tensile and compressive regions prevent the multi-stacked QDs from generation of dislocation. In case of Ge QDs on Si substrates, spacer layer material is carbon incorporated Si since $Si_{1-x}C_x$ possess smaller lattice constant than Si. The details of fabrication of $Ge/Si_{1-x}C_x$ are described in chapter 5.

The purpose of this study is fabricating better crystal quality of multi-stacked Ge QDs with high density and uniformity as well as short inter-dot spacing for application to QD solar cells. Furthermore, the Ge QD structures are applied to solar cells to study the effect of Ge QDs on solar cells properties. In this thesis, we invesitaged following topics: (I) the growth of dense and uniform Ge QDs on Si(001) substrates, (II) the fabrication of multi-stacked Ge/Si QDs, (III) the preparation of multi-stacked $Ge/Si_{1-x}C_x$ QDs, and (IV) the fabrication of Ge QD solar cells.

References

[1] RCPV in AIST website (unit.aist.go.jp/rcpv/ci/about_pv/feature/index.html) [in Japanese].

[2] S. M. Sze and Kwok K. NG: *Physics of Semiconductor Devices* (Wiley,) 3rd edition, Appendix F.

[3] the solar spectral irradiance (AM1.5) provided byNational Renewable Energy Laboratory in USA (http://rredc.nrel.gov/solar/spectra/am1.5/).

[4] J. Nelson: "*The Physics of Solar Cells*" (Imperial College Press, 2013), Chapter 1.

[5] L. Korte, E. Conrad, H. Angermann, R. Stangl, M. Schmidt: Sol. Energy Mater. Sol. Cells **93** (2009) 905–910.

[6] H. Fujiwara and M. kondo: Appl. Phys. Lett. **90**, 013503 (2007).

[7] M. Tanaka, M. Taguchi, T. Matsuyama, T. Sawada, S. Tsuda, S. Nakano, H. Hanafusa, and Y. Kuwano: Jpn. J. Appl. Phys. **31** (1992) 3518-3522.

[8] W. Shockley and H. J. Queisser : J. Appl. Phys. **32** (1961) 510.

[9] Loise C. Hirst *et al* : Prog. Photovolt: Res. Appl. 2011; **19**:286.

[10] A. López, A. Martí and A. Luque : *Next generation of Photovoltaics New concept* (Springer, 2012) Chapter 1.

[11] W. Guter, J. Schöne, S. P. Philipps, M. Steiner, G. Siefer, A. Wekkeli, E. Welser, E. olive, A. W. Bett, and F. Dimtoth: Appl Phys. Lett. 94, 223504 (2009).

[12] A. Luque and A. Marti : Phys. Rev. Lett. **78** (1997) 5014.

[13] A. Luque and A. Marti : Adv. Mater. **22** (2010) 160-174.

[14] M. Fox: "Optical Properties of Solids" (Oxford, 2010) 2nd edition, Chapter 6.

[15] K. Brunner: Rep. Prog. Phys. **65** (2002) 27-72.

[16] T. Sugaya, T. Amano, M. Mori, S. Niki: Appl. Phys. Lett. **97** (2010) 043112.

[17] G. S. Solomon, J. A. Trezza, A. F. Marshall, and J. S. Harris Jr: Phys. Rev. Lett. **76** (1996) 952-955..

[18] M. K. Zundel, P. Specht, K. Eberl, N. Y. Jin-Phillipp, and F. Fhillipp: Appl. Phys. Lett. **71** (1997) 2972-2974.

[19] W. Hu, M. M. Rahman, M-Y. Lee, Y. Li,a nd S. Samukawa: J. Appl. Phys. **114**, 124509 (2013).

[20] A.I. Yakimov, A. A. Blochkin and A. V. Dvurechenskii: Semicond. Sci. Technol. **24** (2009) 095002.

[21] M. K. Zundel, P. Specht, K. Eberl, N. Y. Jin-Phillipp, and F. Fhillipp: Appl. Phys. Lett. **93** 132105 (1997).

[22] A. López, A. Martí and A. Luque : "*Next generation of Photovoltaics New concept*" (Springer, 2012) chapter 8.

[23] S. A. Blockhin, A. V. Sakharov, A. M. Nadtochy, A. S. Pauysov, M. V. Maximov, N. N. Ledentsov, A. R. Kovsh, A. R. Kovsh, S. S. Mikhrin, V. M. Lantratov, S. A. Mintairov, N. A. Kaluzhiny, and M. Z. Shvatts: Semiconductors. **43** (2009) 514-518.

[24] Y. Shoji, K. Akimoto, and Y. Okada: J. Phys. D: Appl. Phys. **46** (2013) 024002.
[25] Y. Okada, T. Morioka, K. Yoshida, R. Oshima, Y. Shoji, T. Inoue, and T. Kita: J. Appl. Phys. **109** (2011) 024301.
[26] R. Oshima, A. Takata, and Y. Okada: Appl. Phys. Lett. **93** (2008) 083111.
[27] T. Sugaya, O. Numakami, R. Oshima, S. Furue, H. Komaki, T. Amano, K. Matsubara, Y. Okano, S. Niki: Energy Environ. Sci. **5** (2012) 6233.
[28] T. Sugaya, O. Numakami, S. Furue, H. Komaki, T. Amano, K. Matsubara, Y. Okano, S. Niki: Sol. Energy Mater. Sol. Cells. **95** (2011) 2920-2923.
[29] N. Kasamatsu, T. Kada, A. Hasegawa, Y. Harada, and T. Kita: J. Appl. Phys. 115 (2014) 083510.
[30] M. Fox: "Optical Properties of Solids" (Oxford, 2010) 2nd edition, Chapter 3.
[31] M. Fox: "Optical Properties of Solids" (Oxford, 2010) 2nd edition, Chapter 5.
[32] T. Tayagaki, K. Ueda, S. Fukatsu, and Y. kanemitsu: J. Phys. Soc. Jpn. **81** (2012) 064712.
[33] A. I. Yakimov, N. P. Stepina, A. V. Dvurechenskii, A. I. Nikiforov, and A. V. Nenashev: Semicond. Sci. Technol. 15 (2000) 1125-1130.
[34] S. Fukatsu, H. Sunamura, Y. Shiraki, and S. Komiyama: Appl. Phys. Lett. **71** (1997) 258-260.
[35] K.Sakamoto, Y. Kondo, K. Uchida, and K. Yamaguchi, J. Appl. Phys. **112** (2012) 124515
[36] Z. Liu, T. Zhou, L. Li, Y. Zuo, C. He, C. Li, C. Xue, B. Cheng, and Q. Wang: Appl. Phys. Lett. **103** (2013) 082101.
[37] T. Tayagaki, K. Ueda, S. Fukatsu, and Y. Kanemitsu: J. Phys. Soc. Jpn. **81** (2012) 064712.
[38] T. Tayagaki, N. Usami, W. Pan, Y. Hoshi, K. Ooi, and Y. Kanemitsu: Appl. Phys. Lett. **101** (2012) 133905.
[39] M. L. Lee, G. Dezsi, and R. Venkatasubramanian: Thin Solid Films **518** (2010) S76-S79.
[40] A. Alguno, N. Usami, K. Ohdaira, W. Pan, M. Tayanagi, and K. Nakajima: Thin Solid Films **508** (2006) 402-405.
[41] N. Usami, A. Alguno, K. Sawano, T. Ujihara, K. Fujiwara, G. Sazaki, Y. Shiraki, and K. Nakajima: Thin Solid Films **451-452** (2004) 604-607.

Chapter 2. Experimental

This chapter gives brief explanation about equipment for growth and characterization of Ge QDs. Furthermore, growth procedures of Ge QDs are described as well as fabrication procedures of solar cells.

2.1. Equipment for sample preparation

2.1.1. Solid-source molecular beam epitaxy

All self-assembled Ge quantum dots were grown on Si(001) by solid-source molecular beam epitaxy (SS-MBE) equipment. In general, the MBE is epitaxial crystal growth in ultra-high vacuum around 10^{-10} Torr by using one or few atomic or molecular species [1]. The MBE is advantageous to achieve high crystal quality because the MBE are able to control contents of mixed crystal and layer thickness minutely. For these striking features, it is widely used for growth of thin monocrystalline layer on substrate as well as multi-stacked QDs structure [2,3]. Figure 2.1 shows a schematic image of our SS-MBE. The MBE equipment is composed of growth chamber and loading chamber. A turbo-molecular pomp connecting a oil rotary pomp and a ion pomp are used for decompression in growth chamber. The base pressure of growth chamber is on the order of 10^{-10} Torr. Silicon and germanium ingots were heated by each electron beam gun. A Kunudsen cell (K-cell) and carbon filament cell was used for heating gallium and carbon, respectively. A cryoshroud for liquid nitrogen is equipped with the SS-MBE growth chamber to prevent layers from incorporation of contamination. Reflection high energy electron diffraction (RHEED) is installed to monitor surface conditions of samples in-situ.

The RHEED is capable of monitoring sample surfaces during growth [4]. The RHEED generally consists of a electron beam source and a screen. Electrons emitted by the filament are accelerated up to

about few tens of keV by applied voltage. The electrons irradiate on samples and are reflected to a monitor. Diffracted electrons by sample show the some patterns in monitor which provides surface condition of samples. Figure 2.2 shows RHEED images for Si(001) substrate (a) before thermal cleaning, (b) after thermal cleaning at 750 °C and (c) single Ge self-assembled QDs on Si(001) substrate as examples. The weak 1×1 RHEED patterns were observed before thermal cleaning, which indicates ultra-thin oxide layer was formed on Si(001) substrate. The 2×1 reconstructed Si(001) surface was observed in (b), which means clean and atomically flat surface is obtained. Arrow head patterns, so called 'Chevron pattern', was observed in (c). The Chevron pattern indicates island growth. In this way, surface condition is monitored by RHEED.

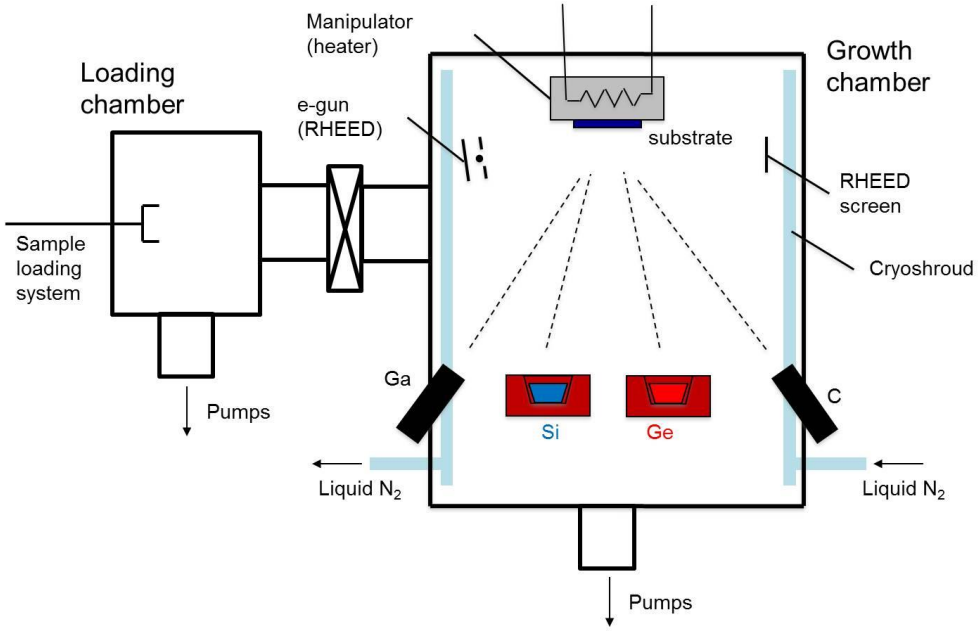

Figure 2.1: Schematic illustration of our SS-MBE.

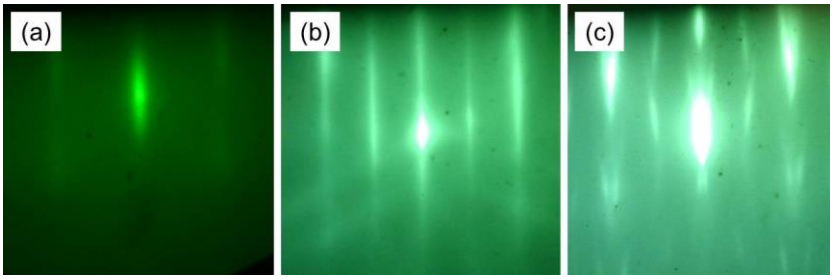

Figure 2.2: RHEED images for Si(001) surface (a) before and (b) after thermal cleaning and (c) island growth.

2.1.2. Plasma enhanced chemical vapor deposition

To form p-n junction for fabrication of solar cells, hydrogenated amorphous Si (a-Si:H) were deposited on Si covered multi-stacked Ge QDs by plasma enhanced chemical vapor deposition (PECVD). CVD is a technique to form thin films on substrates by utilizing chemical reaction of source gases [5]. PECVD employs plasma to cause the chemical reaction. In this work, vacuum chamber is pumped by dry pumps, mechanical booster pumps and turbo molecular pumps. The base pressure was on the order of 10^{-1} Pa. Samples were heated during deposition. For source gases, hydrogen diluted SiH_4 and PH_3 were used and they were decomposed by plasma induced by radio frequency (RF). Only SiH_4 was provided into reaction chamber to deposit intrinsic type a-Si:H. Both SiH_4 and PH_3 were simultaneously supplied for deposition of n-type a-Si:H.

2.1.3. Sputtering

We employed a sputtering equipment to deposit indium tin oxide (ITO) for fabrication of contact for solar cells. The sputtering is the phenomenon which is emission of particles on surface of solids by collision of ionized inert gases [5]. Sputter deposition is performed by attachment of the emitted particles, so called sputtering particle, on substrates. In our experiments, a ITO ingot was sputtered by ionized Ar and O_2 by RF of 100 W at pressure of about 1×10^{-6} Torr and 75 nm-thick ITO were

deposited on p-n junction formed samples. The vacuum was created by a cryopump and a dry pomp. The flow rate of Ar and O_2 were 200 ccm and 1.5 ccm, respectively.

2.2. Equipment for sample characterization

2.2.1. Atomic force microscope

A atomic force microscope (AFM) equipment were employed to investigate surface morphology. The AFM scans a cantilever on sample surface and obtain surface morphology by detecting the displacement of cantilever induced by atomic force between the tip of cantilever and surface [6]. A schematic illustration is depicted in Fig. 2.3. Our AFM is mainly composed of cantilever, laser, displacement sensor, vibration removal board, and microscope to adjust optical axis for the cantilever and sensor. In general, the tip and sample surface are constantly touched each other during measurements. In our AFM measurements, we used the tapping mode which the tip contacts with sample surface periodically and it prevent sample surface from some damage arisen form contact with tip.

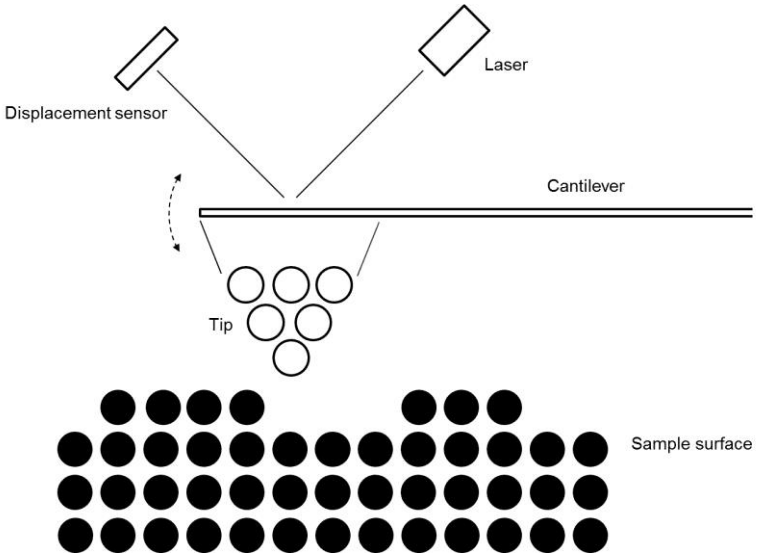

Figure 2.3: Principal illustration of AFM.

2.2.2. Scanning transmission electron microscope

Scanning transmission electron microscope (STEM) was used to study cross-section of multi-stacked Ge QDs. The STEM is combination of the TEM and the scanning electron microscope

(SEM) [7]. The TEM are able to obtain information in minute region of samples by irradiating accelerated electrons to samples and imaging transmitted electrons. The SEM gives surface morphology of sample by scanning electron beams on samples surface.

When high energy electrons are irradiated to thin samples, almost all electrons transmit the samples, so called transmitted electrons, and part of electrons are scattered, so called scattered electrons. The some scattered electrons keep energy, and others lose energy in collisions with atoms of samples. In general, the TEM creates images to utilize transmitted electrons and elastically scattered electrons.

If a sample is crystalline, some electron beams are scattered to definite directions due to Bragg diffraction, which separate transmitted electron beams into transmitted waves and diffracted waves. TEM images are obtained by those electron beams selected by objective aperture. When only the transmitted waves are allowed to pass objective aperture, the bright field (BF) TEM image is obtained. On the other hand, dark field (DF) TEM image are acquired by imaging the diffracted waves. The BF images become brighter in images out part of a sample due to attenuation of transmitted waves, whereas the DF images become darker due to absence of diffracted waves. In particular, TEM images using diffracted waves to high angle are called high angle annular dark field (HAADF) images. The HAADF images are advantages to recognize an element.

2.2.3. High resolution X-ray diffraction

The X-ray diffraction is widely used to study structural information of epitaxial layers [8-10]. We investigated content of carbon in epitaxially grown $Si_{1-x}C_x$ layer on Si substrates by ω-2θ measurements in high resolution X-ray diffraction (HR-XRD). The feature of HR-XRD is monochromatic and parallel X-ray beam. The ω-2θ measurement gives information about change of plane distance. If epitaxial layers have smaller lattice constant than substrates in growth direction, the epitaxial layer is deformed by tensile stress and thus X-ray peak of the epitaxial layers appeared in high angle region. On the other hand, the epitaxial layer is deformed by compressive stress if the

lattice constant of epitaxial layer is larger than that of substrates in growth direction, which leads to appearance of x-ray peaks in lower angle region. The schematic of ω-2θ measurement is illustrated in Fig. 2.4. From the displacement of X-ray peak (004) for $Si_{1-x}C_x$ layer from Si substrate peak, we estimated the content for epitaxially grown $Si_{1-x}C_x$ layers

Furthermore, reciprocal space mapping (RSM) around (224) was used to study stain condition of multi-stacked Ge QDs. The RSM is two dimensional scans in reciprocal space. The RSM utilizing asymmetric X-ray reflection around (224) gives information about in-plane as well as out-plane. If the X-ray peaks from epitaxial layers were away from that form substrates in in-plane direction, it means that epitaxial layers partially or fully relax. The X-ray peaks from epitaxial layers were same value of that from substrates in in-plane direction, which indicates the epitaxial layer is fully strain. The detailed principal of both measurements are given in [11,12].

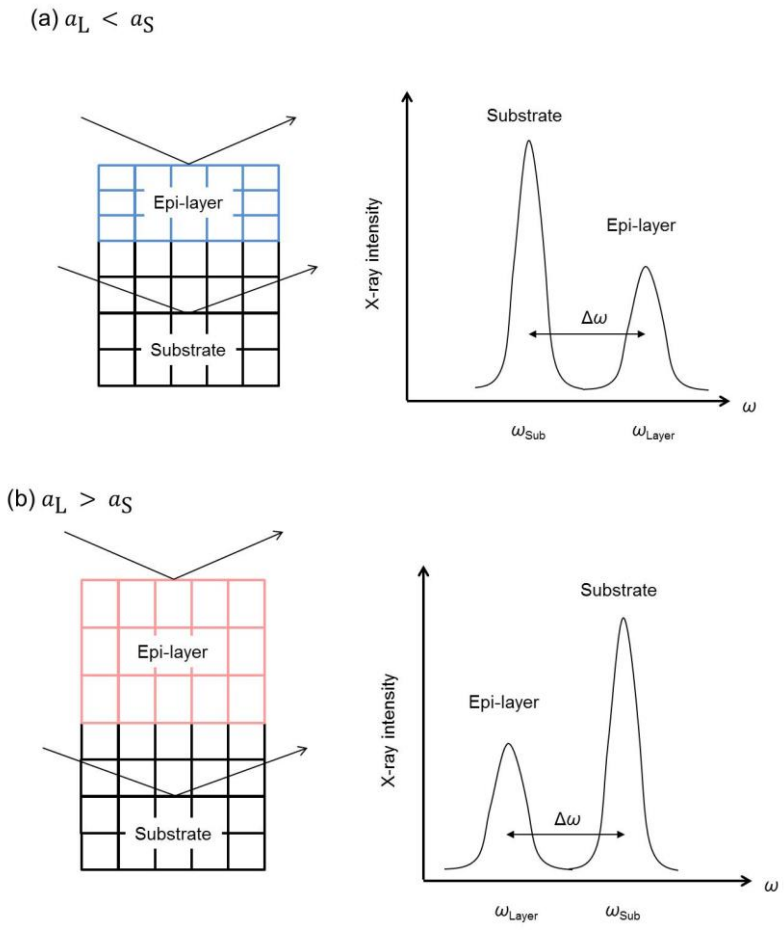

Figure 2.4: Schematic of ω-2θ measurement in case of (a) $a_L < a_S$ and (b) $a_L > a_S$.

2.2.4. Photoluminescence spectroscopy

Photoluminescence (PL) spectroscopy were employed to investigate optical properties of multi-stacked Ge QDs in this thesis. The PL is re-emisssion of light after elecrons and holes in a semiconductor are excited by illumination of light with higher energy than bandgap as shown in Figure 2.5. The details about PL is given in [13]. PL measuremets are gnerally used for characterization of energy levels in near band edge and impurity levels with in the band gap [14,15]. Thus, The PL measurement is a powerful method to investigate crystal quality of self-assembled QDs since quantized levels of the QDs is located with in band gap of matrix.

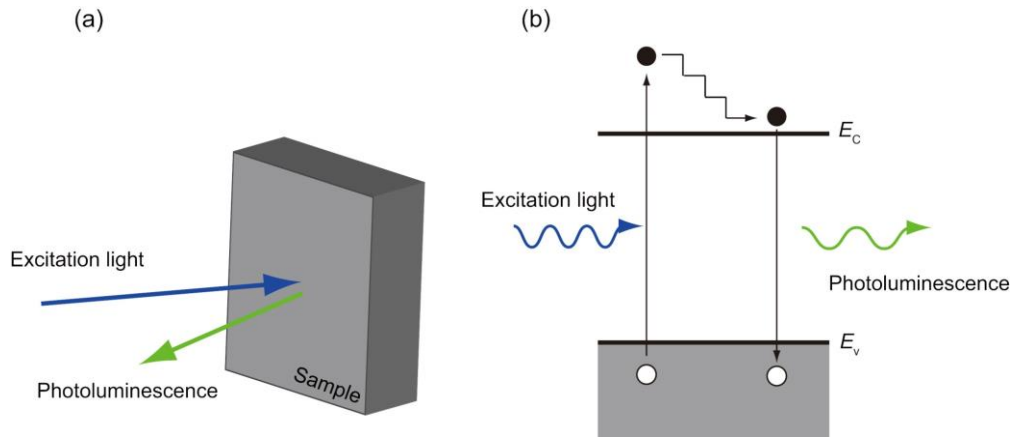

Figure 2.5: (a) PL configuration and (b) general scheme of PL in materials.

Simplified experimental setup of our PL spectroscopy is depicted in Fig. 2.6. A 532 nm Nd:YAG laser was used as excitation light source. It posseses enogh energy to excite electrons in Ge QDs in Si matrix. Liquid nitrogen cooled Ge photodetector was used thus photolumnescense with energy higher than fundamental bandgap energy about 0.67 eV are detectable. Standard lock-in configuration was utilized to improve ratio of signal to noise. A IR-80 filter was inserted in front of a spectrometer to prevent 532 nm light from entering a spectrometer. Excitation power of light source was chaned by using ND filters and measeared by a power meter. Samples are able to be cooled at 12 K by a cryostat during measurements.

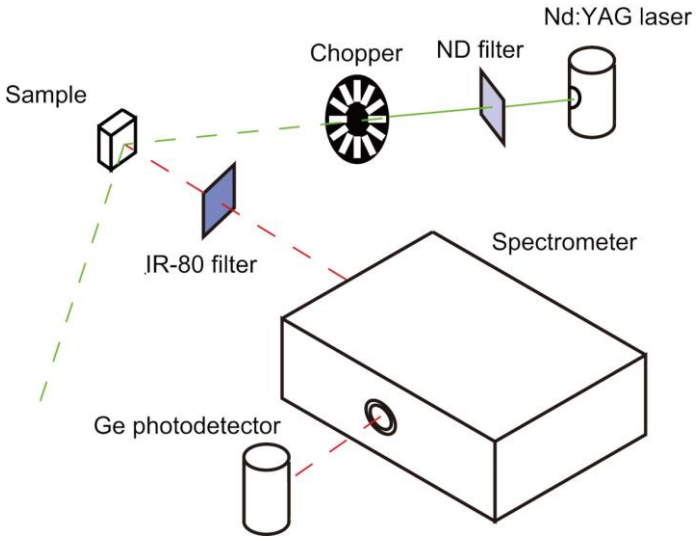

Figure 2.6: Simplified experimental setup of our PL measurements.

2.3. Sample preparation

2.3.1. Substrates cleaning

Before growth of self-assembled Ge QDs on Si(001) substrates, Si(001) substrate were cleaned by using chemical solution based on RCA cleaning method [16]. Figure 2.7 shows our cleaning procedures for Si(001) substrates. The RCA cleaning method generally utilizes two chemical solutions: (i) SC1 and (ii) SC2. The SC1 consists of ammonium hydroxide (NH_4OH) and hydrogen peroxide (H_2O_2) and it loosely etch Si surface, which is able to lift fine particles off. Furthermore, surface potential, so called zeta potential, of fine particles such as SiO_2 and Si_3N_4 shows same polarity with Si surface in SC1, which leads to prevention of re-attachment of the fine particles on Si surface thanks to electrostatic repulsion. The SC2 is composed of hydrochloric acid (HCl) and hydrogen peroxide (H_2O_2) and melts metal particles, which results in removal of metal contaminations. In addition to SC1 and SC2, we used aceton and SPM consisting of sulfuric acid (H_2SO_4) and hydrogen peroxide (H_2O_2) before RCA cleaning. In general, oil is easy to dissolve in aceton so it is used to remove oil contamination from Si surface. The SPM decomposes organic contaminations to CO_2, H_2O and so on [17]. Therefore, organic contaminations are purged before RCA cleaning.

① Blow by N_2	
② Ultrasonic waves cleaning in Aceton	[RT for 5 min]
③ Rinse in pure water	
④ H_2SO_4/H_2O_2 (SPM)	[4:1, 120 °C for 10 min]
⑤ Rinse in pure water	
⑥ $NH_2OH_4/H_2O_2/H_2O$ (SC1)	[1:1:5, 70-80 °C for 10 min]
⑦ Rinse in pure water	
⑧ $NH_2OH_4/H_2O_2/H_2O$ (SC1)	[1:1:5, 70-80 °C for 10 min]
⑨ Rinse in pure water	
⑩ Blow by N_2	

Figure 2.7: Our cleaning procedure for Si substrates.

After cleaning in chemical solutions, Si(001) substrates were immediately loaded into the vacuum chamber. Then, initial thermal cleaning at 300 °C for 10 min was performed to remove water from Si substrates in loading chamber of the base pressure on the order of 10^{-8} Torr. Following transfer of Si substrates into growth chamber, second thermal cleaning at 750 °C for 10 min was carried out to remove ultrathin oxide layers on Si surface. We confirmed removal of the oxide layer by appearance of 2×1 reconstructed Si(001) surface in a RHEED monitor.

2.3.2. Growth procedure of Ge QDs

Following thermal cleaning, self-assembled Ge/Si QDs and Ge/$Si_{1-x}C_x$ QDs were grown by molecular beam epitaxy. We grew single Ge/Si QDs and Ge/$Si_{1-x}C_x$ QDs. To grow Ge QDs on Si, after growth of Si buffer layers on Si(001) substrates at 700 °C, additional Si layers were grown and then Ge were deposited. For growth of Ge QDs on $Si_{1-x}C_x$ layers, Si buffer layers and additional Si layers were similarly grown. Following growth of $Si_{1-x}C_x$ layers at 500 °C, Ge was deposited. The each growth procedure and its schematic image of samples are summarized in Fig. 2.8.

For multi-stacked Ge QDs, Ge and Si or $Si_{1-x}C_x$ were alternately deposited after Si buffer layer. We fabricated three types of multi-stacked Ge QDs: (i) multi-stacked Ge/Si QDs, (ii) multi-stacked Ge/$Si_{1-x}C_x$ QDs, and (iii) Ge/$Si_{1-x}C_x$ QDs with 2-nm-thick Si interlayers. Those schematic images are shown in Fig. 2.9. The 2 nm-thick Si interlayers were used to improve structural and optical properties. The details are described in Chapter 5.

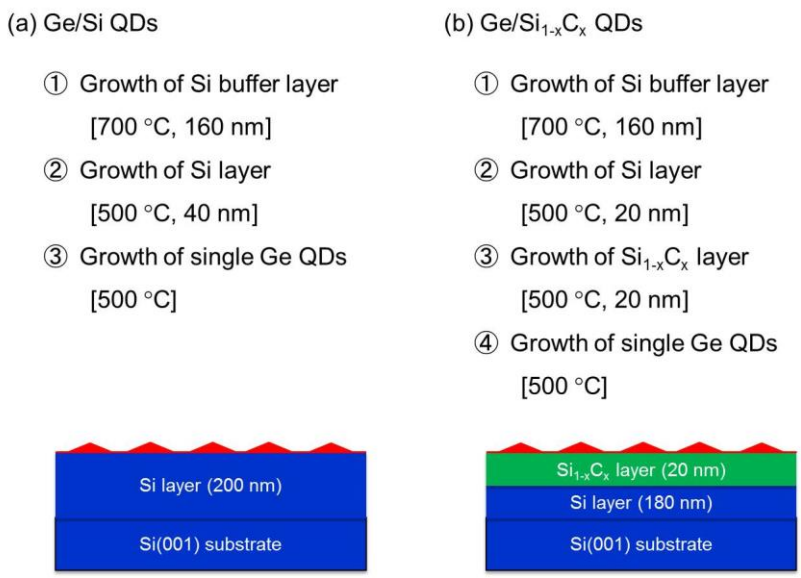

Figure 2.8: Growth procedure for single layer Ge QDs on (a) Si and (b) on $Si_{1-x}C_x$ layers

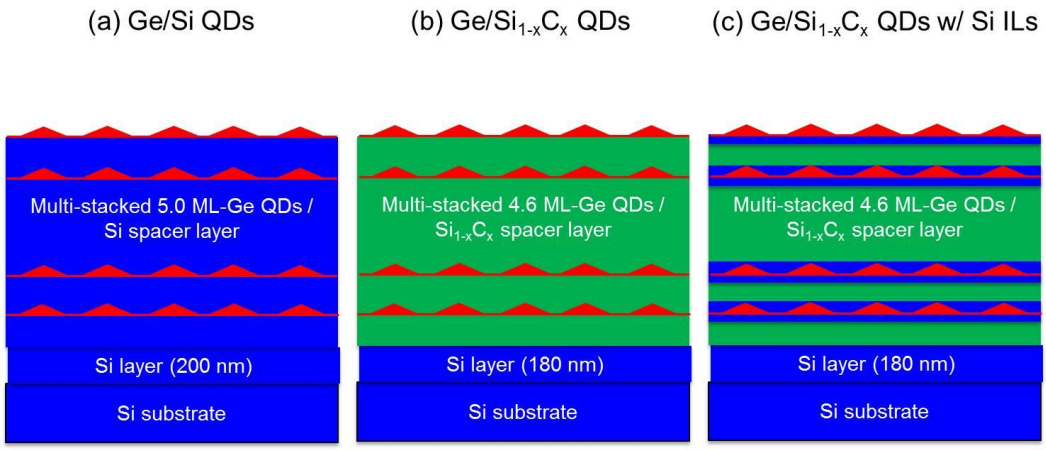

Figure 2.9: Schematic structure of grown multi-stacked (a) Ge/Si, (b) $Ge/Si_{1-x}C_x$, (c) $Ge/Si_{1-x}C_x$ QDs with Si ILs.

References

[1] S. Gonda: “Bunshisenepitakisi (Molecular Beam Epitaxy)” (Baifukan, 1994) Capter 1 & Chapter 2 [in Japanese]

[2] K. Akahane, N. Yamamoto, and T. Kawanishi: Phys. Status. Solidi **A 208** (2011) 425-428.

[3] Y. Shiraki, H. Sunamura, N. Usami, S. Fukatsu: Appl. Surf. Sci. **102** (1996) 263-271.

[4] The Surface Science Society of Japan: “*Hyoumendensikaisetsuhou* (*Electron Diffraction at Surface*)” (Maruzen, 2002) Chapter 2 & Chapter6 [in Japanese].

[5] H. Tango: “Handoutapurosesugijutsu (Process Technique for Semiconductors)” (Baifukan, 2006) [in Japanese].

[6] The Surface Science Society of Japan: “*Sousapuroubkenbikyou* (*Sccaning Proeb Microscope*)” (Maruzen, 2002) Chapter 3 [in Japanese].

[7] The Surface Science Society of Japan: “*Toukagatadensikenbikyou* (*Transmission Electron Microscope*)” (Maruzen, 2002) Chapter 1 [in Japanese].

[8] R. Oshima, T. hashimoto, H. Shigekawa, and, Y. Okada: J. Appl. Phys. **100**, 083110 (2006).

[9] J. E. Chunningham, K. W. Goossen, M. Williams, and W. Y. Jan: Appl. Phys. Lett. **60** (1992) 727-729.

[10] T. katsuyama, S. M. Bedair, N. C. Giles, R. P. Burns, and J. F. Schetzina: J. Appl. Phys. **62** (1987) 498-502.

[11] E. Kasper, N. Escoubs, J. Werner, Oehme, and K. Lyutovich: J. Appl. Phys. **111**, 63507 (2012)

[12] G. Bauer, J. Li, E. Koppensteiner: J. Cryst. Growth **157** (1995) 61-67.

[13] M. Fox: “*Optical properties for Solids*” (Oxford) 2nd edition, Chapter 5.

[14] J. Weber and M. I. Alonso: Phys. Rev. B **40** (1989) 5683-5693.

[15] P. J. Dean, J. R. Haynes, and W. F. Flood: Phys. Rev. **161** (1967) 711-729.

[16] W. Kern: J. Electrochem. Soc. **137**, (1990) 1887-1892.

[17] T. Ohmi: J. Electrochem, Soc, **143** (1996) 2957-2964.

Chapter 3. Single Layer Ge QDs on Si

In this chapter, fabrication of single layer Ge QDs on Si substrates are described to obtain dense and uniform Ge QDs. Dense and uniform Ge/Si QDs are needed for QDSC application to absorb sufficient photons in Ge QDs and formation of minibands. Though such QDs are obtained by using Sb surfactant [1,2] or lower growth temperature less than 400 °C [3,4], Sb surfactant leads to unintentional doping to Ge/Si QDs, which arises difficulty to control doping profile for application to solar cells. Lower growth temperature results in low crystal quality. Therefore, new growth technique should be crucial for dense and uniform Ge/Si QDs. For this reasons, growth condition were systematically investigated to obtain Ge QDs with high density and highly uniform Ge QDs.

3.1. Introduction

Self-assembled QDs are widely used for application to QD solar cells and they are formed as results of S-K growth mode in the hetero epitaxial growth. Theory of crystal growth and self-assembled QDs is elaborated on in [5]. Epitaxial growth is growth of layer with high perfection and composition on crystalline substrate. The epitaxial growth is classified into homo-epitaxial growth and hetero-epitaxial growth. In homo-epitaxial growth, layer material is identical with substrate material. On the other hand, layer material is different with substrate materials in hetero-epitaxial growth.

Strain is induced by hetero-epitaxial growth of thin epitaxial layer on much thicker substrate, since the lattice constant of layer material (a_L) is different with that of substrate materials (a_S). Figure 3.1 shows a schematic image of hetero-interface between epitaxial layer and substrates. When the a_L is larger than the a_S, lateral constant of a_S is same even in epitaxially grown layer and vertical lattice constant is changed to $a_{L\perp}$ due to deformation resulting in strain.

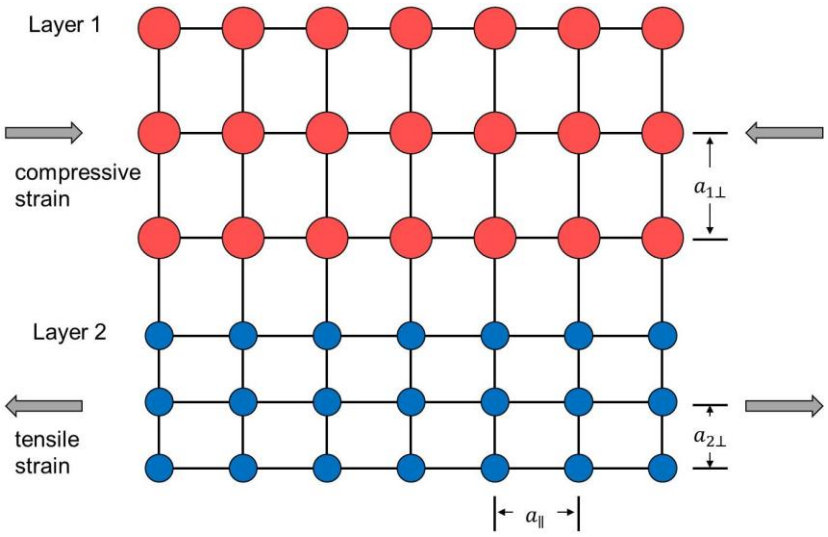

Fig. 3.1: Schematic image of interface between layer 1 and 2 in hetero-epitaxial growth. The $a_{\parallel}$, $a_{1\perp}$, and $a_{2\perp}$ are common lateral lattice constant, vertical lattice constant of strained layer 1 and 2, respectively.

The fundamental growth mode in hetero-epitaxial growth is classified with three modes: (i) Frank-Van der Merve (F-M) mode, (ii) Volmer-Weber (V-M) mode, and (iii) Stranski-Krastanov (S-K) mode. The schematic images of three growth modes are depicted in Fig. 3.2. The F-M mode corresponds to the layer-by-layer growth mode which atomically flat and smooth epitaxial layer is grown on substrates. The V-M growth mode is the island growth which three-dimensional islands are grown on substrate. The S-K growth mode is intermediate case between the F-M growth mode and V-M mode. It initially grows two-dimensional layer and subsequently transforms to three-dimensional islands growth. The growth mode is determined by the total energy composed of substrate surface energy, epilayer surface energy, interface energy and strain energy. Here, only S-K growth mode is explained, since we employed the self-assembled Ge/Si QDs using the S-K mode. As mentioned above, strain is induced in epilayer in hetero epitaxy. For system with small interface energy but large strain mismatch, initial growth is layer-by-layer growth accompanying stain energy and large strain energy in thicker epilayer can be reduced by forming islands, which means layer-by-layer growth is

energetically favored in thin layer thickness and islands growth become energetically favored after exceeding some critical layer thickness [6].

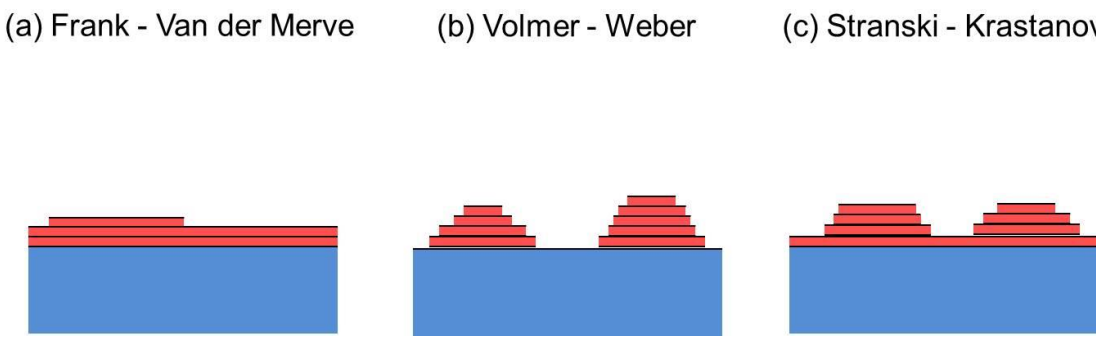

Fig. 3.2: Schematic image of three growth modes: (a) Frank-Van der Merve mode, (b) Volmer-Weber mode, and (c) Stranski-Krastanov mode.

Self-assembled QDs using S-K growth mode are a promising approach to fabricate dislocation-free semiconductor QDs in semiconductor matrix. Fine structure with high material quality fabricated by S-K growth mode is termed as self-assembled quantum dots (QDs). InAs self-assembled QDs in GaAs matrix show the ultra-narrow luminescence which is a feature of QDs by employing cathode luminescence (CL) with high resolution in space [7].

Self-organized QDs is array of self-assembled QDs in-plane and/or out-plane. Surface morphology and optical properties of self-assembled QDs are controllable to some extent by growth condition and substrate orientation. The self-organized QD array in-plane is achieved in InGaAs QDs on GaAs(311)B substrate [8,9], InGaAs QDs on InP(311)B substrate [10], Ge QDs on vicinal Si(001) surface [11], Ge QDs on pit-patterned Si(001) substrate [12,13]. Furthermore, vertically aligned QDs were obtained by propagation of strain caused by buried QDs by matrix [10,12,14,15]. Self-organized QDs is a powerful candidate to fabricate QDSLs.

Dense QDs are favored to absorb sufficient photons in QDs. In general, self-assembled Ge/Si QDs on Si(001) substrates shows areal density on the order of 10^9 cm^{-2} and bimodal size distribution due to coexistence of small pyramid-shaped and large dome-shaped QDs [16-19]. The self-assembled QDs

are grown by employing different substrate such as Si(111) [20], Si(113) [21] and pit-patterned Si(001) [22,23]. The Ge islands on Si(111) shows flat islands with height of about 10 nm lateral size of about 180 nm. And deposition of Ge on Si(113) forms wire-shaped islands. Furthermore, Ge QDs on pit-patterned Si(001) substrates by reactive ion etching (RIE) show well aligned in direction to in-plane and homogeneous in size, however the RIE process for each layer is not reasonable for fabrication multi-stacked QD structures. Therefore, the author focused on Si(001) substrates. High areal density is realized by using low growth temperature at about 400 °C [3,4] and anti-surfactants such as antimony (Sb) [1,2] due to suppression of surface migration of Ge adatoms.

In epitaxial growth, generally, atoms in vapor reduce their kinetic energy on surface of substrate and bond with surface atoms weakly. Then, adatoms randomly work by hopping potential energy E_m created by surface atoms. The behavior is termed as "migration". The hopping rate to neighbor adsorption position $1/\tau$ is given by following equation [24]

$$\frac{1}{\tau} = zv\exp\left(-\frac{E_m}{kT}\right) \tag{3.1}$$

, where k, T, z and v are Boltzmann constant, temperature of substrate, available hopping sites and frequency of bonding, respectively. The value of v is estimated at about 10^{13} s^{-1} from frequency of phonons. From Eq. (3.1), lower substrate temperature results in smaller hopping rate and hence suppression of the migration. It is thought that the Sb anti-surfactant similarly suppresses the surface migration. The suppressed migration leads to generation of many nuclei in smaller region and depressed evolution of QDs. Therefore, decreased QD size and increase in areal density are observed with decrease in temperature.

Although the suppression of migration helps to form dense QDs, lower growth temperature leads to degradation of crystal quality. The Sb is a donor in Si and Ge, which results in unexpected impurities doping. Other methods are necessary to grow dense Ge QDs for solar cell application. Recently, highly-stacked InGaAs/GaAs QDs are successfully grown by using high deposition rate of 1

monolayer (ML) per second and growth interruption [25]. Furthermore, Ge QDs with high density and uniformity were observed by using high deposition rate of 2 ML/s and growth temperature at 500 °C due to high surface concentration of Ge adatoms [26]. The higher surface concentration of adatoms reduces available hopping sites *z* in Eq. (3.1), which results in suppression of migration and thus high density could be obtained. So we concentrated on the high deposition rate to grow dense and uniform Ge QDs since it allows us to employ relatively high growth temperature without surfactant.

3.2. Self-assembled Ge nano dots on Si surface

At first, it was found that hetero epitaxial growth of Ge on Si shows the S-K growth mode. All samples were fabricated on Si(001) substrate by SS-MBE. Before loading into chamber, Si(001) substrates were cleaned by RCA cleaning procedures. Following thermal cleaning at 750 °C for removing ultra-thin oxide layer, Si layer were grown on Si substrate. Then, Ge was deposited at growth temperature of 560 °C and deposition rate of 0.2 Å/s as employed in [16]. Figure 3.3 shows 1 × 1 μm^2 AFM images and RHEED images for single Ge/Si QDs with layer thickness of (a) and (b) 0 monolayer (ML), i.e. Si(001) substrate, (c) and (d) 3.9 ML, and (e) and (f) 4.6 ML, respectively. The 2 × 1 pattern of reconstructed Si(001) surface was observed in Fig. 3.3 (b) and there were no Ge islands in Fig. 3.2 (a). Although (c) shows the flat surface, two different RHEED patterns were observed in (d), one comes from the Si substrate and the other from thin Ge layer, which indicates layer by layer epitaxial growth until 3.9 ML.

When layer thickness reaches 4.6 ML, three-dimensional islands were observed in Fig. 3.3 (e). The islands consisted of smaller in lateral size of ~40 nm and larger islands in size of ~60 nm. The angle of smaller pyramid-shaped and larger dome-shaped island was about 10° and 21° to surface, respectively, which is good agreement with previous works [27-29]. The different shapes results from minimization of total energy of islands [30,31]. Furthermore, arrowhead-shape RHEED patterns, called as ‘chevron patterns’, were observed in Fig. 3.3 (f). In general, the chevron patterns arise from diffraction of electrons passing through facets of three-dimensional islands, so the chevron patterns with smaller (indicator A in Fig.3.3 (f)) and larger angle (indicator B in Fig.3.3 (f)) correspond to pyramid and dome islands, respectively [31]. From these results, hetero epitaxial growth in Ge/Si system shows S-K growth and critical layer thickness of transition to islands growth is around 4 ML, which is good agreement with [16]. From this results, the layer thickness than 4 ML is necessary for growth of Ge QDs on Si(001) substrates.

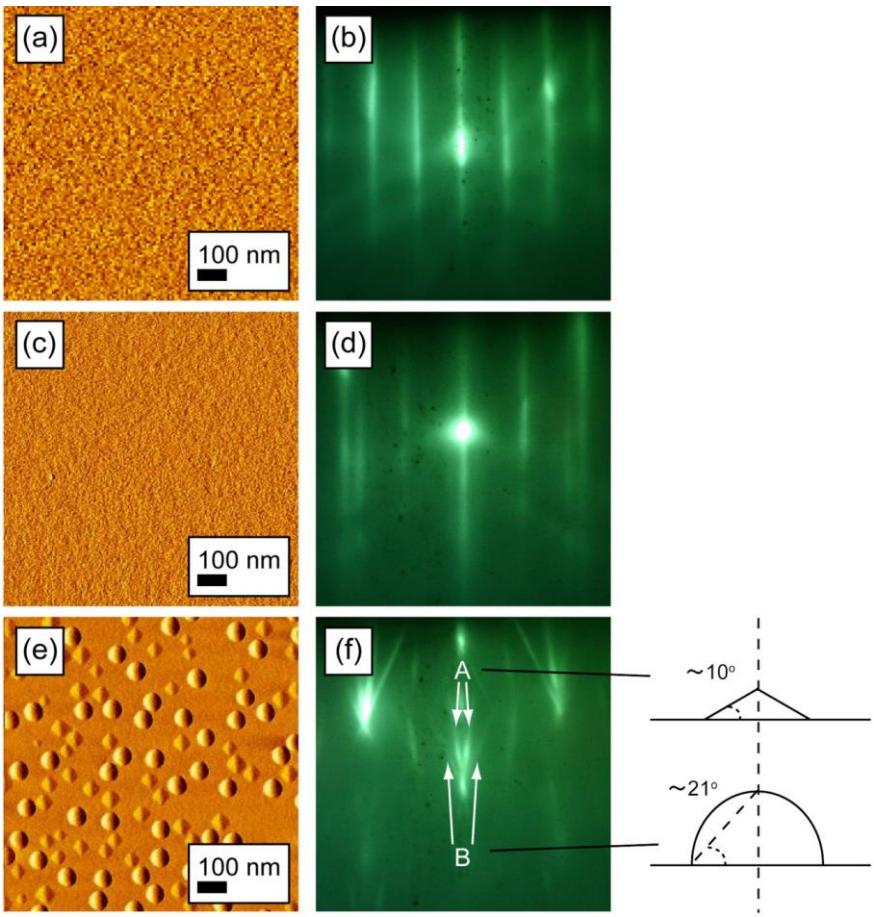

Fig. 3.3: 1 × 1 μm^2 AFM images and RHEED images of surface for single layer Ge QDs on Si(001) substrates. AFM images and RHEED patterns are shown for layer thickness of 0 ML in (a) and (b), of 3.9 ML in (c) and (d), and of 4.6 ML in (e) and (f), respectively. The A and B in (f) indicate chevron patterns due to smaller pyramid-shaped QDs and larger dome-shaped QDs, respectively. The inset shows schematic illustration of pyramid-shaped QDs and dome-shaped QDs with their angle to surface.

To investigate appropriate layer thickness of Ge QDs, the effect of layer thickness was investigated. Figure 3.4 shows AFM images of single Ge QDs on Si(001) substrate with layer thickness of (a) 3.9 ML, (b) 4.6 ML, (c) 5.3 ML (d) 6.0 ML, (e) 7.0 ML and (f) 7.8 ML. Both pyramid-shaped and dome-shaped Ge QDs were observed in (b)-(d). Furthermore, larger coalesced QDs at size of ~100 nm were generated in (e) and (f). Figure 3.5 shows dependence of lateral size and height on layer thickness for (a) dome-shaped QDs and (b) pyramid-shaped QDs. Both lateral size and height

increased with increasing layer thickness in (a), whereas those are independent on layer thickness in (b). The dispersion in lateral size and height for dome-shaped QDs were smaller than pyramid-shaped QDs. Figure 3.6 shows the areal density of Ge QDs with different shape as a function of layer thickness. The areal density of pyramid-shaped Ge QDs gradually decrease and dome-shaped Ge QDs became dominant with layer thickness. Larger coalesced Ge QDs accompanying lattice relaxation [32] were observed in layer thickness over 7.0 ML. These results indicates that layer thickness from 4 to 6 ML is appropriate to grow Ge QDs on Si(001) substrates.

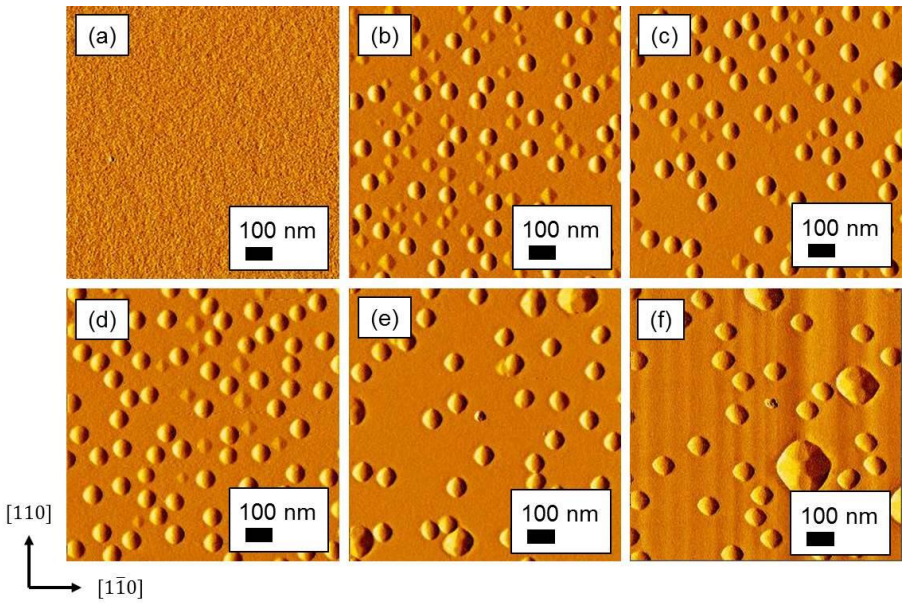

Fig. 3.4: 1 × 1 μm^2 AFM images of single Ge QDs on Si(001) substrates with layer thickness of (a) 3.9 ML, (b) 4.6 ML, (c) 5.3 ML (d) 6.0 ML, (e) 7.0 ML, and (f) 7.8 ML.

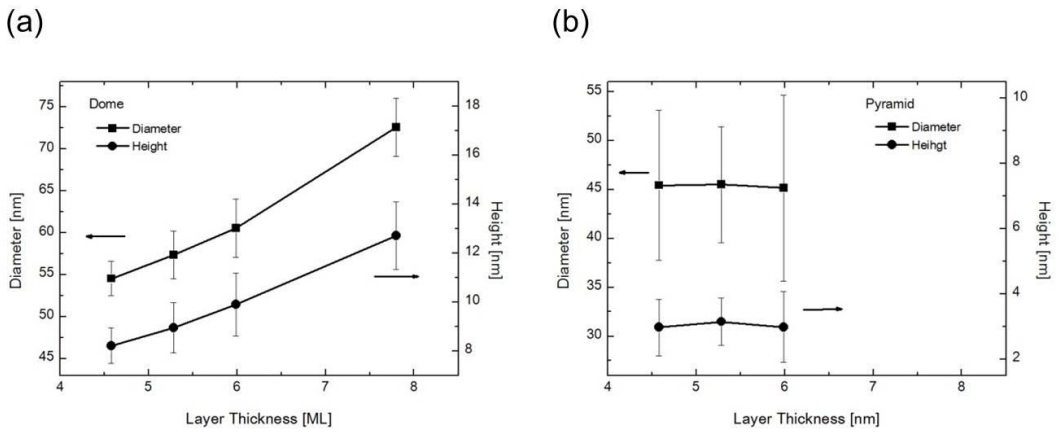

Fig. 3.5: Lateral size and height of (a) dome-shaped QDs and (b) pyramid-shaped QDs as a function of layer thickness.

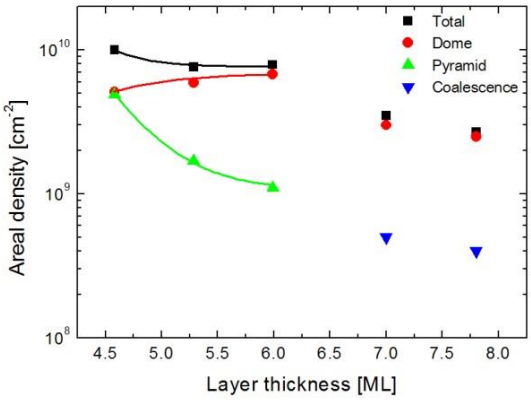

Fig. 3.6: Dependence of areal density for different shape Ge QDs on layer thickness.

The transition from pyramid-shaped QDs to dome-shaped QDs is explained in total energy of faceted islands [29]. The shape of pyramid is energetically favored in initial stage, since energy of pyramid-shaped QDs (E_P) is smaller than that of dome-shape QDs (E_D). Once volume exceeds some critical volume, the E_D become smaller than E_P so dome-shaped QDs is favored in ticker layer thickness. The energy of QDs with different shape (E) is described by [33]:

$$E = V^{2/3}\alpha^{4/3} - V\alpha \quad (3.2)$$

, where V is the volume in scaled units, and α is the ratio of the facet angle to an arbitrary reference angle. The first term relates to surface energy of QDs, whereas the second term associates with volume energy of QDs. For QDs with less volume, the energy E can be reduced by QDs with few facet and smaller facet angle to surface. On the other hand, generation of QDs with many facet and larger facet angle is allowed for much volume. Therefore, pyramid-shaped disappears and dome-shaped Ge QDs become dominant with increase in layer thickness.

3.3. Pulse growth method

Next, we investigated the effect of growth temperature on structural properties of Ge QDs on Si(100) substrates. Figure 3.7 shows AFM images of single Ge QDs on Si(001) substrate grown at (a) 560 °C, (b) 530 °C, (c) 500 °C and (d) 470 °C. The layer thickness of Ge is 5.0 ML. Average height, average lateral size, dispersion in lateral size and areal density were 6.1 nm, 51.4 nm, 14.3% and 1.8×10^9 cm^{-2} for (a), 5.8 nm, 50.3 nm, 27.9% and 5.8×10^9 cm^{-2} for (b), 2.4 nm, 35.2 nm, 24.9% and 2.5×10^{10} cm^{-2} for (c), and 1.1 nm, 21.6 nm, 16.3% and 5.9×10^{10} cm^{-2} for (d), respectively. The height and lateral size decreased with decreasing temperature. Fluctuation in lateral size is around 20% and maximum at 530 °C. Areal density increased with decrease in growth temperature. Small and dense QDs are ascribed to suppressed surface migration of Ge adatoms. In epitaxial growth, adatoms randomly migrate by hopping potential energy E_m created by surface atoms. The hopping rate to neighbor adsorption position $1/\tau$ is given by Eq. (3.1). Lower substrate temperature results in suppression of the migration. The suppressed migration leads to generation of many nuclei in smaller region. Therefore, decrease in QD size and increase in areal density were observed with decrease in temperature.

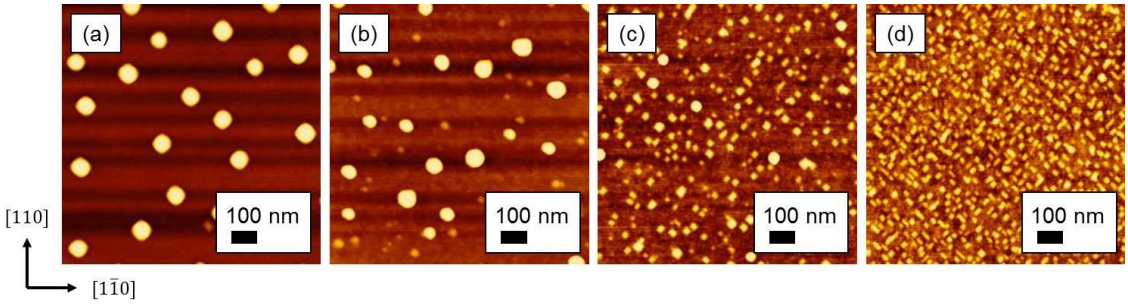

Fig. 3.7: 1×1 μm^2 AFM images of single Ge QDs on Si(001) substrate grown at (a) 560 °C, (b) 530 °C, (c) 500 °C and 470 °C.

The Ge QDs grown at 500 °C showed higher areal density but lower uniformity in lateral size. To improve the size uniformity, we then focused on deposition rate of Ge. Figure 3.8 shows AFM images

of 5.0 ML-thick single layer Ge QDs on Si substrate grown at 500 °C and rate of (a) 1.1 Å/s, (b) 1.4 Å/s, (c) 2.2 Å/s, and (d) 2.8 Å/s. The growth interruption for 30 seconds was employed for all samples by referring [25]. Figure 3.9 shows the lateral size distribution of the Ge/Si QDs. The structural parameters as a function of deposition rate are illustrated in Fig. 3.10. Both pyramid-shaped and dome-shaped Ge/Si QDs were observed in Fig 3.7 (a)-(c), which results in bimodal size distribution as shown in Fig 3.8 (a)-(c). There were no dome-shaped Ge/Si QDs in Fig. 3.7 (d) and thus monomodal size distribution was observed in Fig. 3.8 (d). Height and lateral size decreased with deposition rate, while areal density increased. Fluctuation in lateral size was about 20% from 1.1 to 2.2 Å/s due to bimodal size distribution and 11.1% for Ge/Si QDs grown at rate of 2.8 Å/s. High density of $\sim 5 \times 10^{10}$ cm^{-2} and smaller size fluctuation of 11% were obtained by using deposition rate of 2.8 Å/s. The smaller and denser Ge/Si QDs with better uniformity in lateral size would be caused by shorten migration length of adatoms. In general, the growth conditions such as growth temperature and deposition rate strongly affect the surface migration of Ge adatoms on the Si surface. It was reported that the deposition of Ge at high rates promotes nucleation owing to high concentration of Ge adatoms, viz. short migration length of Ge adatoms [26]. Therefore, the surface migration of Ge adatoms was effectively suppressed for the sample shown in Fig. 3.8 (d), leading to the formation of metastable pyramid-shaped QDs.

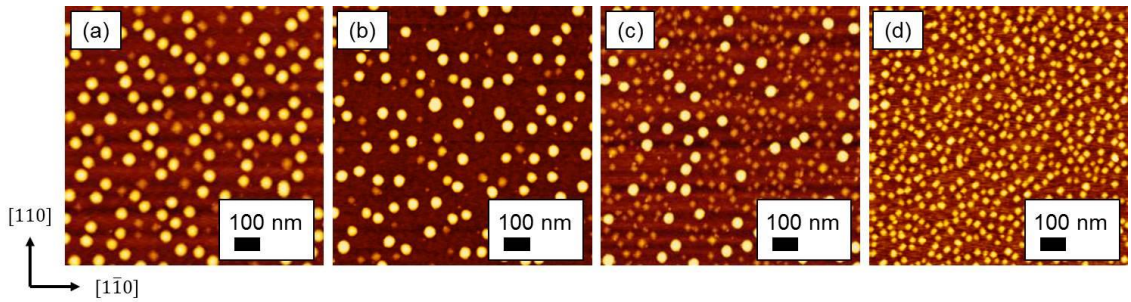

Fig. 3.8: 1 × 1 μm^2 AFM images of single Ge QDs on Si(001) substrate grown at 500 °C and rate of (a) 1.1 Å/s, (b) 1.4 Å/s , (c) 2.2 Å/s and (d) 2.8 Å/s.

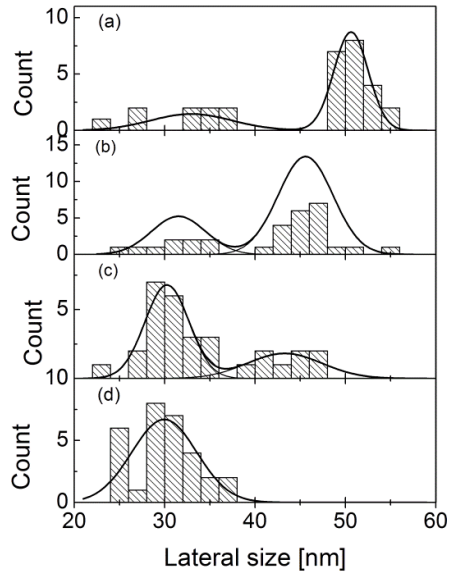

Fig. 3.9: Lateral size distribution of Ge/Si QDs grown at rate of (a) 1.1 Å/s, (b) 1.4 Å/s, (c) 2.2 Å/s and (d) 2.8 Å/s.

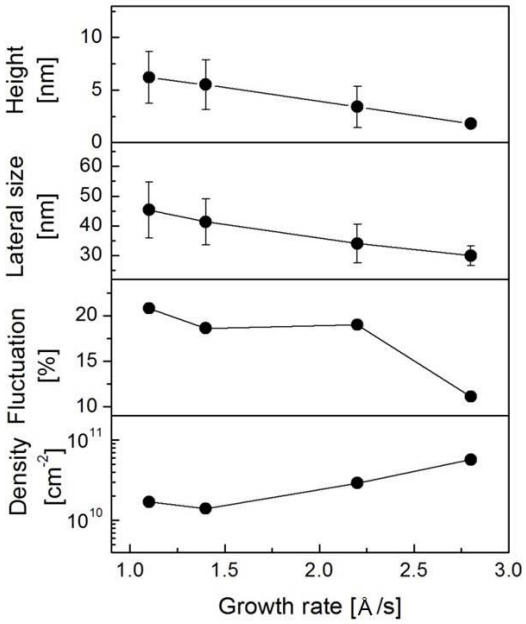

Fig. 3.10: Dependence of deposition rate on structural parameters.

Then, the effect of growth interruption was investigated to check stability of the dense and uniform Ge QDs. Figure 3.11 shows AFM images of single Ge QDs layer grown on Si(001) substrates at 500 °C and rate of 2.8 Å/s with growth interruption for (a) 5, (b) 15 and (c) 30 seconds. The height, lateral size, and fluctuation in size and areal density are summarized in Fig. 3.12. For all samples, significant change was not observed in Fig. 3.11. The average height, average lateral size, fluctuation in lateral size and areal density were almost identical values of about 2 nm, 28 nm, 11% and 6 $\times 10^{10}$ cm^{-2}, respectively. This indicates that the surface morphology is not affected by the growth interruption until 30 seconds possibly due to both suppression of Ge migration at relatively low growth temperature of 500 °C. Thus, evolution of Ge QDs was suppressed owing to energetically stable facet.

We roughly estimated confinement energy of self-assembled Ge QDs grown by pulse growth. The average height and lateral size were about 2 and 30 nm, respectively. According to [34], quantum confinement of carriers in the rather flat shape of Ge/Si nanostructures is comparable to the case of quantum well films, which means strong quantization occurred in growth direction, i.e. height, and

weaker carrier confinement in lateral direction. So it is reasonable to calculate confinement energy in growth and lateral direction separately. The quantized energy level of heavy-hole (hh) locates above 100 meV lower than valence band maximum of Ge, viz. confinement energy is about 600 meV, in case of height of 2 nm. Assuming a parabolic lateral potential, the confinement energy in lateral direction is roughly given by the harmonic oscillator frequency $\hbar\omega$ [34],

$$\frac{1}{2}m^{\parallel}\omega^2\left(\frac{d}{2}\right)^2 = V_0 \tag{3.3}$$

, where $m^{\parallel}$, d and V_0 are effective hole mass in the lateral direction, lateral size and effective band offset of valence band. The $m^{\parallel}$, d and V_0 are 5.18×10^{-32} kg for heavy-hole, 30 nm and 300 meV for Ge QDs of 2 nm height, thus the lateral confinement energy was about 13 meV using an effective mass of bulk Ge. Holes are confined in Ge in lateral direction, however the confinement energy in lateral direction is exceedingly small so the fabricated self-assembled QDs seems to behave quantum well like dots.

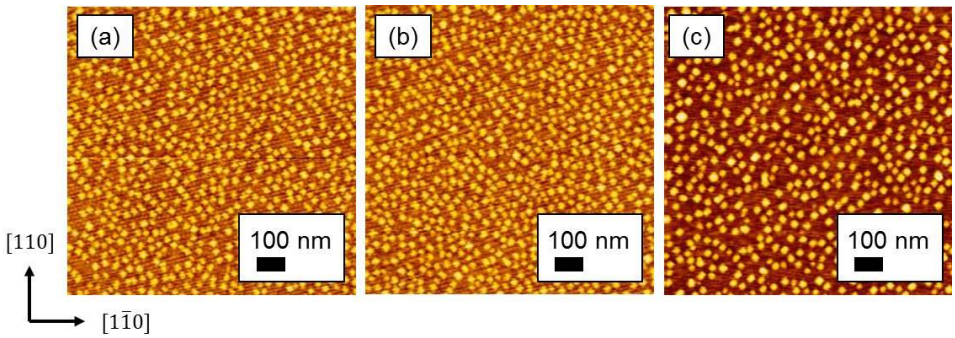

Fig. 3.11: 1×1 μm^2 AFM images of single Ge QDs on Si substrates grown at 500 °C and rate of 2.8 Å/s with growth interruption for (a) 5, (b) 15 and (c) 30 seconds.

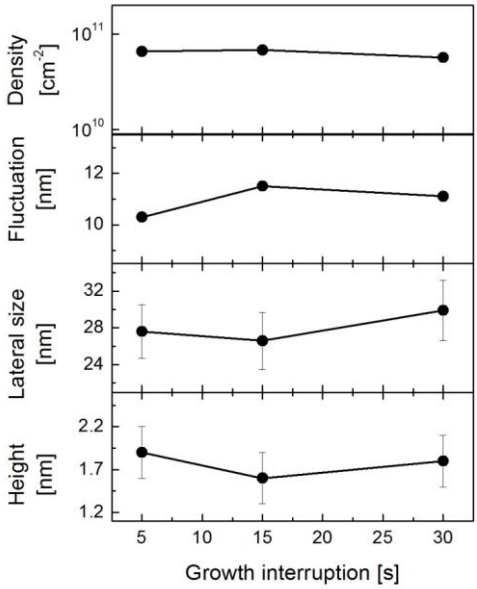

Fig. 3.12: Structural parameters as function of growth interruption.

3.4. Capping self-assembled Ge quantum dots by Si

Multiple stacking of self-assembled Ge QDs is essential to enhance absorption of photons in QD layers. To stack the Ge QD layers, the Ge QDs should be covered by Si before growth of next QD layer. So we investigated how Si layer thickness is necessary to cap Ge QDs. After formation of Ge QDs grown at 500 °C and rate of 2.8 Å/s, growth interruption was employed for 5 seconds and then Si layer was grown at 500 °C and rate of 2.5 Å/s, i.e. small Ge QDs with high density and better uniformity are formed as previously shown. Figure 3.13 shows AFM images of surface for samples grown at Si layer thickness of (a) 2, (b) 6 and (c) 10 nm in addition to RHEED images for respective samples for Si layer thickness of (e) 2, (f) 6 and (g) 10 nm. Furthermore, (d) and (h) show AFM image of a Si(001) substrate and RHEED image of sample before growth of Ge QDs as references, respectively. The root mean square (RMS) of surface roughness was (a) 0.105, (b) 0.103, (c) 0.096 and (d) 0.206 nm, respectively. The values of RMS are plotted as a function of Si cap layer thickness in Fig 3.14 as well as that of Ge QDs without Si capping. The RMS values were about 0.1 nm for (a)-(c) while that of as-grown Ge QD sample was about 0.6 nm, which indicates atomically smooth surface was obtained by burying Ge QDs. With increasing layer thickness of Si, the RSM slightly decreased. The surface became smoother with increase in layer thickness of Si probably due to approach to lattice constant of Si by thicker Si cap layer. Furthermore, RHEED images showed 2 × 1 reconstructed surface was observed from Si cap layer thickness of 2 nm, since the height of Ge QDs was about 2 nm. These results indicate that exceeding 2 nm-thick Si layer is enough to bury Ge QDs grown at 500 °C and rate of 2.8 Å/s with growth interruption for 5 seconds.

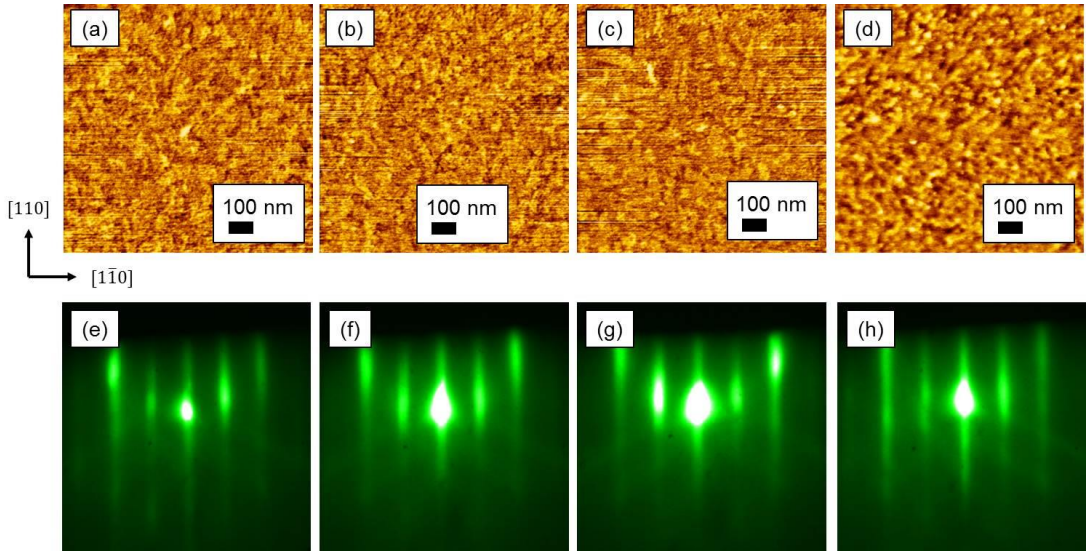

Fig. 3.13: AFM images and RHEED images of surface for Ge QDs buried by Si at layer thickness of 2 nm for (a) and (e), 6 nm for (b) and (f), and 10 nm for (c) and (g), respectively. (d) and (h) shows AFM images of surface for Si(001) substrates and RHEED images for samples before growth of Ge QDs, respectively. The scan size of AFM images was 1 × 1 μm^2.

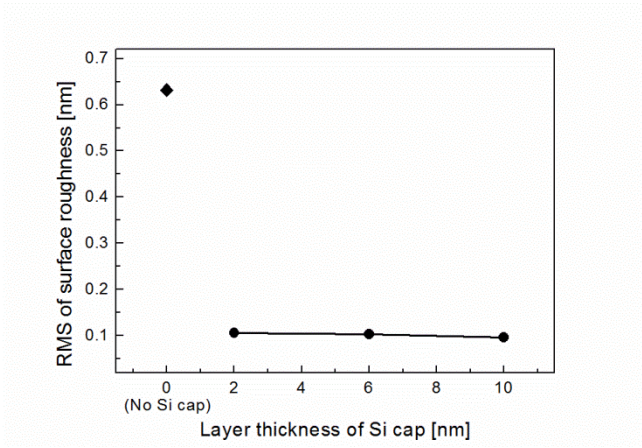

Fig. 3.14: RMS of surface roughness for samples covered by Si at different layer thickness and that of Ge QDs without Si capping.

3.5. Summary

Dense QDs leads to increase in absorption sites of sufficient photons and it is important for solar cells application, so we investigated growth conditions of single layer Ge QDs on Si for high density and high uniformity Ge/Si QDs. By investigating growth conditions, small size uniformity of about 10% and high density of order of 10^{10} are obtained at growth temperature of 500 °C and high deposition rate of 2.8 Å/s. The dense and highly uniform Ge QDs are arisen from suppressed migration of Ge adatoms. The structural parameters were well remained until growth interruption for 30 s, which suggests energetically stable QDs are obtained. The average height of Ge QDs and lateral size were about 2 nm and 30 nm, respectively. The confinement energy in growth and lateral direction are roughly 600 meV and 13 meV, respectively. It is seems that the fabricated Ge QDs behave quantum well like dots. Furthermore, atomically smooth surface and 2 × 1 reconstructed Si surface are observed for 2 nm-thick Si capped Ge QDs, so Si cap layer exceeding layer thick of 2 nm is essential to fabricate multi-stacked Ge QDs.

References

[1] W, Ke-Fan, Z. Yang, Z. Weifeng : Appl. Surf. Sci. **258** (2012) 1935-1939.

[2] A.I. Yakimov, A. V. Dvurechenskii, A. Nikiforov, and Y. Y. Proskuyakov : J. Appl. Phys. **89**, 5676 (2001).

[3] J. Konle, H. Presting, and H. Kibbel: Physica E **16** (2003) 596-601.

[4] A. Protavoce, F. Volpi, A. Ronda, P. Gas, I. Berbezier: Mater. Sci. Eng. **B89** (2002) 205-210.

[5] U. W. Pohl: *Epitaxy of semiconductor* (Springer) chapter 2 and 4.

[6] D. J. Eaglesham and M. Cerullo: Phys. Rev. Lett. **64** (1990) 1943-1946.

[7] M. Grundmann, J. Christen, N. N. Ledentsov, J. Böhrer, D. Bimberg, S. S. Ruvimov, P. Werner, U. Richter, U. Gösele, J. Heydenreich, V. M. Ustinov, A. Yu. Egorov, A. E. Zhukov, P. S. Kop'ev, and Zh. I. Alferov: Phys. Rev. Lett. **74** (1995) 4043-4046.

[8] M. Kawabe, Y. J. Chun, S. Nakajima, and K. Akahane: Jpn. J. Appl. Phys. **36** (1997) 4078-4083.

[9] K. Akahane, T. Kawaura, K. Okino, H. Koyama, S. Lan, Y. Okada, and M. Kawabe: Appl. Phys. Lett. **73** (1998) 3411-3413.

[10] T. Kawamura, K. Akahane, Y. Okada, and M. Kawabe: Jpn. J. Appl. Phys. **38** (1999) 720-723.

[11] J. Zhu, K. Brunner, and G. Abstreiter: Appl. Phys. Lett. **73** (1998) 620.

[12] Y. J. Ma, Z. Zhong, X. J. Yang, and Z. M. Jiang: Nanotechonology **24** (2013) 015304.

[13] C. Dais, G. Mussler, H. Sigg, T. Fromherz, V. Auzelyte, H. H. Solak, and D. Grützmacher: Euro. Phys. Lett. **84** (2008) 67017.

[14] O. G. Schmidt and K. Eberl: Phys. Rev. B **61** (2000) 13721-13729.

[15] V.L. Thanh, V. Yam, P. Boucaud, F. Fortuna, C. Ulysse, D. Bouchier, L. Vervort, and J.-M. Lourtioz: Phys. Rev. B **60** (1999) 5851-5857.

[16] G. Abstreiter, P. Schittenhelm, C. Engel, E. Silveria, A. Zrenner, D. Meettens, and W. Jäger: Semicond. Sci. Technol. **11** (1996) 1521-1528.

[17] G. Costantini, A. Rastelli, C. Manzano, R. Songmuang, O. G. Schmidt, and K. Kern: Appl. Phys. Lett. **85** (2004) 5673-5675.

[18] A. Rastelli, M. Kummer, and H. von Känel: Phys. Rev. Lett. **87** (2001) 256101.

[19] V. A. Markov, H. H. Cheng, C. Chia, A. I. Nikiforov, V. A. Cherepanov, O. P. Pchelyakov, K. S. Zhuravlev, A. B. Talochkin, E. McGlynn, M. O. Henry: Thin Solid Films **369** (2000) 79-83.

[20] N. Motta, A. Sgarlata, R. Calarco, J. Castro Cal, Q. Nguyen, P. Prosposito, A. Balzarotti, and M. De. Crescenzi: J. Vac. Sci. Technol. B **16** (1998) 1555-1559.

[21] H. Omi, and T. Ogino: Phys. Rev. B 59 (1999) 7521-7528.

[22] M. Grydlik, G. Langer, T. Fromherz, F. Schäffler, and M. Brehm: Nanotechnology **24** (2013) 105601.

[23] Z. Zhong, and G. Bauer: Appl. Phys. Lett. **84** (2004) 1922-1924.

[24] K. Nakajima: “epitaxitialseichounomekanizumu (Mechanizm of Epitaxial Growth)” (Kyouritsu, 2002) chapter 4.
[25] T. Sugaya, T. Amano, M. Mori, S. Niki, and M. Kondo Jpn. J. Appl. Phys. **49** (2010) 030211.
[26] A.I. Yakimov, N. I. Nikiforov, A. V. Dvurechenskii, V. V. Ulyanov, A. V. Volodin, R. Groetzschel: Nanotechnology **17** (2006).
[27] G. Costantini, A. Rastelli, C. Manzano, R. Songmuang, O. G. Schmidt, and K. Kern: Appl. Phys. Lett. **85** (2004) 5673-5675.
[28] A. Rastelli, M. Kummer, and H. von Känel: Phys. Rev. Lett. **87** (2001) 256101.
[29] V. A. Markov, H. H. Cheng, C. Chia, A. I. Nikiforov, V. A. Cherepanov, O. P. Pchelyakov, K. S. Zhuravlev, A. B. Talochkin, E. McGlynn, M. O. Henry: Thin Solid Films **369** (2000) 79-83.
[30] I. Daruka and J. Tersoff: Phys. Rev. B **66** (2002) 132104.
[31] I. Daruka, J. Tersoff, and A.-L. Barabási: Phys. Rev. Lett. **82** (1999) 2753-2756.
[32] Y. Shiraki and N. Umasi: “*Silicon-germanium (SiGe) nanostructures*” (Woodhead, 2011) Chapter5.
[33] F. M. Ross, J. Tersoff, and R. M. Tromp: Phys. Rev. Lett. **80** (1998) 984-987.
[34] K. Brunner: Rep. Prog. Phys. **65** (2002) 27-72.

Chapter 4. Multi-stacked Ge QDs in Si Matrix

In this chapter, fabrication of multi-stacked Ge QDs in Si matrix is described. The multi-stacked QDs are essential to absorb sufficient photons in each QD layer. The effect of number of stacks was studied for the multi-stacked Ge/Si QDs fabricated by employing pulse growth technique consisted of high deposition rate of 2.8 Å/s and growth interruption of 5 seconds. Additionally, influence of spacer layer thickness on structural and optical properties of multi-stacked Ge/Si QDs was investigated.

4.1. Fabrication of multi-stacked Ge/Si QDs

For solar cells application, multi-stacked QDs are necessary to absorb photons in each QD layer so we tried to fabricate multi-stacked QD structure. To investigate the effect of new growth conditions using high deposition rate of 2.8 Å/s, we fabricated multi-stacked Ge/Si QDs with spacer layer thickness of 40 nm by comparing two growth conditions: conventional growth and new growth methods. Although the fabrication procedure is same with previously described in Chapter 2, different growth conditions were employed during growth of multi-stacked Ge QDs. The conventional growth condition employed growth temperature of 560 °C, low deposition rate of 0.2 Å/s and layer thickness of 6.0 ML, named as ‘continuous growth’, while new growth condition used growth temperature at 500 °C, high deposition rate of 2.8 Å/s and layer thickness of 5.0 ML, and growth interruption for 5 seconds on the basis of our newly developed method, named as ‘pulse growth’.

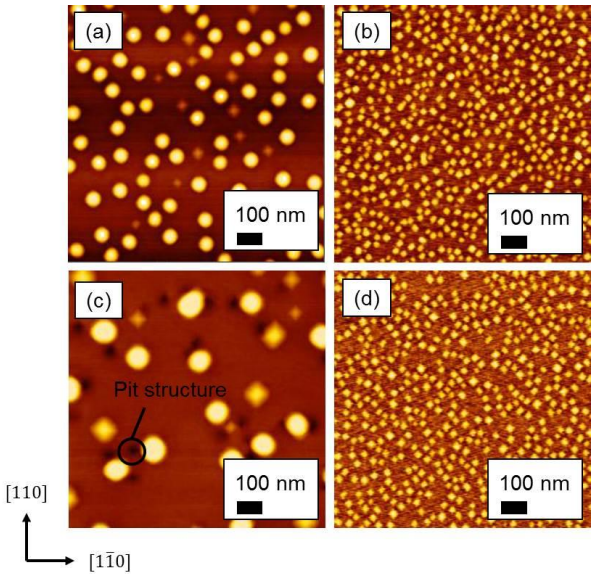

Fig. 4.1: 1 × 1 μm^2 AFM images of (a, b) single Ge QDs and (c, d) 20-layer-stacked on Si substrate grown by continuous and pulse growth method, respectively.

Figure 4.1 shows 1 × 1 μm^2 AFM images of single layer Ge/Si QDs grown using (a) continuous growth and (b) pulse growth methods. The average lateral size, average height, dispersion in lateral size and areal density were 60.4 nm, 9.9 nm, 6.7% and 7.2 × 10^9 cm^2 for (a), and 29.9 nm, 1.8 nm, 11.1% and 5.6 × 10^{10} cm^2 for (b), respectively. In general, both a high deposition rate and a low growth temperature significantly depressed the surface migration length of Ge adatoms, leading to the generation of high-density nuclei to form QDs. However, it seems to be almost no difference in size dispersions of 10% for each QD sample, which suggests that QDs were self-assembled under the influence of a different simple dominant facet in each condition. Fig. 4.1(c) and (d) shows 1 × 1 μm^2 AFM images of topmost surface for 20-layer-stacked Ge QDs grown using continuous and pulse methods, respectively. Further, the dependence of average QD lateral size, height, size dispersion and areal density of the topmost QDs on the stack number for the sample grown by each growth method are summarized in Fig. 4.2. Both QD size and lateral size dispersion increased with the increase in the number of stacks for QDs grown using the continuous growth technique. On the other hand, these

parameters remained constant for QDs grown using the pulse growth technique even after 20 layers of stacking. Additionally, high-density pit-structures associated with threading dislocations propagating to the surface were clearly observed near the QDs in Fig. 4.1 (c). As a result, highly uniform 20-layer-stacked Ge/Si QDs with a high areal density were fabricated using the pulse growth method.

Figure 4.3 shows HAADF-STEM images of 20-layer-stacked Ge/Si QDs grown by (a) continuous growth and (b) pulse growth method. The inset in Fig. 4.3 (b) shows magnified view of top portion of 20-layer stacked Ge/Si QDs. Vertically aligned QD structure was clearly observed in Fig. 4.3 (a). The QD size became larger with increasing the number of stacks for (a). Furthermore, it was notable that dislocations were generated around the QDs after 8 layers of stacking in (a), because a larger QD generates a stronger strain field around it resulting in the critical thickness being exceeded locally [1]. However, we did not observe simultaneously the generation of dislocations and a vertical correlation between the regions above and below the QDs as shown in Fig. 4.3 (b). In comparison with QDs grown using the conventional growth method, QDs grown using the pulse growth method generate spatially averaged strain fields due to the formation of small, high density QDs [1]. These results strongly supported AFM observations mentioned above.

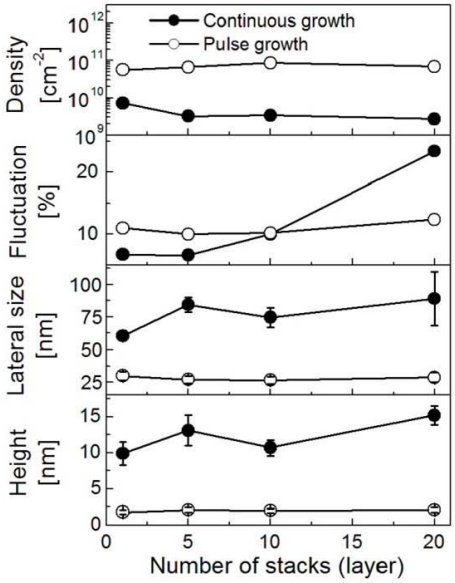

Fig. 4.2: Dependence of structural parameters on number of stacks for multi-stacked Ge/Si QDs grown by continuous growth and pulse growth.

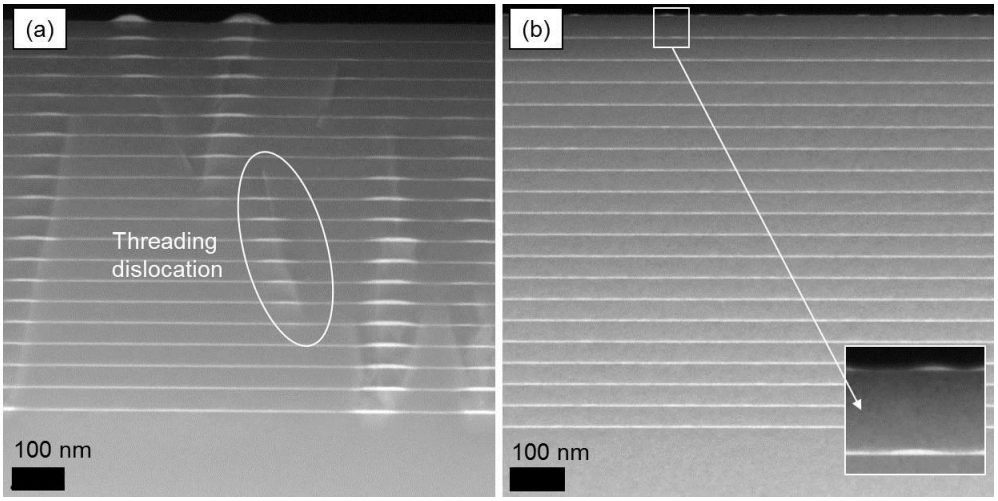

Fig. 4.3: Cross-sectional HAADF-STEM images for 20-layer-stacked Ge/Si QDs grown by (a) continuous growth and (b) pulse growth. The inset in (b) is an enlarged image of top portion.

Figure 4.4 shows PL spectra for 20-layer-stacked QDs grown by continuous growth and pulse growth methods. PL emissions at around 1.08 eV come from Si substrate or Si spacer layers. The PL linewidth of Si in continuous growth was larger than that in pulse growth probably due to

interdiffusion of Ge caused by higher growth temperature or degradation of crystal quality induced by dislocations. PL emission peak from 0.9-1.0 eV would be dislocation related PL emissions [2]. PL emissions of 0.8 eV arise from Ge QDs. These PL emission peaks are consistent with previous work [3-6]. The PL peak energy and PL linewidth were 0.806 eV and 98.7 meV for continuous growth, and 0.833 eV and 71.2 meV for pulse growth, respectively. PL intensity of Ge/Si QDs grown by pulse growth is twenty times stronger than that of continuous growth. The blue-shifted PL peak energy was observed for Ge/Si QDs grown by pulse growth probably due to quantum size effect caused by smaller size Ge/Si QDs. Narrower PL linewidth was obtained for 20-layer-stacked Ge/Si QDs grown by pulse growth. These results indicate that better crystal quality was obtained by using pulse growth technique.

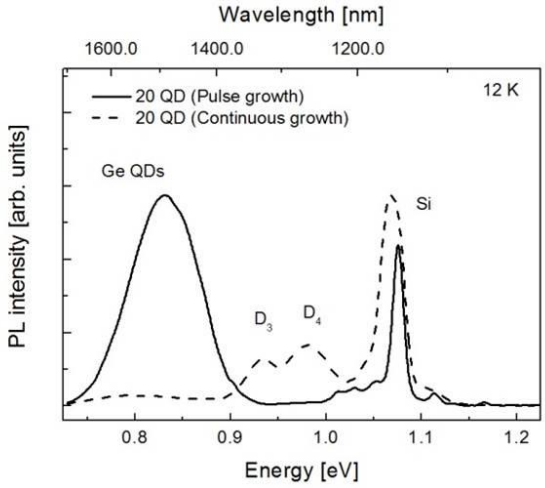

Fig. 4.4: PL spectra measured at 12 K for 20-layer-stacked Ge/Si QDs grown by continuous growth (dotted line) and pulse growth (solid line). The representatives of Si, Ge QDs, indicates Si and Ge QDs related PL emission peak. PL emission peaks of the D_3 and D_4 associate with dislocations.

4.2. Dependence on number of stacks

Next, we tried to fabricate highly-stacked QD structure because highly stacked QD structure is important to absorb photons in QD layers. Figure 4.5 shows AFM images of topmost surface for (a) 25, (b) 50, (c) 75 and (d) 100-layer-stacked Ge/Si QDs with spacer layer thickness of 30 nm on Si(001) substrates. Pyramid-shaped Ge/Si QDs were successfully maintained up to 100-layer-stack. Figure 4.6 shows structural parameters as a function of number of stacks. Height and lateral size were around 2.0 nm and 32.5 nm, respectively. Fluctuation in lateral size was less than 10%. Sheet density was on the order of 10^{10} cm^{-2}. Structural parameters were almost identical for all samples. Furthermore, reciprocal space mapping around (224) are given in Fig. 4.7. The axes are reciprocal space vector coordinates and those are related to *hkl* units. The X-ray peak of Si and satellite peaks (L) of 100-layer-stacked QDs were vertically aligned, which indicates the relaxation of strain is entirely zero [7,8]. Figure 4.8 shows (a) cross-sectional HAADF-STEM images for 100-layer-stacked Ge/Si QDs in addition to enlarged HAADF-STEM images of (a) top, (b) middle and (c) bottom portion of the 100-layer-stacked Ge/Si QDs. The difference of the contrast intensity in Fig. 4.8 (b)-(d) would be caused by different sample thickness in the direction to transmitting electrons. Ge QDs can be seen with a lateral size of ~25 nm and a height of ~2 nm. Dislocations were not observed after 100-stacks. These results indicate that no strain relaxation happened, which is good agreement with results of X-ray diffraction.

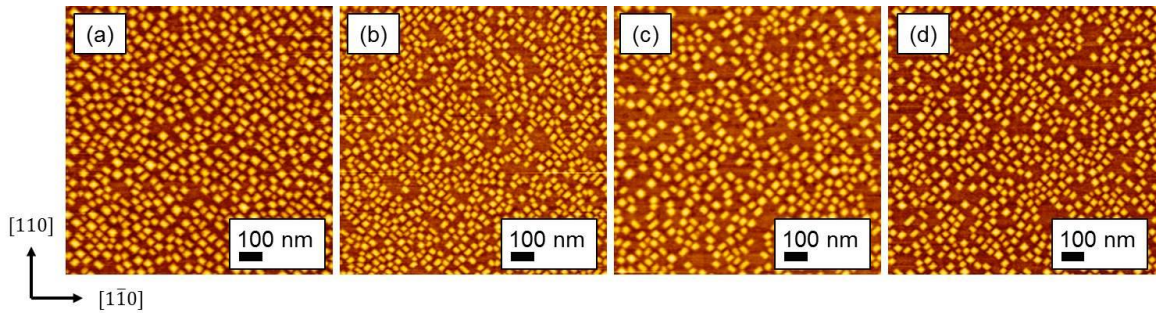

Fig. 4.5: 1 × 1 μm^2 AFM images of topmost surface for (a) 25, (b) 50, (c) 75 and (d) 100-layer-stacked Ge/Si QDs grown by new growth technique.

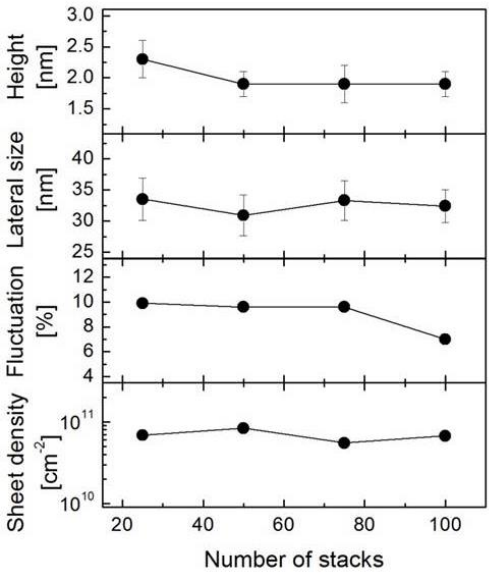

Fig. 4.6: Structural parameters of multi-stacked Ge/Si QDs as a function of number of stacks.

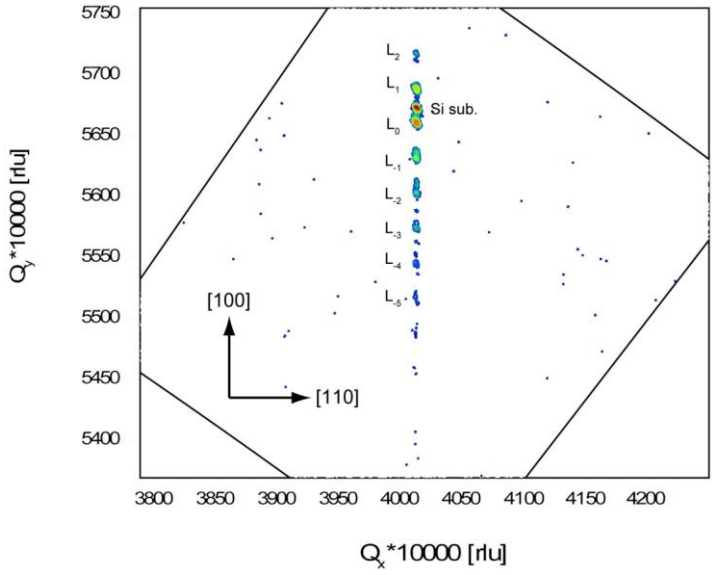

Fig. 4.7: Reciprocal space mapping (RSM) around 224 for 100-layer-stacked QDs.

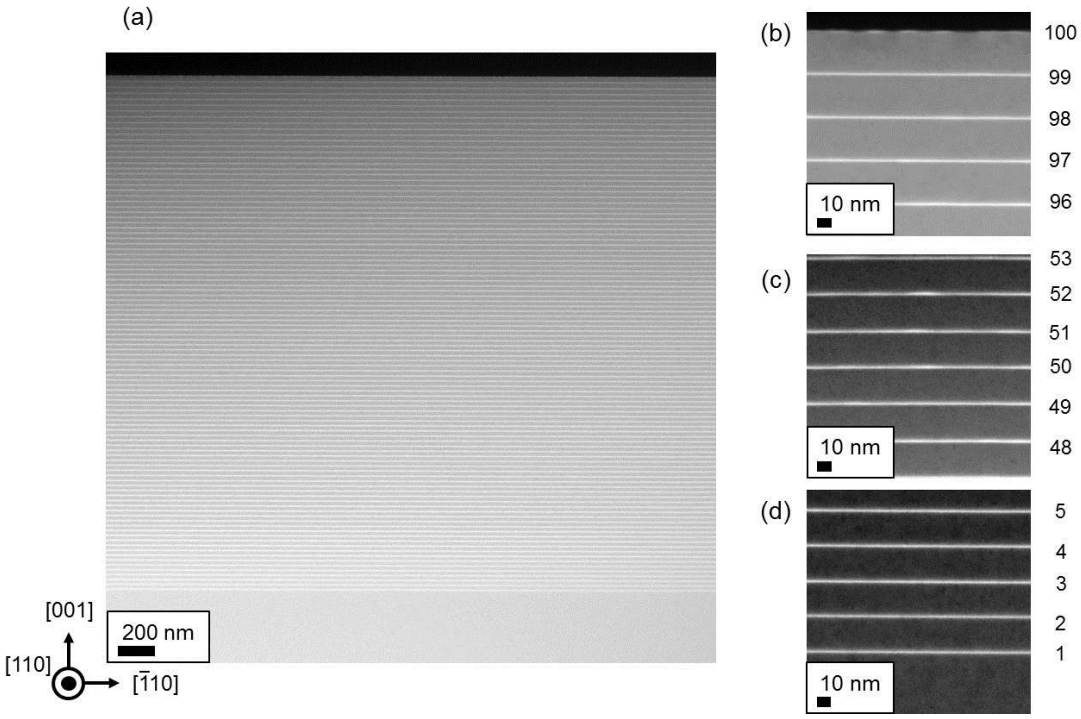

Fig. 4.8: (a) Cross-sectional HAADF-STEM images for 100-layer-stacked Ge/Si QDs. Enlarged STEM images of (b) top, (c) middle and (c) bottom portion of 100-layer-stacked Ge/Si QDs.

Figure 4.9 shows PL spectra for 25, 50, 75 and 100-layer-stacked Ge/Si QDs with spacer layer thickness of 30 nm. PL emission peak from Ge/Si QDs was clearly observed for all samples. The PL peak intensity, peak energy and line width are summarized in Fig. 4.10. The PL intensity became stronger in proportion to number of stacks, while the PL peak energy of 0.8 eV and the PL linewidth of 90 meV were almost constant for all the samples. Therefore, crystal quality of Ge/Si QDs was not deteriorated even in 100-layer-stacked QD structure.

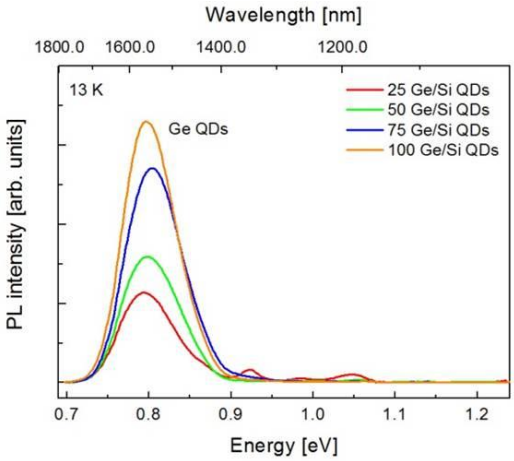

Fig. 4.9: PL spectra for 25, 50, 75 and 100-layer-stacked Ge/Si QDs with spacer layer thickness of 30 nm excited by 532 nm green laser with power of 193.5 mW and at temperature of 12 K.

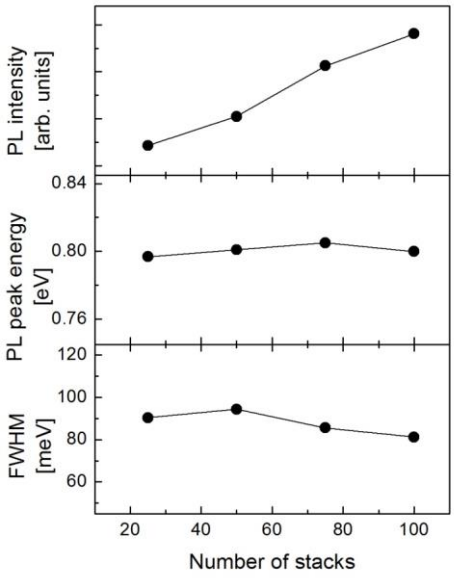

Fig. 4.10: PL peak intensity, peak energy and line width for 25, 50, 75 and 100-layer-stacked Ge/Si QDs with spacer layer thickness of 30 nm.

4.3. Dependence on spacer layer thickness

To create minibands in direction to p-n junction, short inter-dot spacing, i.e. thinner spacer layer thickness in growth direction, is necessary. Thereupon, the effect of spacer layer thickness was investigated. Figure 4.11 shows 5 × 5 μm^2 and 1 × 1 μm^2 AFM images of topmost surface for 20-layer-stacked Ge/Si QDs. The Si spacer layer thickness (d_{SL}) was 40 nm for (a) and (e), 20 nm for (b) and (f), 10 nm for (c) and (g), and 6 nm for (d) and (h). Pyramid-shaped Ge/Si QDs were maintained from d_{SL} = 10 to 40 nm. In Fig. 4.11 (d) and (h), aggregation of Ge QDs were observed due to stronger stain fields established by Ge QDs. Multi-stacked Ge QDs were successfully grown without larger and aggregated Ge islands by using spacer layer thickness until 20 nm. Figure 4.12 shows structural parameters as a function of d_{SL}. Height, lateral size and dispersion in lateral size increased with decrease in d_{SL}, whereas areal density decreased. The lager QD size accompanying with lower density is caused by local strain induced by buried Ge QDs in Si matrix. That is supported by cross-sectional HAADF-STEM images as shown in Fig. 4.13. Misfit dislocations and significant interdiffusion between Si and Ge were not observed in all the samples. We confirmed that the inter-dot spacing fabricated in this study was 38 nm for (a), 18 nm for (b), and 8 nm for (c), since the height of the buried QDs were almost identical value of 2 nm. The QD pairing ratio was used as a parameter to compare the stacking configuration for each sample, with the QDs considered paired if the center of a QD is above the surface occupied by a QD underneath, which equals to number of the paired QDs divided by total number of QD. The pairing ratios of stacked Ge QDs were determined to be 7.1% for (a), 36.0% for (b), and 82.7% for (c). A nucleation site of QDs is generally affected by the strain field caused by underlying QDs [9,10] as well as the step structure of the surface, because the stress on the crystal surface is a natural driving force for nanostructure formation in lattice mismatch growth. The buried Ge QD under Si layer thickness of L at position x = 0 causes the strain fields on surface ε and the relationship of the ε with lateral position x is given in following equation [1]:

$$\varepsilon(x) = C\frac{1}{(x^2 + L^2)^{3/2}}\left[1 - \frac{3L^2}{(x^2 + L^2)}\right] \tag{4.1}$$

, where C is proportional to the volume of the buried QDs, the misfit and the elastic constants. For single buried QD in Si, favored nucleation site is x = 0, which means directly above. Furthermore, thinner Si layer thickness results in stronger strain fields. For many buried QDs in Si, the ε strongly overlap when the average spacing in initial QD layer is smaller than the spacer layer thickness [1] and thus energetically favored nucleation sites decrease. These results suggest that the thicker d_{SL} = 40 nm homogenizes the strain field of the surface before the deposition of Ge, while the local strain field is strong enough to generate a nucleation site just above a QD array in the thinner d_{SL} = 10 nm, resulting in a decrease in areal density.

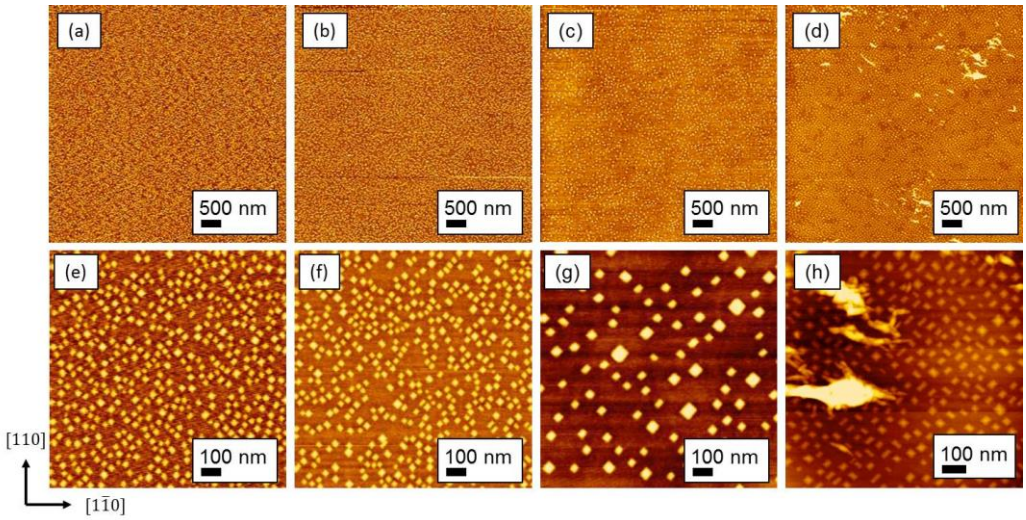

Fig. 4.11: 5 × 5 μm^2 and 1 × 1 μm^2 AFM images of topmost surface for 20-layer-stacked Ge/Si QDs with d_{SL} = (a) and (e) 40, (b) and (f) 20, (c) and (g) 10, and (d) and (h) 6 nm, respectively.

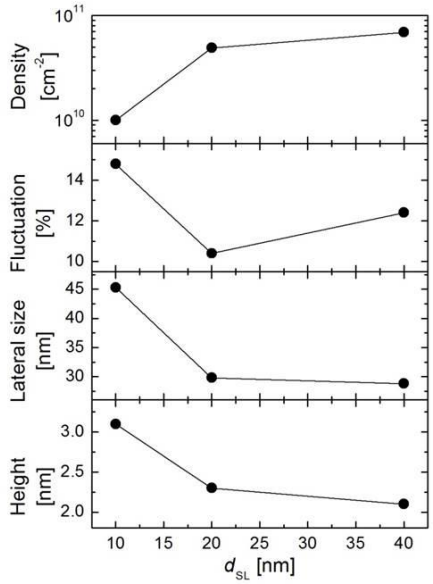

Fig. 4.12: Dependence of Si spacer layer thickness (d_{SL}) on structural parameters.

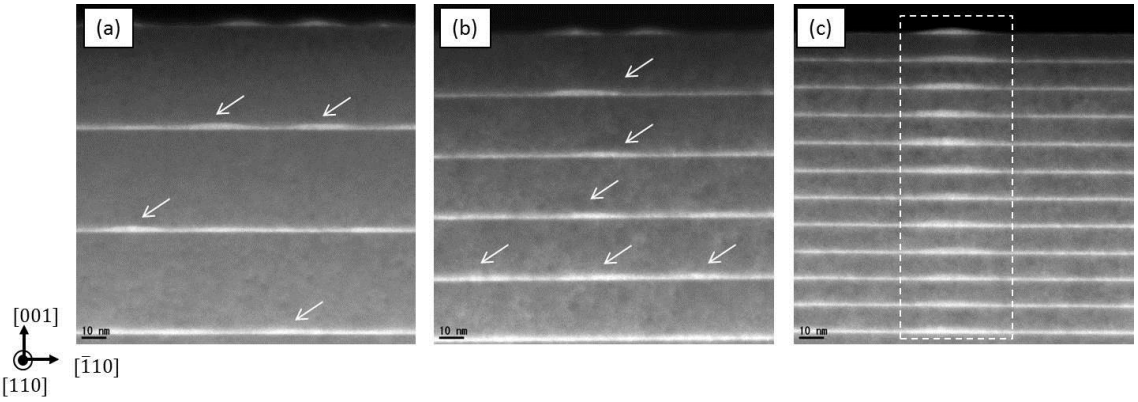

Fig. 4.13: Cross-sectional HAADF-STEM images for the top portion of 20-layer-stacked Ge QDs with d_{SL} = (a) 40 nm, (b) 20 nm and (c) 10 nm.

Figure 4.14 shows the PL spectra for sample with different d_{SL} measured at 12 K. The wavelength and power of excitation source were 532 nm and 97.0 mW, respectively. PL emission peaks at around 0.8 eV and 1.08 eV were observed from Ge QDs and bulk Si, respectively, as mentioned above. The PL emission for sample (d) was extremely weak probably due to defect formation in aggregated QDs. The PL peak energy and full width at half maximum (FWHM) are 0.831 eV and 70.5 meV for (a), 0.829 eV and 68.1 meV for (b), and 0.816 eV and 91.1 meV for (c). The relationship of PL parameters with spacer layer thickness is summarized in Fig. 4.15. Significant decrease in PL intensity was observed in d_{SL} = 10 nm. As d_{SL} decreased, the PL peak energy reduced. The PL peak energy of QDs are generally affected by various factors such as Si-Ge alloying due to interdiffusion [11-13], quantum confinement [8,14], and electronic coupling of QDs [14-16]. If the interdiffusion between Si and Ge is a dominant factor in determining the PL peak energy, it should shift to higher energy according to the change in effective QD size. In structural characterization, strong interdiffusion was not observed in our stacked QD configurations. Thus, the reduction of PL peak energy and broadening of PL emission possibly arises from quantum size effect of larger Ge QDs or electronic coupling of quantum states in vertically stacked Ge/Si QDs.

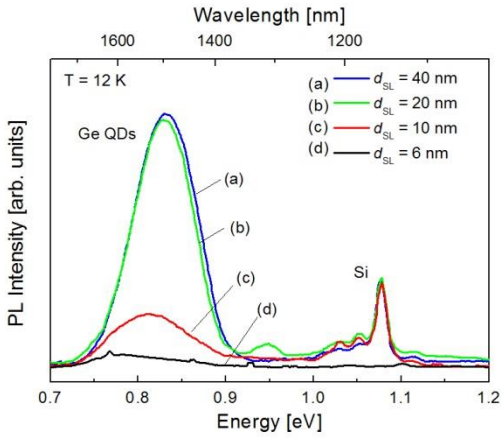

Fig. 4.14: PL spectra for 20-layer stacked Ge QDs with d_{SL} = (a) 40 nm, (b) 20 nm, (c) 10 nm and (d) 6 nm measured at 12 K.

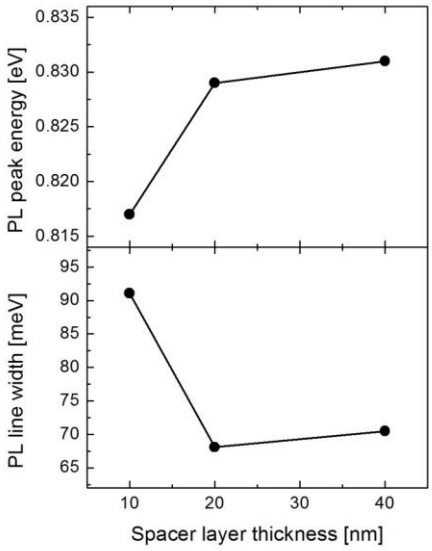

Fig. 4.15: PL peak energy and PL line width as a function of spacer layer thickness.

Figure 4.16 shows PL peak energy as a function of third root of excitation intensity ($(P_{exc})^{1/3}$) for each QD sample. It can be seen that the PL peak energy is proportional to $(P_{exc})^{1/3}$ for all the samples. In general, type-II heterostructures in Ge/Si QDs form a dipole layer at the interface because of spatial separation of holes confined in the Ge QDs and electrons in the Si spacer layer accumulated around the Ge QDs. The accumulated electrons generate quantized energy state of electrons and the energy levels are proportional to the third root of the excitation power [17-20]. On the other hand, PL peak energy of InGaAs/GaAs QDs showing band lineup type-I are independent of excitation power [21]. The relationship between the quantized energy level of the electron and the excitation power are explained by:

$$E_e = b(P_{exc})^{1/3} \tag{4.2}$$

, where b is a factor defined by the following equation [21]:

$$b = \left(\frac{9\pi}{8}\right)^{2/3}\left(\frac{\hbar^2}{2m_e}\right)^{1/3}\left(\frac{2\pi e^2}{\epsilon_0}\right)^{2/3}\left(\frac{\alpha(d_{SL} + d_{QD})^2}{\gamma}\right)^{1/3} \tag{4.3}$$

, where m_e, e, ε_0, α, d_{SL}, d_{QD}, and γ are effective electron mass, elementary charge, dielectric constant,

absorption coefficient, thickness of the spacer layer, thickness of the QD layer, and radiative recombination coefficient, respectively. In our calculation results, *b* values were almost the same for (a) and (b) at 2.03(meV)$^{2/3}$ and 2.31(meV)$^{2/3}$, respectively, while larger for (c) at 5.62 (meV)$^{2/3}$. Most parameters are identical for all samples, except for d_{SL} and γ, though thinner d_{SL} should be responsible for smaller *b*. Therefore, larger *b* for d_{SL} = 10 nm is due to smaller γ, which suggests the radiative recombination coefficient for d_{SL} = 10 nm was reduced. Figure 4.17 shows normalized integrated PL intensity and integrated QD density as a function of d_{SL}. The increasing rate of integrated PL intensity with d_{SL} seems to correspond that of QD density. Thus, the reduction of PL emission intensity as shown in Figures 4.14 is due to the suppression of radiative recombination caused by decreased QD density, which leads to smaller γ and thus larger b. Though, theoretical calculation based on six-band $k \cdot p$ model mentioned that splitting of hole energy state caused by residual strain around Ge QDs may result in appearance of electrically coupled QD states even if the dot separation exceeds 3-4 nm [22], the interconnection of envelope function in Ge/Si system ideally appears from inter-dot spacing of less than 3-4 nm [23-25].

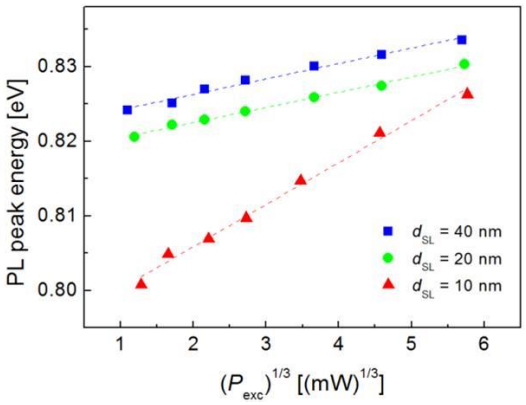

Fig. 4.16: PL peak energy as a function of third root of excitation power for 20-layer-stacked Ge QDs with d_{SL} = 40, 20 and 10 nm at 12 K. The fitted lines are shown as dotted line.

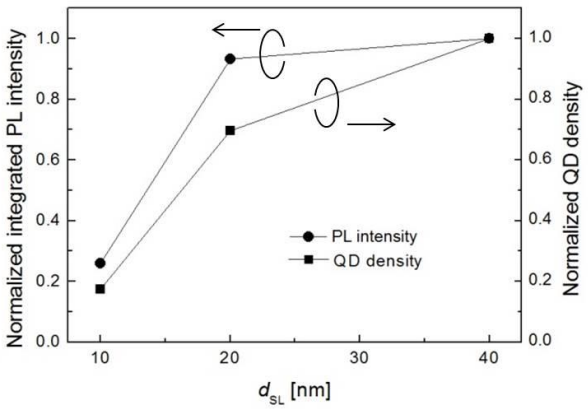

Fig. 4.17: Integrated PL intensity and QD density as a function of d_{SL}. The value for each parameters were normalized by the value at d_{SL} = 40 nm.

4.4. Summary

Multi-stacked Ge/Si QDs with spacer layer thickness of 30 nm were successfully grown up to 100-layer without deterioration of crystal quality by employing the new growth method consisted of high deposition rate of 2.8 Å/s and growth interruption of 5 seconds. Furthermore, larger Ge/Si QDs and aggregated Ge/Si islands were generated for 20-layer-stacked QDs with spacer layer thickness of 10 nm and 6 nm, respectively. Thus, growth of 20-layer-stacked Ge/Si with thicker spacer layer thickness than 20 nm was possible due to both weak strain fields induced by small QDs and diluted strain fields by thicker spacer layer. Vertically aligned QD structure was clearly observed in spacer layer thickness of 10 nm, since the stronger strain field by thin spacer layer thickness. PL excitation power dependence indicated that fabricated Ge/Si QDs were type-II band lineup.

References

[1] J. Tersoff, C. Teichert, and M. G. Lagally: Phys. Rev. Lett. **76** (1996) 1675-1678.

[2] S. Sauer, J. Weber, J. Stolz, E. R. Weber, K.-H. Küsters, and H. Alexander: Appl. Phys. A **36** (1985) .

[3] M. Larsson, A. Elfving, P. O. Holtz, G. V. Hansson, and W. X. Ni, Surf. Sci. **532-535**, 832 (2003).

[4] V. Yam, V. L. Thanh, Y. Zheng, P. Boucaud, and D. Bouchier, Phys. Rev. B **63**, 033313 (2001).

[5] S. Fukatsu, N. Usami, H. Sunamura, Y. Shiraki, and R. Ito, Mat. Res. Soc. Symp. Proc. **448**, 125 (1997).

[6] H. Sunamura, N. Usami, Y. Shiraki, and S. Fukatsu, Appl. Phys. Lett. **66**, 3024 (1995).

[7] E. Kasper, N. Escoubs, J. Werner, Oehme, and K. Lyutovich: J. Appl. Phys. **111**, 63507 (2012)

[8] G. Bauer, J. Li, E. Koppensteiner: J. Cryst. Growth **157** (1995) 61-67.

[9] V. L. Thanh, V. Yam, P. Boucaud, F. Fortuna, C. Ulysse, D. Bouchier, L. Vervoort, and J. M. Lourtioz: Phys. Rev. B **60**, 5851 (1999).

[10] O. G. Schmidt and K. Eberl: Phys. Rev. B **61**, 13721 (2000).

[11] T. Tayagaki, K. Ueda, S. Fukatsu, and Y. Kanemitsu, J. Phys. Soc. Jpn. **81**, 064712(2012).

[12] T. U. Schülli, M. Stoffel, A. Hesse, J. Stangl, R. T. Lechner, E. Wintersberger, M. Sztucki, T. H. Metzger, O. G. Schmidt, and G. Bouer, Phys. Rev. B **71**, 035326 (2005).

[13] J. Wan, Y. H. Luo, Z. M. Jiang, G. Jin, L. Liu, Kang L. Wang, X. Z. Liao, and J. Zou, J. Appl. Phys. **90**, 4290 (2001).

[14] H. Sunamura, S. Fukatsu, N. Usami, and Y. Shiraki, J. Cryst. Growth **157**, 265 (1995).

[15] Y. Shoji, K. Narahara, H. Tanaka, T. Kita, K. Akimoto, and Y. Okada, J. Appl. Phys. **111**, 074305 (2012).

[16] M. K. Zundel, P. Specht, K. Eberl, N. Y. Jin-Philipp, and F. Philipp, Appl. Phys. Lett. **71**, 2972 (1997).

[17] G. S. Solomon, J. A. Terezza, A. F. Marshall, and J. S. Harris, Jr., Phys. Rev. Lett. **76**, 952 (1996).

[18] F. Hatami, M. Grundmann, N. N. Ledentsov, F. Heinrichsdorff, R. Heitz, J. Böhrer, D. Bimberg, S. S. Ruvimov, P. Werner, V. M. Ustinov, P. S. Kop'ev, Zh. I. Alferov, Phys. Rev. B **57**, 4635 (1998).

[19] F. Hatami, N. N. Ledentsov, M. Grundmann, J. Böhrer, F. Heinrichsdorff, M. Beer, D. Bimberg, S. S. Ruvimov, P. Werner, U. Gösele, J. Heyndenreich, U. Richter, S. V. Ivanov, B. Y. Meltser, P. S. Kop'ev, Z. I. Alferov, Appl. Phys. Lett. **67**, 656 (1995).

[20] N. N. Ledentsov, J. Böhrer, M. Beer, F. Heinrichsdorff, M. Grundmann, D. Bimberg, S. V. Ivanov, B. Y. Meltser, S. V. Shaposhnikov, I. N. Yassievich, N. N. Faleev, P. S. Kop'ev, and Z. I. Alferov, Phys. Rev. B **52**, 14058 (1995).

[21] T. Sugaya, T. Amano, M. Mori, and S. Niki: Appl. Phys. Lett. **97** 043112 (2010).

[22] A. I. Yakimov, A. A. Bloshkin and A. V. Dvurechenskii, Semicond. Sci. Technol. **24**, 095002 (2009).

[23] W. Hu, M. M. Rahman, M. Lee, Y. Li, and S. Samukawa: J. Appl. Phys. **114**, 124509 (2013).

[24] V. G. Talalaev, G. E. Cirlin, A. A. Tonkikh, N. D. Zakharov, P. Werner, U. Gösele, J. W.Tomm, and T. Elsaesser: Nanoscale Res. Lett. **1**, 137 (2006).

[25] O. L. Lazarenkova and A. A. Balandin: J. Appl. Phys. **89**, 5509 (2001).

Chapter 5. Ge QDs in $Si_{1-x}C_x$ Matrix for Strain Compensation

This chapter presents results of fabrication of $Ge/Si_{1-x}C_x$ QDs. To form minibands in direction to p-n junction, growth of multi-stacked QDs with thinner spacer layer thickness thinner than ~4 nm is necessary. QDs are able to couple electrically due to short inter-dot spacing and thus minibands is formed. In chapter 4, 20-layer-stacked Ge/Si QDs with spacer layer thickness of 20 nm were grown, however increase in QD size and aggregation of QDs were observed in the thickness thinner than 10 nm due to stronger strain fields induced by Ge QDs. To improve this problem, we focused on the strain compensation technique which is possible to compensate the QD induced compressive strain by tensile stress in spacer layer. For Ge QDs on Si substrates, $Si_{1-x}C_x$ spacer layer are able to be strain compensating spacer layer. By employing $Si_{1-x}C_x$ spacer layer, it is possible to fabricate electrically coupled, multi-stacked QDs without aggregation of QDs. For this reason, we grew $Si_{1-x}C_x$ layer on Si(001) substrates firstly. Next, Ge QDs were grown on $Si_{1-x}C_x$ layers. Then, multi-stacked $Ge/Si_{1-x}C_x$ QDs were fabricated. The effect of spacer layer thickness on multi-stacked $Ge/Si_{1-x}C_x$ QDs was studied.

5.1. Introduction

As described in Chapter 1, thinner spacer layer thickness is critical to form minibands in growth direction, however it is difficult to fabricate multi-stacked QD structure with thin spacer layer thickness since self-assembled QDs accompany the strain arisen from difference of lattice constant in hetero epitaxial growth. Both crystalline Si and Ge are diamond lattice structure and the lattice constant of Ge and Si are 5.431 Å and 5.657 Å, respectively. In hetero epitaxial growth of Ge on Si, in-plane lattice constant of Ge corresponds to lattice constant of Si, meanwhile out-plane lattice constant become larger due to elastic deformation induced by compressive strain. The schematics of

hetero epitaxial growth of Ge on Si are illustrated in Fig. 5.1. The lattice mismatch f is quantitative measure of structural difference between the epitaxial films and substrates, which is defined as the relative differences of the lattice constants of the film (a_{f}) and the substrate (a_{s})

$$f = \frac{a_{\mathrm{f}} - a_{\mathrm{s}}}{a_{\mathrm{s}}} \tag{5.1}$$

in case of hetero epitaxial growth of Ge on Si, f = 4.2 %.

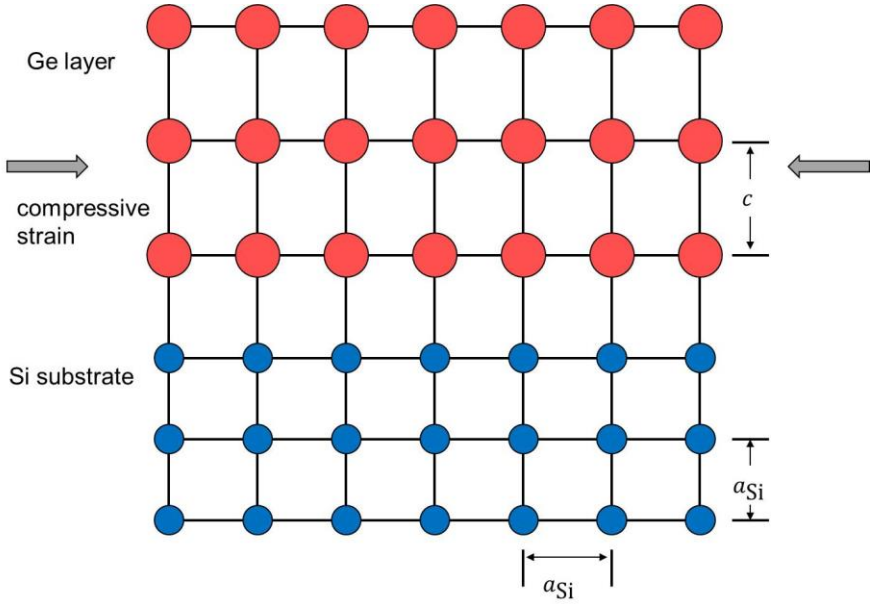

Fig. 5.1: Schematic image of interface in hetero-epitaxial growth of Ge on Si. The a_{Si} and c are common lateral lattice constant of Si, elastically deformed vertical lattice constant of Ge, respectively.

The lattice mismatch limits stacking QD layers up to some critical layer thickness. Once exceeding the critical thickness, bond breaking and dislocation is preferred due to relaxation of accumulated stress. Self-assembled QDs create the inhomogeneous strain fields which affects growth of QDs on above layer [1]. In particular, it is notable when spacer layer thickness between QD layers becomes thinner. Consequently, QD size becomes larger until generation of dislocation.

To prevent increase in QD size and generation of dislocations, strain compensated technique is developed. In the strain compensated multi-stacked QD structure, tensile stress in spacer layer

compensates the compressive stress established by the QDs [2,3]. The schematic concept of strain compensated QD structure is shown in Fig. 5.2. For generating tensile stress in spacer layer, the spacer layer should possess smaller lattice constant than substrate. So far, the strain compensation is demonstrated in InAs/InAlGaAs QDs on InP(311) substrates [4], InAs/GaNAs QDs on GaAs(001) [5,6]. By employing strain compensation technique, highly-stacked QDs with better crystal quality are achieved without increase in QD size and generation of dislocation. Hence, the technique improved properties of solar cells [7-9].

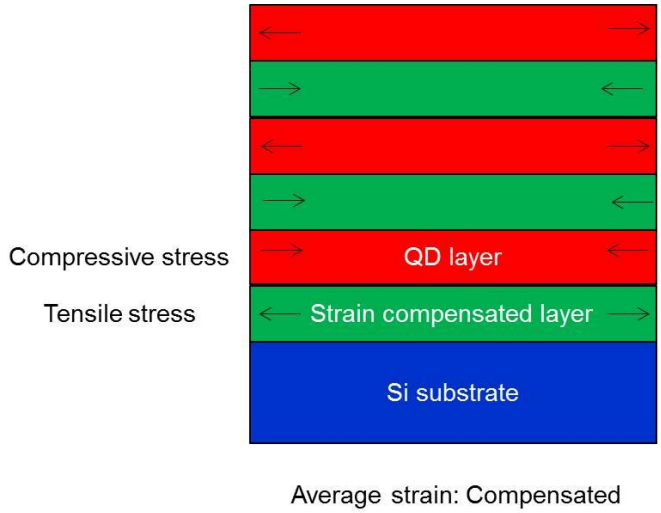

Fig. 5.2: Schematic concept of strain compensation technique.

From these achievements, we concentrated on applying the strain compensation technique to Ge/Si QDs for thinner spacer layer thickness. In case of Ge QDs on Si substrate, a candidate of the spacer layer is carbon (C) incorporated Si, viz. $Si_{1-x}C_x$ layer. The lattice constant of C is 3.567 Å. According to Vegard's law, the lattice constant principally could be changed from 3.567 Å to 5.6575 Å in $Si_{1-x}C_x$ alloy, however substitutional carbon incorporation exceeding few percent is difficult owing to significant small thermal equilibrium solubility of C into Si of the order of 10^{17} atoms/cm^3. So MBE is appropriate to grow $Si_{1-x}C_x$ layer on Si and actually few percent of C is successfully incorporated into

Si because the growth mode of MBE is not governed by thermodynamics but by kinetics [10]. The content is estimated by equaling average strain of QD layer with that of spacer layer,

$$d_{\mathrm{QD}} \cdot \varepsilon_{\mathrm{QD}} = -d_{\mathrm{SL}} \cdot \varepsilon_{SL} \tag{5.2}$$

, where d_{QD} is layer thickness of QD layer, $\varepsilon_{\mathrm{QD}}$ is lattice mismatch of QD layer, d_{SL} is layer thickness of spacer layer, $\varepsilon_{\mathrm{SL}}$ is lattice mismatch of QD layer, respectively. The $\varepsilon_{\mathrm{QD}}$ and $\varepsilon_{\mathrm{SL}}$ are described as follows by using lattice constant of substrate (a_{sub}), QD layer (a_{QD}), and spacer layer (a_{SL}),

$$\varepsilon_{\mathrm{QD}} = \frac{a_{\mathrm{QD}} - a_{\mathrm{sub}}}{a_{\mathrm{sub}}} \tag{5.3}$$

$$\varepsilon_{\mathrm{SL}} = \frac{a_{\mathrm{SL}} - a_{\mathrm{sub}}}{a_{\mathrm{sub}}} \tag{5.4}$$

, for example, C content is 1.73% when d_{QD} and d_{SL} are 5 ML corresponding to 1.3145 nm and 10 nm, respectively.

5.2. Growth of $Si_{1-x}C_x$ layers on Si

For growth of $Si_{1-x}C_x$ layers on Si(001) substrates, effect of C cell temperature, i.e. C flux, was investigated. The $Si_{1-x}C_x$ layer was grown at 500 °C by simultaneous deposition of Si and C. The Si is heated by a electron beam gun. For C source, a C filament cell is used. The deposition rate of Si was 2.8 Å/s. Figure 5.3 and 5.4 shows RHEED images and 20 × 20 μm^2 AFM images for 500 nm-thick $Si_{1-x}C_x$ layers grown on Si(001) substrates at C-cell temperature of (a) 1000 °C, (b) 1100 °C, (c) 1200 °C, (d) 1300 °C, (e) 1400 °C and (f) 1500 °C, respectively. The maximum temperature of C-cell is 1500 °C in our equipment.

Almost identical RHEED patterns of 2×1 reconstructed Si(001) surface were obtained for samples (a)-(e) as shown in Fig. 5.3, while it became obscure for sample (f) in Fig. 5.3. The RHEED pattern for sample (f) suggests formation of micro-roughness on the surface or degradation of crystal quality. From AFM images, islands growth was not observed for all samples. The root mean square (RMS) of the surface roughness was 5.11, 4.21, 3.32, 2.90, 5.17 and 4.44 Å for (a), (b), (c), (d), (e) and (f), respectively. The relationship of the RMS with C-cell temperature is shown in Fig. 5.5. The RMS seems to be no relationship with C-cell temperature. Thus, observed obscure RHEED in (f) probably arises from deterioration of crystal quality.

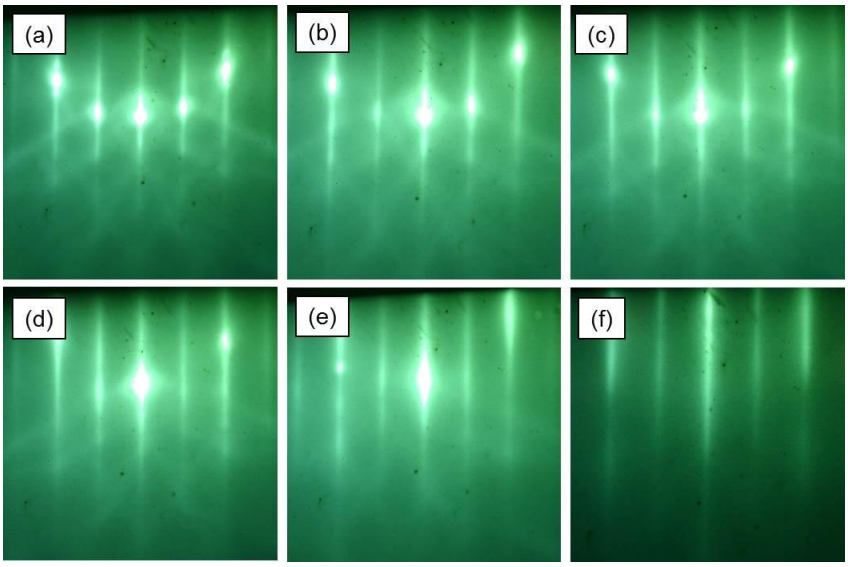

Fig. 5.3: RHEED images for $Si_{1-x}C_x$ layer grown on Si(001) substrates at C-cell temperature of (a) 1000 °C, (b) 1100 °C, (c) 1200 °C, (d) 1300 °C, (e) 1400 °C and (f) 1500 °C.

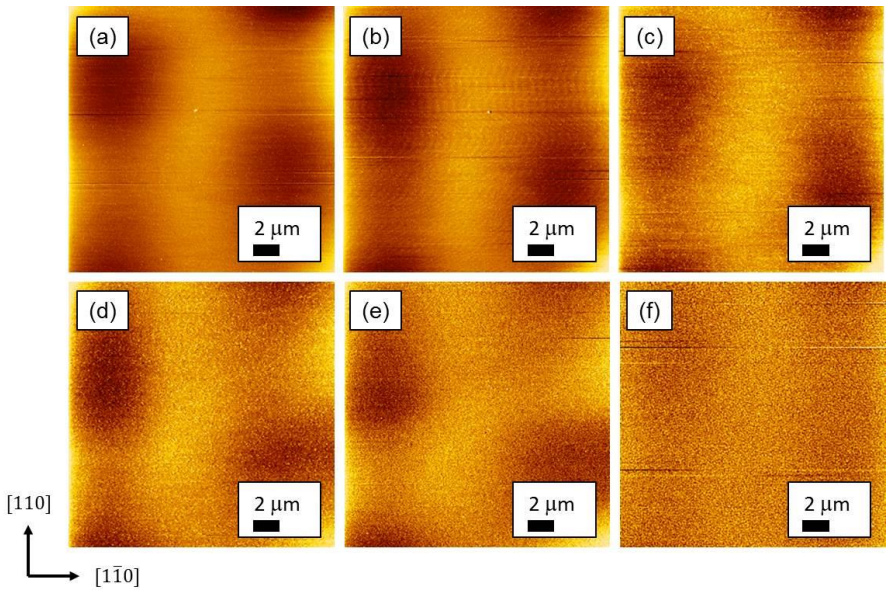

Fig. 5.4: 20 × 20 μm^2 AFM images for $Si_{1-x}C_x$ layer grown on Si(001) substrates at C-cell temperature of (a) 1000 °C, (b) 1100 °C, (c) 1200 °C, (d) 1300 °C, (e) 1400 °C and (f) 1500 °C.

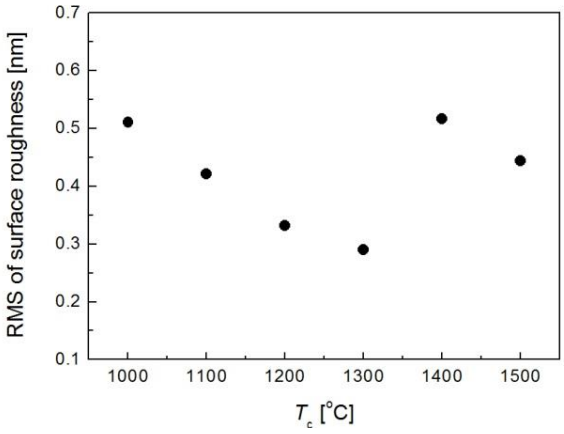

Fig. 5.5: RMS of surface roughness for $Si_{1-x}C_x$ layer grown on Si(001) substrates at C-cell temperature (T_c) of (a) 1000 °C, (b) 1100 °C, (c) 1200 °C, (d) 1300 °C, (e) 1400 °C and (f) 1500 °C.

Figure 5.6 shows ω-2θ scans for $Si_{1-x}C_x$ layers grown on Si(001) substrates at C-cell temperature of (a) 1000 °C, (b) 1100 °C, (c) 1200 °C, (d) 1300 °C, (e) 1400 °C and (f) 1500 °C. The X-ray peak appeared in higher angle region after temperature exceeded 1300 °C. In ω-2θ scan around (004), X-ray peak arise from (004) reflection of epitaxial layers and substrates. If C is substitutionally incorporated into Si, the $Si_{1-x}C_x$ epitaxial layer is deformed and the out-plane lattice constant shrink due to tensile strain induced by lattice mismatch between $Si_{1-x}C_x$ layer and Si substrate. The smaller lattice constant results in appearance of X-ray (004) reflection in higher angle. Therefore, the appeared X-ray peaks were related to the $Si_{1-x}C_x$ layers. The estimated C content in the $Si_{1-x}C_x$ layers (x) were depicted in Fig. 5.7. The x was roughly 0.0004-0.0005 from 1300 to1500 °C. This indicates that C incorporated into Si but C content is not dependent on C-cell temperature in range of 1300-1500 °C. The increased C-cell temperature leads to increase in C flux. If carbon substitutionally incorporates into Si, C content in $Si_{1-x}C_x$ increases with increasing C-cell temperature. The C content was independent of the C-cell temperature. Additionally, dim RHEED pattern was observed for sample grown at C-cell temperature of 1500 °C. These results suggest that C atoms interstitially incorporated into Si and therefore C

content was not changed. Hence, C-cell temperature of 1400 °C is better for growth of $Si_{1-x}C_x$ layers on Si(001) substrates, since the $Si_{1-x}C_x$ related X-ray peak were observed in Fig. 5.6 without darker RHEED pattern.

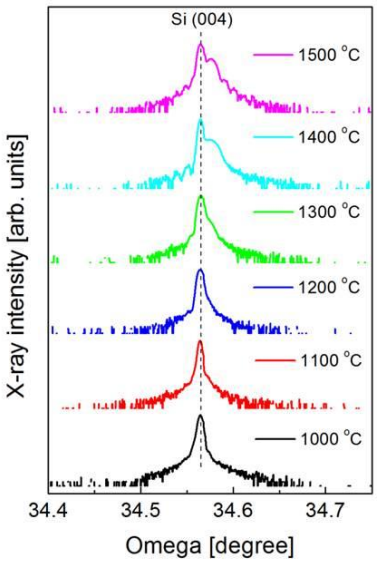

Fig. 5.6: ω-2θ scan for $Si_{1-x}C_x$ layers grown on Si(001) substrates at C-cell temperature (T_c) of (a) 1000 °C, (b) 1100 °C, (c) 1200 °C, (d) 1300 °C, (e) 1400 °C and (f) 1500 °C.

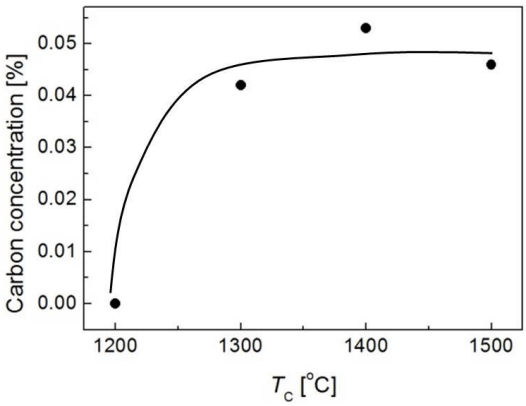

Fig. 5.7: C concentration of $Si_{1-x}C_x$ layers grown on Si(001) substrates at C-cell temperature (T_c). Solid line is visual guide.

For strain compensation of compressive stress induced by QDs, few percent of C content is necessary. To increase C content in $Si_{1-x}C_x$ layer, ratio of Si to C was modified by changing deposition rate from 1.0 Å/s and 2.8 Å/s. Figure 5.8 shows (a) The ω-2θ scans for $Si_{1-x}C_x$ layers grown on Si(001) substrates at C-cell temperature of 1400 °C and (b) C concentration plotted as a function of deposition rate. The ω-2θ scans were almost identical peak. The content of carbon was around 0.0005 and it was hardly changed by deposition rate, possibly due to very low thermal equilibrium solubility of about 10^{17} /cm^3.

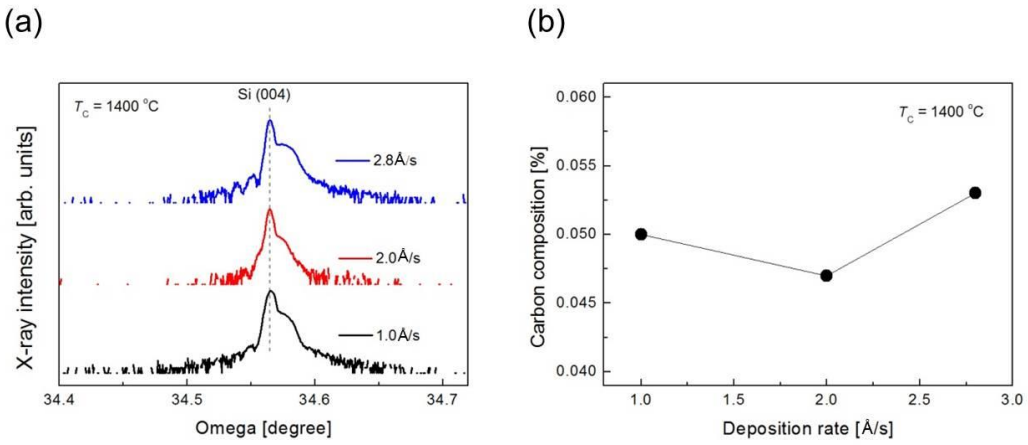

Fig. 5.8: (a) ω-2θ scans for $Si_{1-x}C_x$ layers grown on Si(001) substrates at C-cell temperature of 1400 °C and (b) its C concentration.

5.3. Growth of single layer Ge QDs on $Si_{0.9995}C_{0.0005}$ layer

At the beginning, we grew Ge QDs on $Si_{0.9995}C_{0.0005}$ by using growth temperature at 500 °C and high deposition rate of 2.8 Å/s, since dense and uniform Ge QDs on Si were obtained at 500 °C by using high deposition rate of 2.8 Å/s. Figure 5.9 shows AFM images of topmost surface for single layer $Ge/Si_{0.9995}C_{0.0005}$ QDs on Si(001) substrates at 500 °C and rate of (a) 2.8 Å/s and (b) 2.6 Å/s. The mean height, mean lateral size, dispersion in lateral size and areal density were 2.5 nm, 33.9 nm, 14.1% and 1.1×10^{11} cm^{-2} for (a), and 1.5 nm, 27.5 nm, 9.7% and 1.2×10^{11} cm^{-2} for (b), respectively. Larger dome-shaped QDs were observed in (a), which means bimodal size distribution was realized for (a). The dome-shaped Ge QDs on $Si_{0.9995}C_{0.0005}$ was generated owing to advanced nucleation process induced by suppression of migration by C atoms. C atoms repel Ge adatoms and thus migration of Ge adatoms are suppressed [11-13] because bonding between Ge and C is not energetically favored [14], which leads to advanced nucleation process in comparison with pure Si surface. As previously shown in section 4.1, larger size dome-shaped QDs can be origin of dislocation in multi-stacked QD structure so we decreased growth rate from 2.8 Å/s to 2.6 Å/s to prevent generations of larger QDs. Accordingly, $Ge/Si_{0.9995}C_{0.0005}$ QDs were obtained without larger dome-shaped QDs in (b). So, deposition rate of 2.6 Å/s is appropriate to fabricate multi-stacked $Ge/Si_{0.9995}C_{0.0005}$ QDs.

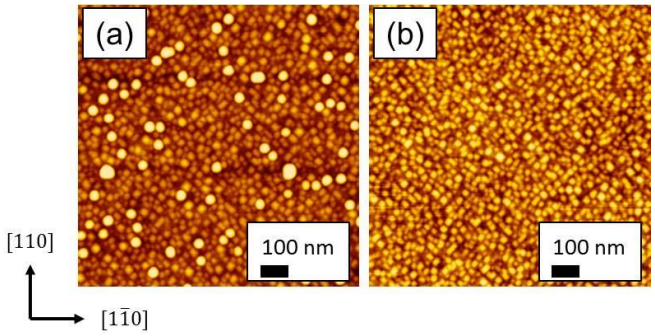

Fig. 5.9: 1×1 μm^2 AFM images of topmost surface for $Ge/Si_{0.9995}C_{0.0005}$ QDs on Si(001) substrates at 500 °C and rate of (a) 2.8 Å/s and (b) 2.6 Å/s.

Next, we fixed deposition rate of 2.6 Å/s and changed layer thickness of Ge to confirm appropriate layer thickness for growth of Ge QDs on $Si_{0.9995}C_{0.0005}$ layers. Figure 5.10 shows AFM images of $Ge/Si_{0.9995}C_{0.0005}$ QDs with layer thickness of (a) 2.8 ML, (b) 3.7 ML, (c) 4.6 ML and (d) 5.5 ML. No Ge QDs were observed in (a). Smaller Ge QDs were generated in (b) and it became denser in (c). Lager dome-shaped Ge QDs were observed in (d). The average height, average lateral size, fluctuation in lateral size and areal density were 1.4 nm, 25.6 nm, 13.4% and 1.54×10^{10} cm^{-2} for (b), 1.8 nm, 26.9 nm, 11.4% and 1.38×10^{10} cm^{-2} for (c), and 2.0 nm, 28.5 nm 14.5% and 1.45×10^{10} cm^{-2} for (d), respectively. The relation between these structural parameters and layer thickness are depicted in Fig. 5.11. The Height and lateral size increased with increasing Ge layer thickness. Both small size dispersion and high density were obtained at 4.6 ML-thick Ge layer.

From optimization of growth condition of Ge QDs on $Si_{0.9995}C_{0.0005}$ layers, dense and better uniformity were obtained by employing growth temperature of 500 °C, deposition rate of 2.6 Å/s and layer thickness of 4.6 ML. Compared with Ge QDs on Si, slightly low deposition rate and few layer thickness was preferred for growth of Ge QDs on $Si_{0.9995}C_{0.0005}$ owing to advanced nucleation process induced by repulsion of Ge atoms by C atoms.

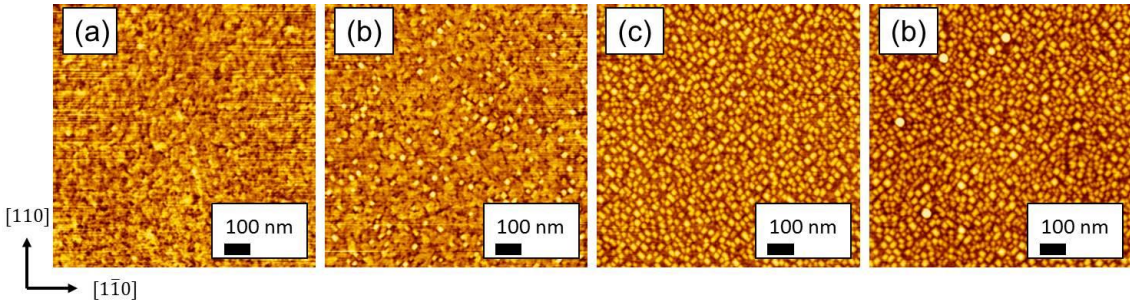

Fig. 5.10: 1 × 1 μm^2 AFM images of topmost surface for $Ge/Si_{0.9995}C_{0.0005}$ QDs on Si(001) substrates grown at 500 °C and deposition rate of 2.6 Å/s with layer thickness of (a) 2.8 ML, (b) 3.7 ML, (c) 4.6 ML and (d) 5.5 ML.

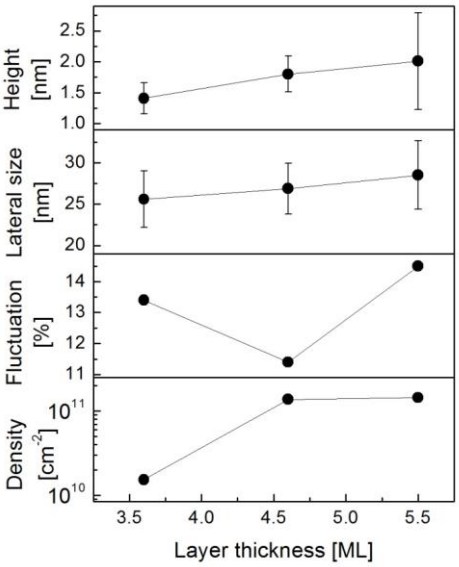

Fig. 5.11: Structural parameters of $Ge/Si_{0.9995}C_{0.0005}$ QDs as a function of Ge layer thickness.

5.4. Fabrication of multi-stacked $Ge/Si_{0.9995}C_{0.0005}$ QDs on Si

Figure 5.12 (a) and (b) shows AFM images of topmost surface for 5-layer and 10-layer-stacked $Ge/Si_{0.9995}C_{0.0005}$ QDs with spacer layer thickness of 40 nm, respectively. Their average height, average lateral size, fluctuation in lateral size and areal density are plotted as a function of number of stacks in Fig. 5.13 (open circle). With increasing number of stacks, the height, lateral size and fluctuation in lateral size increased whereas the areal density decreased. This is due to interface roughness shown in Fig 5.14 (a) BF-STEM images and (b) HAADF-STEM images for 10-layer-stacked $Ge/Si_{0.9995}C_{0.0005}$ QDs. An unexpected undulation at the heterointerface between the Ge QDs and the underlying spacer layer was observed for (a) and (b). To overcome the non-uniform size and decreasing density, $Si_{0.9995}C_{0.0005}$ spacer layer was sandwiched by 2 nm-thick Si interlayers (ILs). The schematic structure of multi-stacked $Ge/Si_{0.9995}C_{0.0005}$ QDs with Si ILs is illustrated in Fig. 5.15. Composite structures of 36 nm-thick $Si_{0.9995}C_{0.0005}$ layers sandwiched by 2 nm-thick Si were used for spacer layers. Closed circle in Fig. 5.13 shows structural parameters of multi-stacked $Ge/Si_{0.9995}C_{0.0005}$ QDs with Si ILs. In contrast to those of $Ge/Si_{0.9995}C_{0.0005}$ QDs without Si ILs, the height, lateral size and areal density were successfully maintained up to 20-layer-stacks. The size uniformity was improved to around 12% by introducing Si ILs owing to smoother heterointerface between the Ge QDs and the underlying spacer layer in Fig 5.14 (c) and (d).

Furthermore, PL measurements were performed at 13 K for 10-layer-stacked (a) 5.0 ML-thick Ge/Si QDs, (b) 4.6 ML-thick $Ge/Si_{0.9995}C_{0.0005}$ QDs without 2 nm-thick Si ILs, and (c) 4.6 ML-thick $Ge/Si_{0.9995}C_{0.0005}$ QDs with 2 nm-thick Si ILs. The PL spectra are shown in Fig 5.16. Si related PL emission peak of 1.08 eV for Ge/Si QDs were shifted towards lower energy region for $Ge/Si_{0.9995}C_{0.0005}$ QDs due to bandgap energy reduction arisen from C incorporation into Si [15-17]. The reduction of band gap is caused by the local strain around the substitutional C atoms and it appears in a low concentration of carbon in $Si_{1-x}C_x$ alloy, which means the bowing of bandgap energy [18]. The broad

PL emission from 0.90 to 1.0 eV would come from no-phonon transition and TO phonon replica of Ge wetting layers [19,20]. PL intensity and linewidth of Ge/$Si_{0.9995}C_{0.0005}$ QDs with Si interlayers became stronger and narrower than that of Ge/$Si_{0.9995}C_{0.0005}$ QDs without Si ILs, respectively. The intensity and linewidth was not comparable with that of Ge/Si QDs. This means crystal quality of $Si_{0.9995}C_{0.0005}$ layers was not as well as that of Si layer. The PL peak energy and PL line width were 0.818 eV and 85.2 meV for (a), 0.845 V and 198.2 meV for (b) and 0.828 V and 96.7 meV for (c), respectively. The PL peak energy for (c) was shifted toward the blue region of approximately 10 meV compared with that for (a). This was caused by an increase in the local strain fields around the QDs, due to the tensile strains caused by the $Si_{0.9995}C_{0.0005}$ spacer layers and/or by the strong confinement effects occurring as a result of the formation of smaller Ge QDs on the combined set of $Si_{0.9995}C_{0.0005}$ spacer layers and Si ILs compared with the Ge QDs formed on the plain Si spacer layers. Therefore, the Si ILs helps to improve both the uniformity of QD and the heterointerfaces formed at the surface of the Ge QDs, and thus it improved the optical properties.

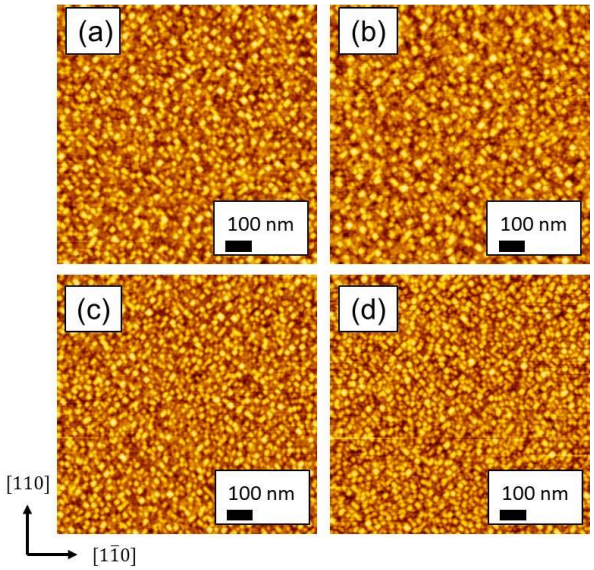

Fig. 5.12: 1 × 1 μm^2 AFM images of topmost surface for (a) 5-layer and (b) 10-layer-stacked Ge/$Si_{0.9995}C_{0.0005}$ QDs and for (a) 5-layer and (b) 10-layer-stacked Ge/$Si_{0.9995}C_{0.0005}$ QDs with 2 nm-thick Si interlayers, respectively.

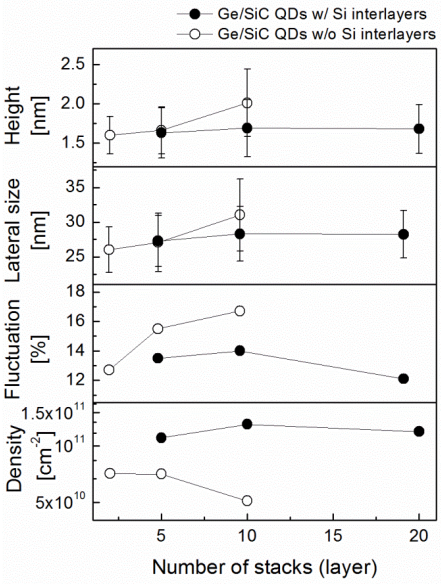

Fig. 5.13: Structural parameters as a function of number of stacks for Ge/$Si_{0.9995}C_{0.0005}$ QDs (open circle) and Ge/$Si_{0.9995}C_{0.0005}$ QDs with 2 nm-thick Si interlayers (closed circle).

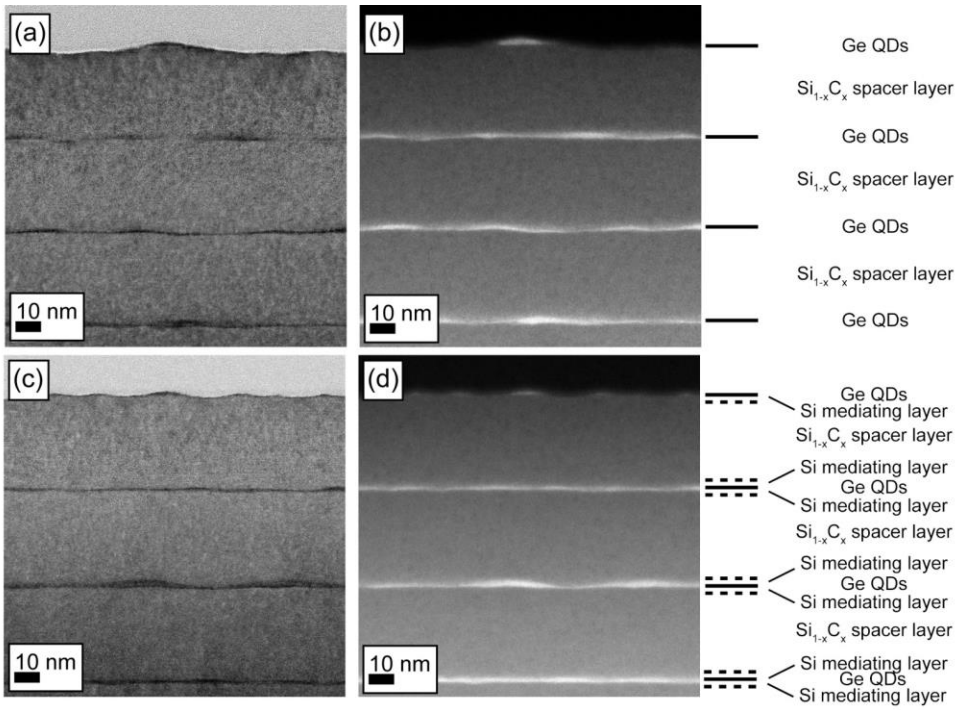

Fig. 5.14: BF and HAADF-STEM images of top portion of 10-layer-stacked Ge/$Si_{0.9995}C_{0.0005}$ QDs without Si interlayers (a,b) and with 2 nm-thick Si interlayers (c,d), respectively.

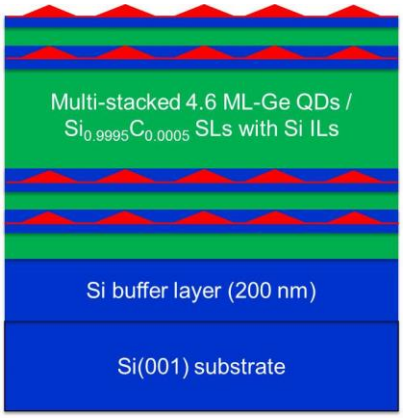

Fig. 5.15: Schematic structure of multi-stacked Ge/ $Si_{0.9995}C_{0.0005}$ QDs with Si interlayers.

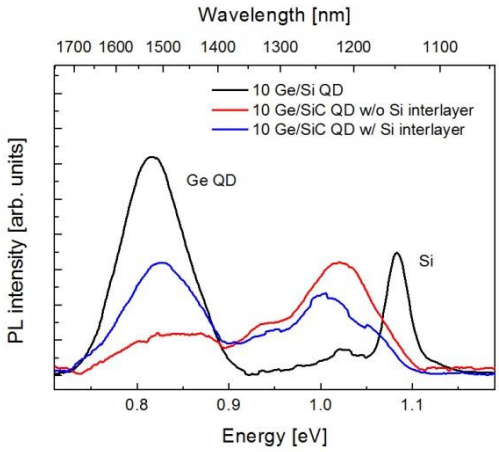

Fig. 5.16: PL spectra for 10-layer-stacked (a) Ge/Si QDs, (b) $Ge/Si_{0.9995}C_{0.0005}$ QDs without 2 nm-thick Si interlayers, and (c) $Ge/Si_{0.9995}C_{0.0005}$ QDs with 2 nm-thick Si interlayers.

5.5. Dependence on spacer layer thickness

For electrically coupled QDs, short inter-dot spacing less than 4 nm is required so the spacer layer thickness was reduced and effect of spacer layer thickness was studied. Figure 5.17 shows 5 × 5 μm^2 and 1 × 1 μm^2 AFM images of topmost surface for 20-layer-stacked Ge/$Si_{0.9995}C_{0.0005}$ QDs with 2 nm-thick Si ILs and $Si_{0.9995}C_{0.0005}$ spacer layer thickness (d_{SL}) of (a) and (e) 2, (b) and (f) 6, (c) and (g) 16, and (d) and (h) 36 nm, respectively. The generation of larger coalesced Ge QDs was suppressed even in d_{SL} = 6 nm in contrast to Ge/Si QDs in section 4.3. Figure 5.18 shows the dependence of structural parameters for (a) 20-layer-stacked Ge/$Si_{0.9995}C_{0.0005}$ QDs with 2 nm-thick Si ILs (open circle) on spacer layer thickness and (b) that for 20-layer-stacked Ge/Si QDs is added in Fig. 5.18 (closed circle). The QD size increased for both samples. The fluctuation in lateral size for (a) tended to decrease with decrease in spacer layer thickness, while that for (b) monotonically increased with decreasing the spacer layer thickness. Decrease in the areal density, accompanied by increase in QD size, was observed from d_{SL} = 10 nm to 6 nm for both the structures, though the decreasing rate of the areal density for (a) was much smaller than that for (b). In general, the second sheet of QDs grows in the strain field created by the buried first sheet of QDs in a multi-stacked configuration. This type of vertical correlation is observed in various material systems, including Ge/Si [1,21,22]. In the Ge/$Si_{0.9995}C_{0.0005}$ QD system, the tensile-strained $Si_{0.9995}C_{0.0005}$ spacer layers seem to compensate a certain fraction of strain field induced by the Ge QDs, though 1.7% of C content in strain compensating $Si_{1-x}C_x$ layers would be still necessary to completely compensate the compressive strain for d_{SL} = 10 nm. Furthermore, the strain fields become stronger with increase in QD size. So the author thinks that the suppression of appearance of aggregated Ge QDs achieved by both compensation of certain fraction of strain field and weaker strain fields induced by smaller QDs.

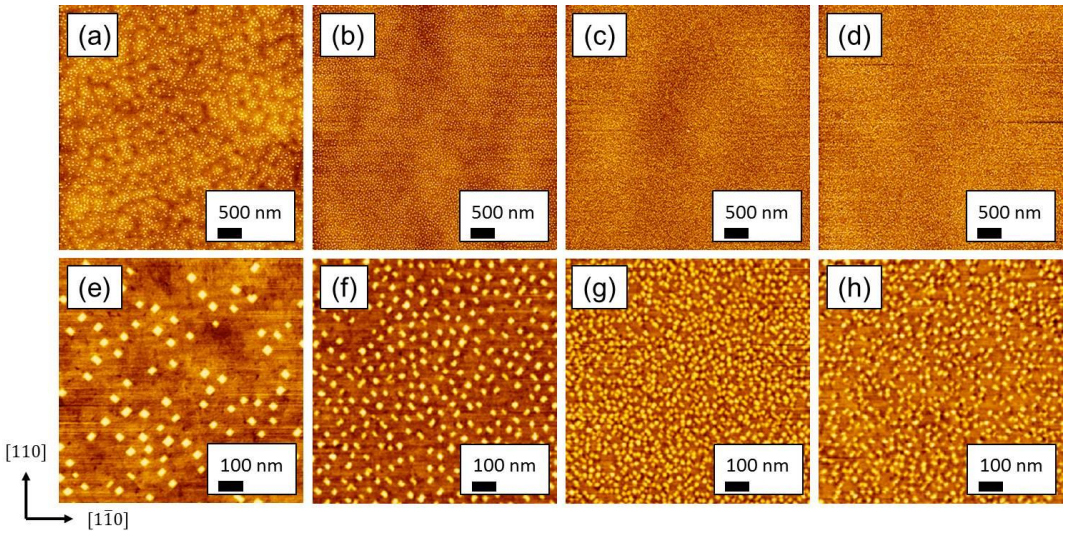

Fig. 5.17: 5 × 5 μm^2 and 1 × 1 μm^2 AFM images of topmost surface for 20-layer-stacked Ge/$Si_{0.9995}C_{0.0005}$ QDs with 2 nm-thick Si interlayers and $Si_{0.9995}C_{0.0005}$ spacer layer thickness of (a) 2, (b) 6, (c) 16 and (d) 36 nm, respectively.

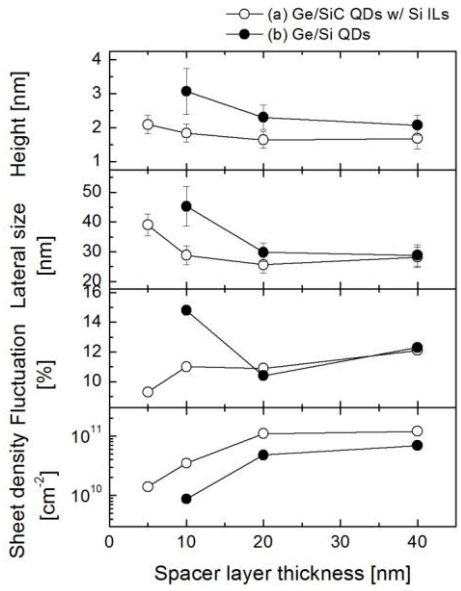

Fig. 5.18: Dependence of structural parameters on spacer layer thickness for (a) 20-layer-stacked Ge/$Si_{0.9995}C_{0.0005}$ QDs with 2 nm-thick Si interlayer (open circle) in addition to (b) that for 20-layer-stacked Ge/Si QDs (closed circle).

Figure 5.19 shows PL spectra for 20-layer-stacked Ge/$Si_{0.9995}C_{0.0005}$ QDs with d_{SL} including Si ILs = (a) 40 nm, (b) 20 nm, (c) 10 nm and (d) 6 nm. The $Si_{0.9995}C_{0.0005}$ related PL emission peak were observed around 1.05-1.06 eV for (a), (b) and (c), and it shifted to 1.1 eV for (d) probably due to relatively few amount of $Si_{0.9995}C_{0.0005}$ layers. The PL emission peak from 0.9 eV to 1.0 eV probably arose from no-phonon transition and TO phonon replica of Ge wetting layers. The PL emission peak of about 0.8 eV related to Ge QDs and it was observed even in d_{SL} = 6 nm. The PL peak energy and PL linewidth were 0.839 eV and 81.0 meV for (a), 0.823 V and 81.5 meV for (b), 0.806 V and 105.7 meV and (d) 0.797 V and 148.6 meV, respectively. The PL parameters are summarized in Fig. 5.20. The PL peak energy decreased with decrease in d_{SL}, while the PL linewidth increased. The redshifted PL peak energy is due to quantum size effect [20] or electric coupling between Ge QDs [23-25]. The incremental difference of peak shift was about 40 meV from d_{SL} = 6 to 40 nm. The change of quantized energy level should be roughly 20 meV by regarding the self-assembled QDs as quantum well [26], which is not consistent with experimental results. The broaden PL emissions with decreasing d_{SL} were inconsistent with fluctuation in lateral size as show in Fig. 4.40. Furthermore, PL intensity increased at spacer layer thickness of 6 nm possibly due to enhanced spatially direct transition accrued from electrically coupled QDs. These results suggests electric coupling between Ge QDs, i.e. creation of minibands, since inter-dot spacing is 4 nm in growth direction for samples with the spacer layer thickness of 6 nm, which is enough thin to occur the electric coupling as previously mentioned in section 1.4.

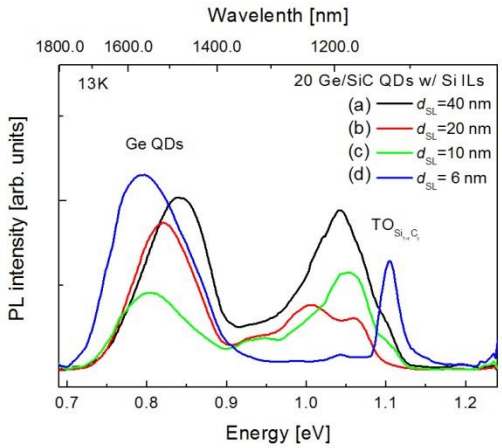

Fig. 5.19: PL spectra for 20-layer-stacked $Ge/Si_{0.9995}C_{0.0005}$ QDs with d_{SL} including 2 nm-thick Si ILs = (a) 40 nm, (b) 20 nm, (c) 10 nm and (d) 6 nm.

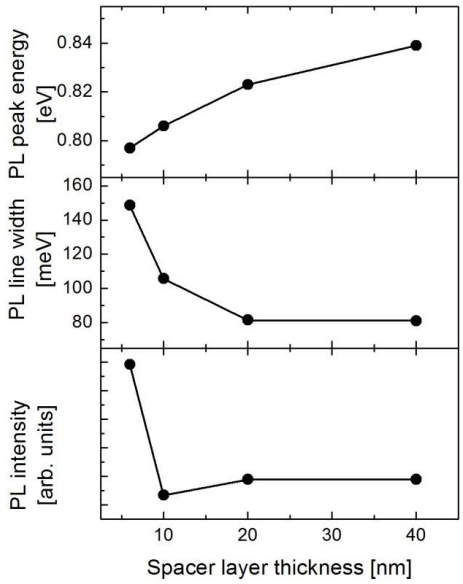

Fig. 5.20: PL peak energy, PL line width and PL intensity of 20-layer-stacked $Ge/Si_{0.9995}C_{0.0005}$ QDs with 2 nm-thick Si interlayers as a function of spacer layer thickness.

Figure 5.21 shows PL peak energy as a function of third root of excitation intensity ($(P_{exc})^{1/3}$) for (a), (b), (c) and (d) in Fig 5.19. The PL peak energy was proportional to $(P_{exc})^{1/3}$ for all samples. This indicates type-II heterointerface was realized even in $Ge/Si_{0.9995}C_{0.0005}$ QDs as explained in section 4.3.

This is the good demonstration of previously suggested type-II band lineup for $Ge/Si_{1-x}C_x$ QDs [18,27,28]. The slope *b* values were for 3.45, 1.38, 2.52, and 5.84 $(meV)^{2/3}$ for d_{SL} = 40, 20, 10 and 6 nm, respectively. Furthermore, the larger slope *b* values were obtained for d_{SL} = 6 nm in comparison with d_{SL} from 10 to 40 nm. Although the QD density decreased for d_{SL} = 6 nm, PL intensity increased in Fig. 5.19. The larger slope seems to be not related to decrease in density. In d_{SL} = 6 nm, inter-dot spacing is less than 4 nm in growth direction. It is possible to start overlapping of wave function in Ge/Si material system as previously mentioned [29-32]. The pronounced buleshift of PL peak energy caused by high excitation power were observed for InGaAs/GaAs QDs employing enough short inter-dot spacing to form minibands [33]. Therefore, the author believe the miniband was established in $Ge/Si_{0.9995}C_{0.0005}$ QDs with d_{SL} = 6 nm.

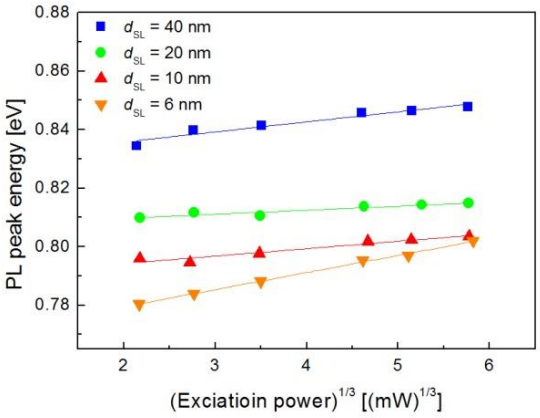

Fig. 5.21: PL peak energy for 20-layer-stacked $Ge/Si_{0.9995}C_{0.0005}$ QDs with d_{SL} including Si ILs = (a) 40 nm, (b) 20 nm, (c) 10 nm and (d) 6 nm as a function of third root of excitation power. The fitted lines are shown as solid line.

5.6. Summary

Structural and optical properties of multi-stacked Ge/$Si_{1-x}C_x$ QDs were studied. Firstly, growth of $Si_{1-x}C_x$ layers on Si substrates was investigated. The $Si_{1-x}C_x$ layer with better crystal quality were grown by C-cell temperature at 1400 °C and C content was 0.0005. The incorporation of C atoms in Si seems to be governed by low thermal equilibrium solubility. Secondly, single layer Ge QDs on $Si_{0.9995}C_{0.0005}$ layers were grown. Appearance of larger dome-shaped QDs was suppressed by reducing deposition rate from 2.8 Å/s to 2.6 Å/s. The nucleation process of Ge QDs on $Si_{0.9995}C_{0.0005}$ was influenced by C atoms since C atoms repel Ge due to not energetically favored C-Ge bonding so slight low deposition rate of 2.6 Å/s was better to obtain uniform Ge QDs on $Si_{0.9995}C_{0.0005}$ layers. Thirdly, the Ge/$Si_{0.9995}C_{0.0005}$ QD layers were stacked. The multi-stacked Ge/$Si_{0.9995}C_{0.0005}$ QDs were grown well by introducing 2 nm-thick Si interlayers between $Si_{0.9995}C_{0.0005}$ layers owing to prevention of rough heterointerface between Ge QDs and $Si_{0.9995}C_{0.0005}$ layers. It is thought that the Si interlayers terminate C atoms on $Si_{0.9995}C_{0.0005}$ and suppress the Ge-C bonding. Finally, effect of spacer layer thickness was investigated. In comparison with multi-stacked Ge/Si QDs, generation of aggregated Ge islands were not observed for multi-stacked Ge/$Si_{0.9995}C_{0.0005}$ QDs even for spacer layer thickness of 6 nm due to slightly compensated strain induced by Ge QDs and weaker strain fields established by smaller Ge QDs. PL emission peak from Ge QDs were observed from spacer layer thickness from 6 to 40 nm and it showed characteristics of type-II band lineup. By decreasing spacer layer thickness from 40 to 6 nm, PL peak energy redshifted from 0.839 to 0.797 V, viz. the incremental difference of peak shift was about 40 meV, owing to quantum size effect and/or electric coupled QDs. The change of quantized energy level should be 20 meV by regarding the self-assembled QDs as quantum well, which is not consistent with the experimental results of 40 meV. Furthermore, PL intensity increased at spacer layer thickness of 6 nm possibly due to enhanced spatially direct transition accrued from electrically coupled QDs. The author believes that these results suggests electric coupling between QDs.

References

[1] J. Tersoff, C. Teichert, and M. G. Lagally: Phys. Rev. Lett. **76** (1996) 1675-1678.

[2] D. Alonso-Álvarez, J. M. Ripalda, B. Alén, J. M. Llorens, A. Rivera and F. Briones: Adv. Mater. **23** (2011) 5256-5261.

[3] N. J. Ekins-Daukes, K. Kawaguchi, and J. Zhang: Cryst. Growth and Design **2** (2002) 287-292.

[4] K. Akahane, N. Yamamoto, and T. Kawanishi: Phys. Status. Solidi. A **208** (2011) 425-428.

[5] R. Oshima, T. Hashimoto, H. Shigekawa, Y. Okada: J. Appl. Phys. **100**, 083110 (2006).

[6] R. Oshima, T. Hashimoto, H. Shigekawa, Y. Okada: Physica E. **32** (2006) 77-80.

[7] R. Oshima, A. Takata, Y. Okada: Appl. Phys. Lett. **93**, 083111 (2008).

[8] S. M. Hubbard, C. D. Cress, C. G. Bailey, R. P. Raffaelle, S. G. Bailey, and D. M. Wilt: Appl. Phys. Lett. **92**, 123512 (2008).

[9] R. B. Laghumavarapu, M. EI-Emawy, N. Nuntawong, A. Moscho, L. F. Lester, and D. L. Huffaker: Appl. Phys. Lett. **91**, 243115 (2007).

[10] Y. Shiraki, N. Usami: "*Silicon-germanium (SiGe) nanostructures*" (Woodhead, 2011) Chapter 5.

[11] O. Leifeld, A. Beyer, E. Müller, K. Kern and D. Grützmacher, and K. Kern: Thin Solid Films **380** (2000) 176-179.

[12] O. Leifeld, A. Beyer, E. Müller, K. Kern and D. Grützmacher: Mater. Res. Eng. **B74** (2000) 222.

[13] O. G. Schmidt, S. Schieker, K. Eberl, O. Kienzle, and E. Ernst: Appl. Phys. Lett. **73** (1998) 659.

[14] R. Matsutani, K. Sueoka, and E. Kamiyama: Phys. Status. Solidi. (2004) 1-4.

[15] H. J. Osten *et al*., Thin Solid Films **367**, 101 (2000) 101.

[16] K. Brunner, K. Eberl and W. Winter, Phys. Rev. Lett. **76** (1996) 303.

[17] K. Eberl, O. G. Schmidt, S. Schieker, N. Y. Jin-Phillipp, and F. Phillipp: Phys. Rev. Lett. **76** (1998) 1593-1597.

[18] S. T. Chang, C. Y. Lin, and C. W. Liu: J. Appl. Phys. **92** (2002) 3717.

[19] G. Abstreiter, P. Schittenhelm, C. Engel, E. Silveria, A. Zrenner, D. Meettens, and W. Jäger: Semicond. Sci. Technol. **11** (1996) 1521-1528.

[20] H. Sunamura, N. Usami, Y. Shiraki, and S. Fukatsu, Appl. Phys. Lett. **66**, 3024 (1995).

[21] V. L. Thanh, V. Yam, P. Boucaud, F. Fortuna, C. Ulysse, D. Bouchier, L. Vervoort, and J. M. Lourtioz: Phys. Rev. B **60**, 5851 (1999).

[22] O. G. Schmidt and K. Eberl: Phys. Rev. B **61**, 13721 (2000).

[23] Y. Shoji, K. Narahara, H. Tanaka, T. Kita, K. Akimoto, and Y. Okada, J. Appl. Phys. **111**, 074305 (2012).

[24] M. K. Zundel, P. Specht, K. Eberl, N. Y. Jin-Philipp, and F. Philipp, Appl. Phys. Lett. **71**, 2972 (1997).

[25] G. S. Solomon, J. A. Terezza, A. F. Marshall, and J. S. Harris, Jr., Phys. Rev. Lett. **76**, 952 (1996).

[26] K. Brunner: Rep. Prog. Phys. **65** (2002) 27-72.

[27] O. G. Schmidt and K. Eberl: Appl. Phys. Lett. **73**, (1998) 2790-2792.

[28] O. G. Schmidt, L. Lange, K. Eberl, O. Kienzle, and F. Ernst: Thin Solid Films **321** (1998) 70-75.

[29] A. I. Yakimov, A. A. Bloshkin and A. V. Dvurechenskii, Semicond. Sci. Technol. **24**, 095002 (2009).

[30] W. Hu, M. M. Rahman, M. Lee, Y. Li, and S. Samukawa: J. Appl. Phys. **114**, 124509 (2013).

[31] V. G. Talalaev, G. E. Cirlin, A. A. Tonkikh, N. D. Zakharov, P. Werner, U. Gösele, J. W.Tomm, and T. Elsaesser: Nanoscale Res. Lett. **1**, 137 (2006).

[32] O. L. Lazarenkova and A. A. Balandin: J. Appl. Phys. **89**, 5509 (2001).

[33] T. Sugaya, T. Amano, M. Mori, and S. Niki: Appl. Phys. Lett. **97** 043112 (2010).

Chapter 6. Application of Multi-stacked Ge QDs to Solar Cells

In this chapter, multi-stacked Ge/Si QDs and Ge/$Si_{0.9995}C_{0.0005}$ QDs were applied to solar cells. In the beginning, trial fabrication of Ge/Si QD solar cells was carried out. Next, the author examined effect of number of stacks on solar cells properties. Then, effect of infrared irradiation on Ge/Si QD solar cells was investigated. Furthermore, Ge/Si QD solar cells and Ge/$Si_{0.9995}C_{0.0005}$ QD solar cells were compared. Finally, dependence of solar cells properties on spacer layer thickness was studied.

6.1. Fabrication procedures of solar cells

For solar cells structure, the author fabricated Si heterojunction solar cells using hydrogenated amorphous Si (a-Si:H). Generally, the Si heterojunction solar cells are fabricated by low temperature process of around 180 °C in comparison with conventional Si solar cells using the p-n junction formed by thermal diffusion of dopants at around 900 °C, which has advantage of fabrication of Ge/Si QD solar cells. Ge-Si intermixing occurs easily so low temperature process enable to maintain as-grown Ge/Si QD structure. To fabricate solar cells, Si capped multi-stacked Ge QDs were cleaned by chemical solutions. Although the cleaning procedure was almost same with the procedure in Fig. 2.6, after the process-10, samples were dipped into diluted hydrofluoric acid (2% dHF) for 2 min and then they were rinsed in pure water. The samples were loaded into PECVD chamber as soon as possible after the cleaning procedures. Subsequently, intrinsic type a-Si:H was deposited on Si capped multi-stacked QDs at 150 °C and then n-type a-Si:H was deposited at 180 °C. The intrinsic a-Si:H is widely used to reduce surface recombination effectively [1-3]. The flow rate of SiH_4, pressure, RF power were 20 sccm, 7 Pa and 30 W for i-layer, respectively. For n-layer, SiH_4 and PH_3 were simultaneously provided at the rate of 10 and 100 sccm, respectively at the pressure of 10 Pa and RF power of 40 W. Following deposition of indium tin oxide (ITO) on p-n junction formed samples by

magnetron sputtering, silver (Ag) was deposited by vacuum evaporation for front electrode. Finally, aluminum (Al) was deposited by vacuum evaporation for rear electrode.

6.2. Trial of Ge/Si QDSCs fabrication

First, we tried to fabricate 100-layer-stacked Ge/Si QD solar cells and the schematic cell structure is shown in Fig. 6.1. Ga doped 2 μm-thick p-type/1 μm-thick p^+-layer were grown on Si(001) substrate with resistivity of 0.01 Ωcm and then 100-layer-stacked Ge/Si QDs with spacer layer thickness of 30 nm were fabricated by using the pulse growth technique. After cleaning samples by using some chemical solutions as described in section 6.1, 10 nm-thick i-type and 20 nm-thick n-type hydrogenated amorphous Si (a-Si:H) were deposited on samples. Following deposition of 75 nm-thick indium tin oxide (ITO) and ~500 nm-thick silver (Ag) for front electrode, ~500 nm-thick aluminum (Al) was deposited for rear electrode. Figure 6.2 shows current-voltage (*J*-*V*) curves for the (a) 100-layer-stacked QDSCs and (b) 5 μm-thick epitaxially grown Si SCs as a reference. The short circuit current density (J_{sc}), open circuit voltage (V_{oc}), fill factor (FF) and conversion efficiency (η) were 13.93 mA/cm^2, 0.2314 V, 0.3977 and 1.282% for (a), and 15.23 mA/cm^2, 0.4776 V, 0.7315 and 5.321% for (b), respectively. The J_{SC}, V_{OC} and FF decreased and thus efficiency decreased by introducing 100-layer-stacked QDs. In general, increased J_{SC} and decreased V_{OC} and FF are commonly observed in QDSCs using III-V compound semiconductors [4-9]. Figure 6.3 shows external quantum efficiency (EQE) for each sample. Slightly increased EQE response up to 1300 nm was observed due to contribution from Ge QD layers, whereas EQE response from 300 nm to 800 nm decreased probably due to recombination of photo-generate carriers in Ge/Si QD region. The increase in recombination process is thought to result from difficulty of carrier extraction from Ge QDs owing to carrier confinement [10].

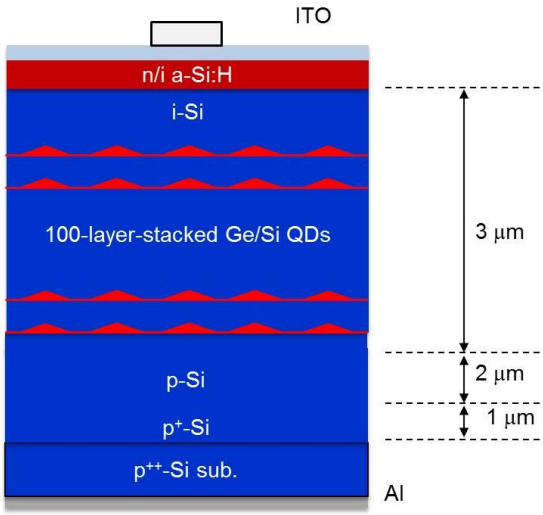

Fig. 6.1: Schematic solar cell structure of 100-layer-stacked Ge/Si QDSCs.

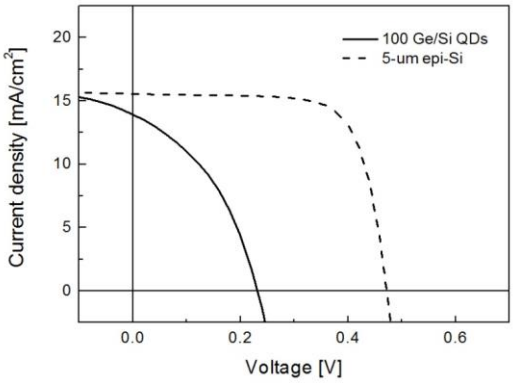

Fig. 6.2: *J-V* curves for 100-layer-stacked Ge/Si QDSCs and epitaxially grown Si SCs (ref.).

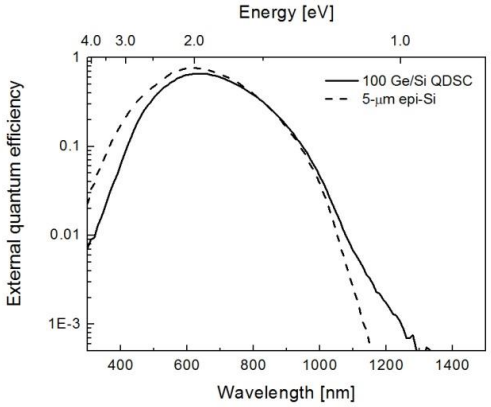

Fig. 6.3: EQE spectra for 100-layer-stacked Ge/Si QDSCs and epitaxially grown Si SCs (ref.).

6.3. Dependence on number of stacks

To investigate effect of Ge/Si QDs on the property of solar cells, number of stacked layer was changed. Figure 6.4 shows the schematic sample structure of multi-stacked Ge/Si QDSCs with Si spacer layer thickness of 30 nm. The number of stacks (x) was changed from 25 to 100 layers. Total layer thickness of multi-stacked Ge/Si QDs was fixed to 3.4 μm to obtain identical built-in potential. The multi-stacked QDs were inserted in middle part of 3.4 μm-thick Si layers. Figure 6.5 (a) shows J-V curves for the multi-stacked Ge/Si QDSCs and the solar cell parameters are summarized in Fig. 6.5 (b). The J_{SC} and FF decreased with increasing number of stacks, and hence η decreased. The V_{OC} reduced from 0.48 to 0.37 V by introduction of Ge QDs and it was not strongly affected by number of stacks, which suggests that quasi-Fermi energy between CB of Si and VB of Ge QDs determined the V_{OC} in Ge/Si QDSCs. Figure 6.6 shows EQE spectra for the QDSCs. EQE decreased with increase in number of stacks due to recombination of photo-generated carriers in Si, which is responsible for the decreased J_{SC} in Fig 6.5 (a).

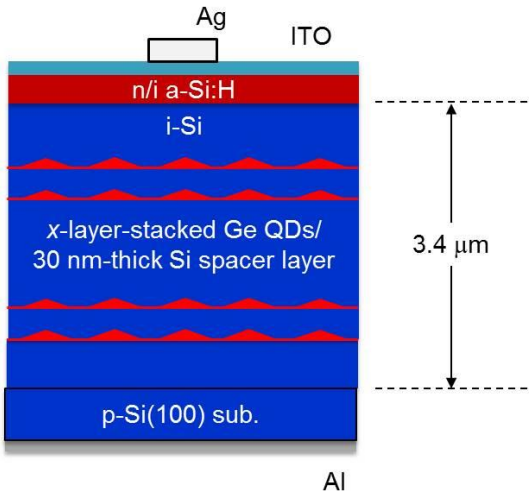

Fig. 6.4: Schematic structure of multi-stacked Ge/Si QDSCs. The resistivity of p-Si substrate is 2 Ωcm. The number of stacks is 25, 50, 75 and 100 layers. Total layer thickness of intrinsic layer including multi-stacked Ge/Si QDs was fixed to 3.4 μm to obtain identical built-in potential.

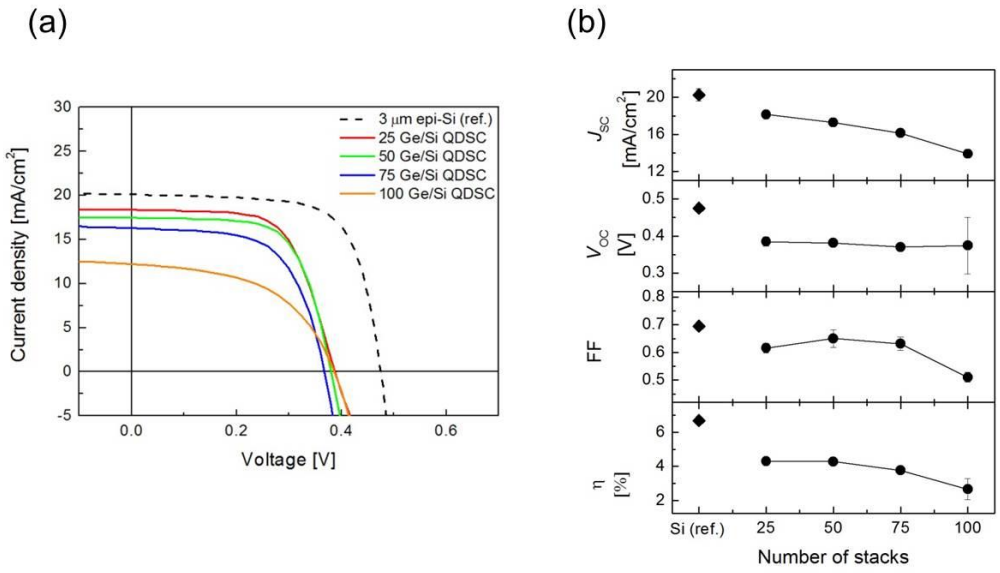

Fig. 6.5: (a) *J*-*V* curves for multi-stacked Ge/Si QDSCs and epitaxially grown 3.4 μm-thick Si solar cells as a reference. (b) Dependence of solar cell parameters of the QDSCs on number of stacks.

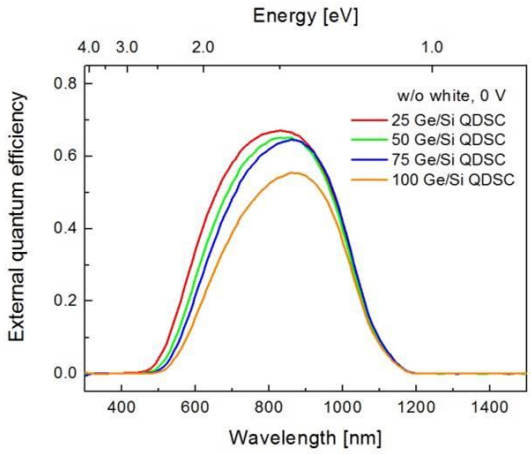

Fig. 6.6: EQE spectra for multi-stacked Ge/Si QDSCs measured at bias voltage of 0 V without bias light.

To make sure the recombination process, PL measurements were performed. PL spectra for the multi-stacked Ge/Si QDSCs are given in Fig. 6.7 (a) at 12 K and (b) at room temperature (RT). Unexpected shoulder peak from 0.9-1.0 eV were observed in (b). Origin of the shoulder peak is

ambiguity since PL emission peaks appear and become stronger at lower temperature generally owing to prevention of thermal escape of carriers trapped in some energy levels. One of the conceivable reasons of the generation shoulder peak might be phonon related PL emissions. Somehow, PL emission form Ge QDs were still observed even in solar cells and the PL intensity increased with increase in number of stacks for at both 12 K and RT. This suggests that photo-generated carriers could be not properly transported by built-in potential in Ge/Si QDSCs. Next, we investigated transport property of the QDSCs by EQE measurements under different bias voltage. Figure 6.8 shows the J_{SC} of the QDSCs calculated by EQE as a function of bias voltage. In general, extraction of photo-generated carriers to external circuit is enhanced by reverse bias. However, the J_{SC} were not significantly recovered by reverse bias voltage for all samples, which suggests that photo-generate carriers recombine on the way to doped layers.

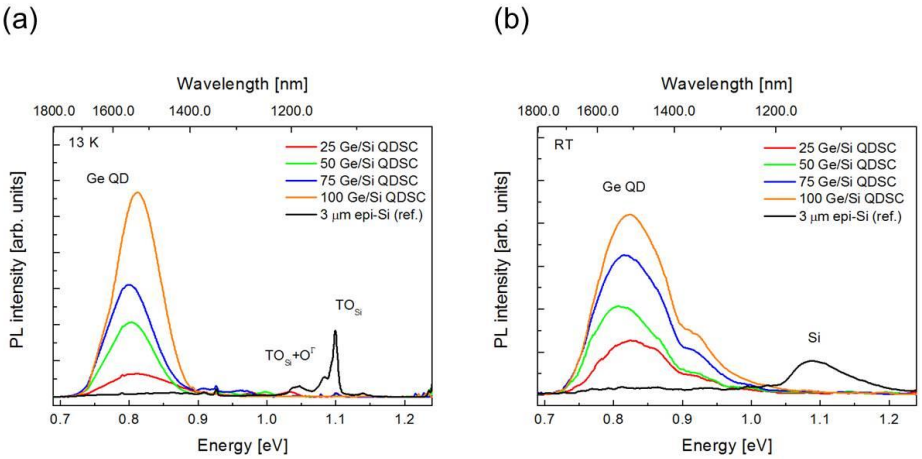

Fig. 6.7: PL spectra for the multi-stacked Ge/Si QDSCs measured at (a) 12 K and (b) room temperature (RT).

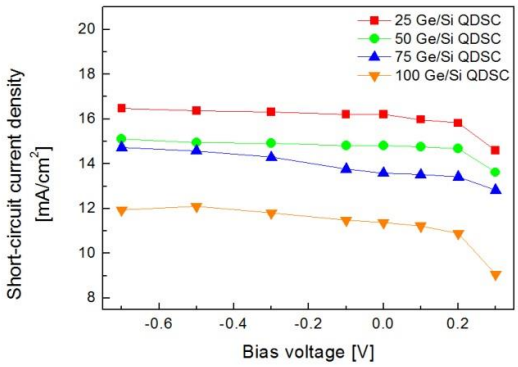

Fig. 6.8: Dependence of J_{SC} calculated by EQE for the multi-stacked QDSCs on bias voltage.

6.4. Effect of infrared irradiation

Next, the author investigated effect of infrared (IR) on QDSCs to enhance escape process of holes from energy levels in Ge QDs as given in Fig. 6.9 (a). Figure 6.9 (b) shows our experimental setup to measure IR effect. In our experiments, solar cells were irradiated on the continuous IR light in addition to chopped monochromatic light. The IR light was created by inserting IR pass filter in from of white bias light and longer wavelength than 980 nm were able to irradiate solar cells. Figure 6.10 shows ΔEQE spectra obtained by subtracting EQE spectra without IR from with IR for 100-layer-stacked QDs and reference Si solar cells. Slightly larger ΔEQE for Ge/Si QDSCs were observed than that for Si reference SCs possibly due to enhancement escape process of holes trapped in Ge QDs. The increased ΔEQE for reference Si SCs came from contribution of Si owing to absorption of IR from 980 to 1110 nm. The increased ΔEQE for shorter wavelength than 980 nm could arise from lack of perfect cut filter for shorter wavelength.

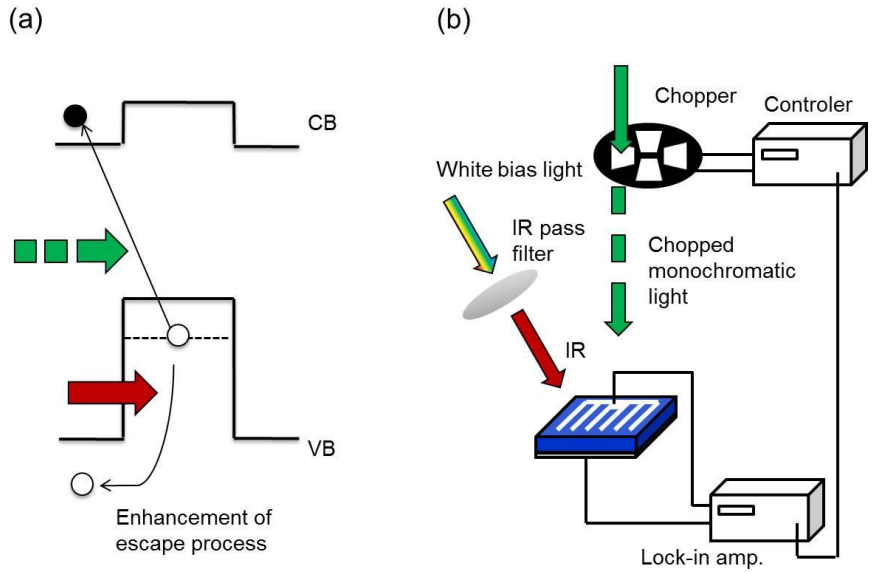

Fig. 6.9: (a) Concept of enhancement of escape process of holes induced by additional IR irradiation and (b) experimental setup for EQE measurements accompanying IR irradiation.

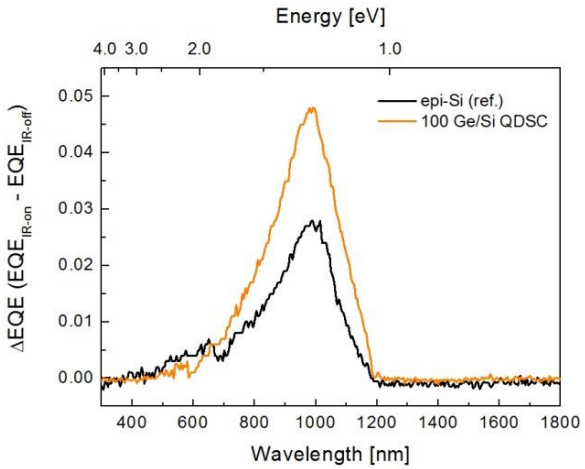

Fig. 6.10: ΔEQE spectra for 100-layer-stacked Ge/Si QDSCs and epi-Si SCs as reference.

6.5. Fabrication of 50-layer-stacked Ge/$Si_{0.9995}C_{0.0005}$ QDs

To investigate effect of strain compensating $Si_{0.9995}C_{0.0005}$ layer on properties of solar cells, we fabricated 50-layer-stacked Ge/$Si_{0.9995}C_{0.0005}$ QDSCs and compared with 50-layer-stacked Ge/Si QDSCs. Figure 6.11 shows sample structure for 50-layer-stacked Ge/$Si_{0.9995}C_{0.0005}$ QDSCs and 50 Ge/Si QDs. The spacer layer thickness was composed of 4 nm-thick Si interlayers (ILs) and 6 nm-thick strain compensating $Si_{0.9995}C_{0.0005}$ layers for Ge/$Si_{0.9995}C_{0.0005}$ QDSCs and of 10 nm-thick Si for 50 Ge/Si QDs. Figure 6.12 shows *J*-*V* curves for (a) 50-layer-stacked Ge/$Si_{0.9995}C_{0.0005}$ QDSCs and (b) 50 Ge/Si QDs. The J_{SC}, V_{OC}, FF and η were 6.23 mA/cm^2, 0.42 V, 0.73 and 1.91% for (a) and 6.20 mA/cm^2, 0.38 V, 0.70 and 1.62% for (b), respectively. The solar cells parameters were slightly improved by introducing $Si_{0.9995}C_{0.0005}$ spacer layers. Figure 6.13 shows EQE spectra for each sample. Subtle increase in EQE was observed for Ge/$Si_{0.9995}C_{0.0005}$ QDSCs, which suggests that collection efficiency of carriers was slightly improved.

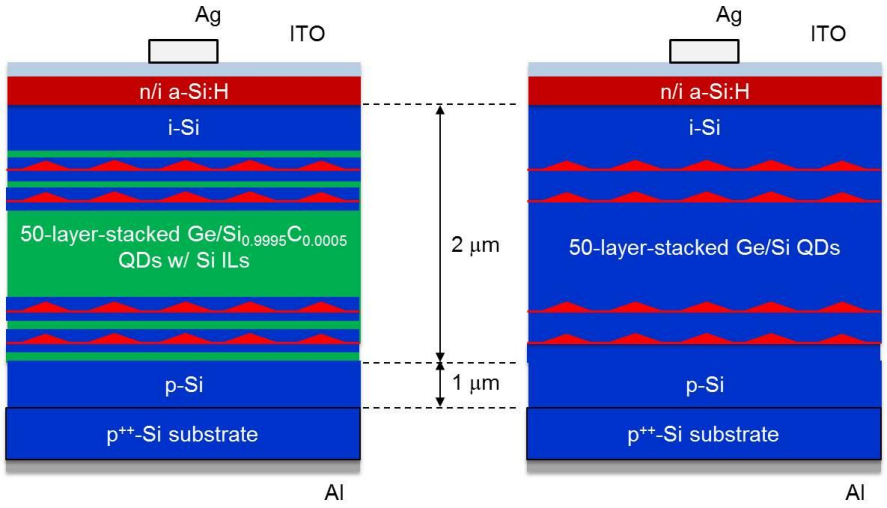

Fig. 6.11: Schematic images of multi-stacked Ge/Si QDSCs. The resistivity of p-Si substrate is 0.01 Ωcm.

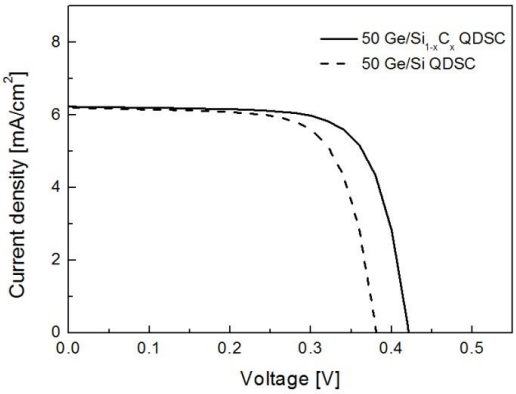

Fig. 6.12: *J-V* curves for 50-layer-stacked $Ge/Si_{0.9995}C_{0.0005}$ QDSCs and Ge/Si QDSCs.

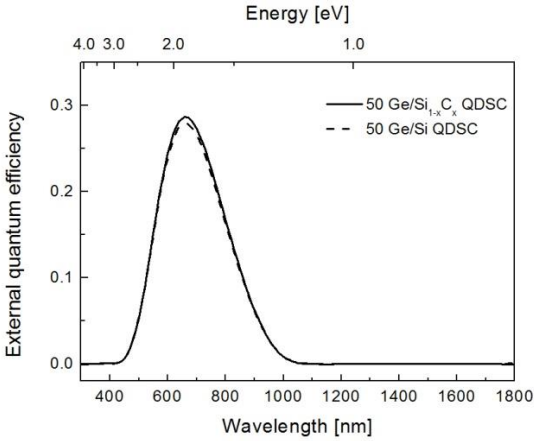

Fig. 6.13: EQE spectra for 50-layer-stacked $Ge/Si_{0.9995}C_{0.0005}$ QDSCs Ge/Si QDSCs.

EQE measurements under bias voltage were performed to confirm transport properties for each sample. The bias voltage was changed from -0.5 to 0.35 V. Figure 6.14 shows EQE spectra for (a) 50-layer-stacked $Ge/Si_{0.9995}C_{0.0005}$ QDSCs and (b) 50-layer-stacked Ge/Si QDSCs under different bias voltage. Generally, reverse bias voltage enhance carrier extraction, while forwards bias voltage suppresses carrier extraction [11]. The EQE response monotonically decreased with increasing bias voltage. Figure 6.15 shows EQE values at 550 nm normalized by the value at -0.5 V for the $Ge/Si_{0.9995}C_{0.0005}$ QDSCs and Ge/Si QDSCs as a function of bias voltage. Smaller decreasing rate of normalized EQE was observed for $Ge/Si_{0.9995}C_{0.0005}$ QDSCs, which means carrier collection became

better in comparison with Ge/Si QDSCs. Furthermore, the decreasing rates at several wavelengths are plotted in Fig. 6.16. The decreasing rates for Ge/$Si_{0.9995}C_{0.0005}$ were smaller than that for Ge/Si QDSCs from 550 to 850 nm. Additionally, the decreasing rates at shorter wavelength were larger value than longer wavelength. The penetration lengths of light in Si are about 1 μm and 10 μm for wavelength at 550 nm and 850 nm [12], respectively, which indicates light at wavelength of 550 nm mainly generate carriers in Ge QDs region, while 850 nm light are able to generate electrons and holes in deeper region. By taking into account this, photo-generated holes chiefly recombine on the way to p-layer by trap in Ge QDs. These results indicate that the transport of holes was improved by introducing $Si_{0.9995}C_{0.0005}$ layers and thus the solar cells properties became better.

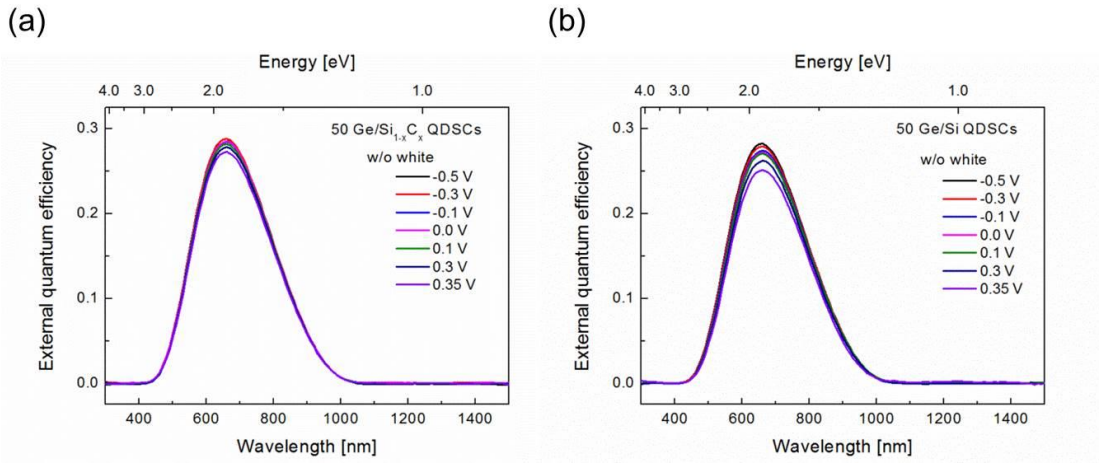

Fig. 6.14: EQE spectra for (a) 50-layer-stacked Ge/$Si_{0.9995}C_{0.0005}$ QDSCs and (b) 50-layer-stacked Ge/Si QDSCs under different bias voltage.

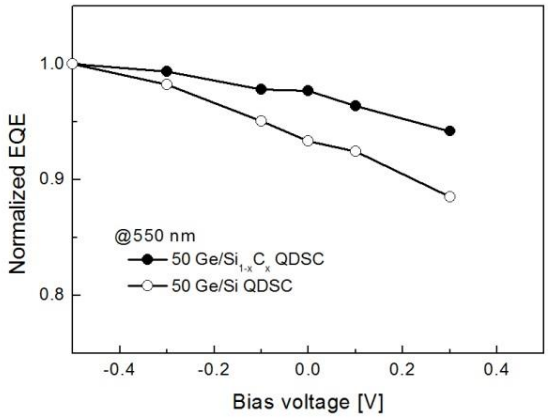

Fig. 6.15: Dependence of EQE values at 550nm on bias voltage. The EQE values are normalized by the value at bias voltage of -0.5 V.

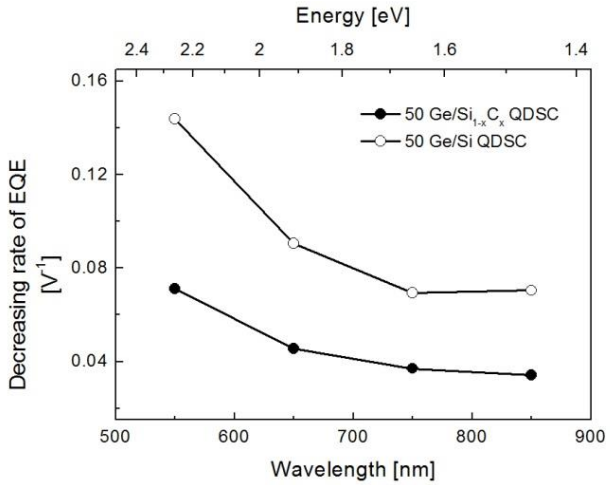

Fig. 6.16: Decreasing rate of EQE at several wavelength.

6.6. Dependence on spacer layer thickness

Finally, the author investigated the dependence of Ge/$Si_{0.9995}C_{0.0005}$ QDSCs properties on spacer layer thickness. Figure 6.17 shows schematic structure of 20-layer-stackied Ge/$Si_{0.9995}C_{0.0005}$ QDSCs with different spacer layer thickness. The spacer layer thickness (d_{SL}) including 2 nm-thick Si ILs was changed from 6 to 20 nm so the layer thickness of $Si_{0.9995}C_{0.0005}$ spacers was equal to (d_{SL} - 4) nm. The total layer thickness of intrinsic epitaxial layers was fixed to 1 μm to obtain same value of built-in potential. The 20-layer-stacked Ge QDs were inserted in middle part of the intrinsic epitaxial layers. Figure 6.18 (a) shows *J-V* curves of the 20-layer-stackied Ge/$Si_{0.9995}C_{0.0005}$ QDSCs with d_{SL} = 6, 10 and 20 nm as well as that of 1 μm-thick epi-Si SCs as a reference. The J_{SC}, V_{OC}, FF and η were plotted as a function of spacer layer thickness in Fig 6.18 (b). Figure 6.19 shows EQE responses of the 20-layer-stacked Ge/$Si_{0.9995}C_{0.0005}$ QDSCs with different spacer layer thickness. The parameters of solar cells and EQE responses were slightly improved by employing thinner d_{SL}, however they were not significantly dependent on d_{SL}.

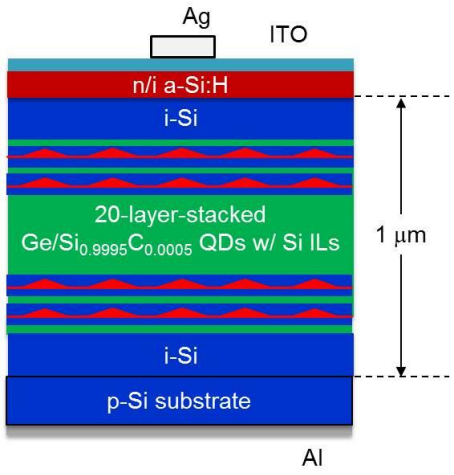

Fig. 6.17: Schematic structure of 20-layer-stacked Ge/$Si_{0.9995}C_{0.0005}$ QDSCs. The resistivity of p-Si substrate is 2 Ωcm.

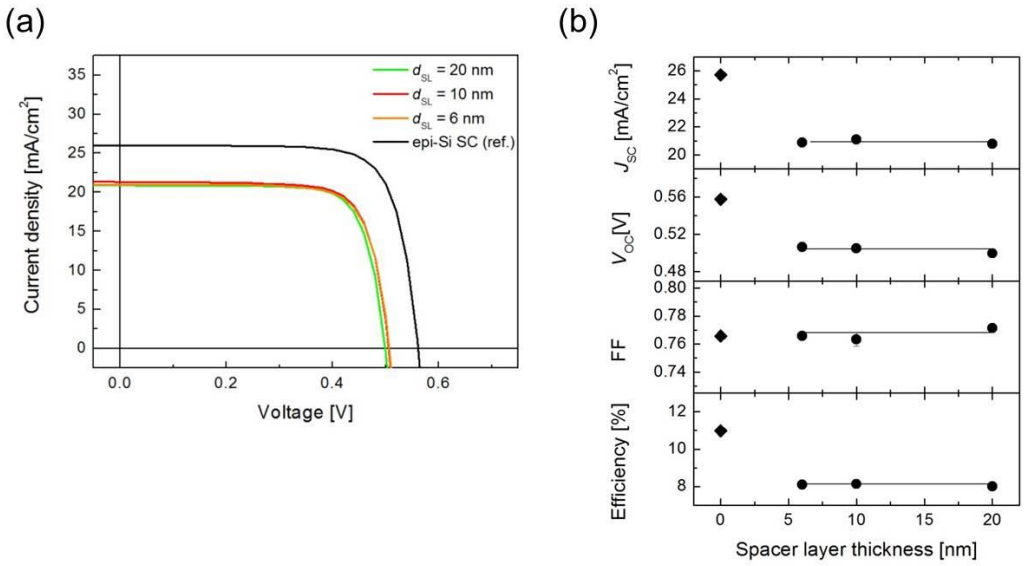

Fig. 6.18: (a) *J-V* curves for multi-stacked Ge/$Si_{0.9995}C_{0.0005}$ QDSCs with d_{SL} = 6, 10, 20 nm, and epitaxially grown 1 μm-thick Si solar cells as a reference. (b) Dependence of solar cell parameters of the QDSCs on spacer layer thickness.

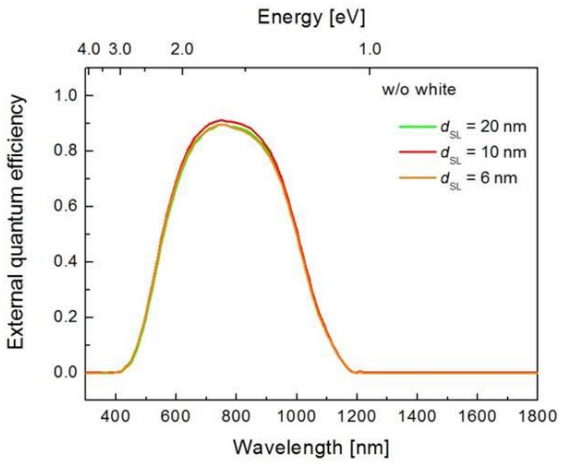

Fig. 6.19: EQE responses of 20-layer-stacked Ge/$Si_{0.9995}C_{0.0005}$ QDSCs with d_{SL} = 6, 10 and 20 nm.

For characterization of carriers transport in 20-layer-stacked Ge/$Si_{0.9995}C_{0.0005}$ QDSCs with different d_{SL}, dependence of the solar cells on bias voltage was investigated. Figure 6.20 shows EQE response of 20-layer-stacked Ge/$Si_{0.9995}C_{0.0005}$ QDSCs with d_{SL} = (a) 6, (b) 10 and (c) 20 nm under different bias

voltage. The bias voltage was changed from -0.5 to 0.45 V. With increasing bias voltage, the EQE response hardly changed in range of reverse bias voltage and decreased from forwards bias of 0.4 V, since weaken built-in potential by forwards bias voltage. Figure 6.21 shows dependence of EQE value of the solar cells at 750 nm on bias voltage. The EQE values were normalized by the value at -0.5 V. The pronounced difference was observed at bias voltage of 0.45 V. The EQE responses at 0.45 V are shown in Fig. 6.22. Decrease in EQE response was suppressed at forward bias voltage of 0.45 V by employing thinner spacer layer thickness, which indicates improvement of carrier collection. This might be caused by better transport of holes due to electronic coupling between QDs. The inter-dot spacing is 4 nm for Ge QDSCs with d_{SL} = 6, which is enough thin to occur electronic coupling between QDs. Although increase in J_{SC} is expected for the samples with d_{SL} = 6 nm due to improved collection of carriers generated in Ge QDs, pronounced increase in J_{SC} were not observed. The author thinks that these results arose from few photo-generated carriers by optical transition via energy levels of Ge QDs and increase in recombination of photo-generated carriers in Ge QDs. PL emission peak from Ge QDs were observed at ~0.8 eV (~1550 nm) in Fig. 5.19, however there was no EQE response around 1550 nm, which indicates that absorption is weak and recombination is dominant in Ge QDs. Therefore, even if holes were pumped from energy levels of Ge QDs to VB of Si, the number of holes is small owing to weak absorption and eventually they recombine in Ge QDs.

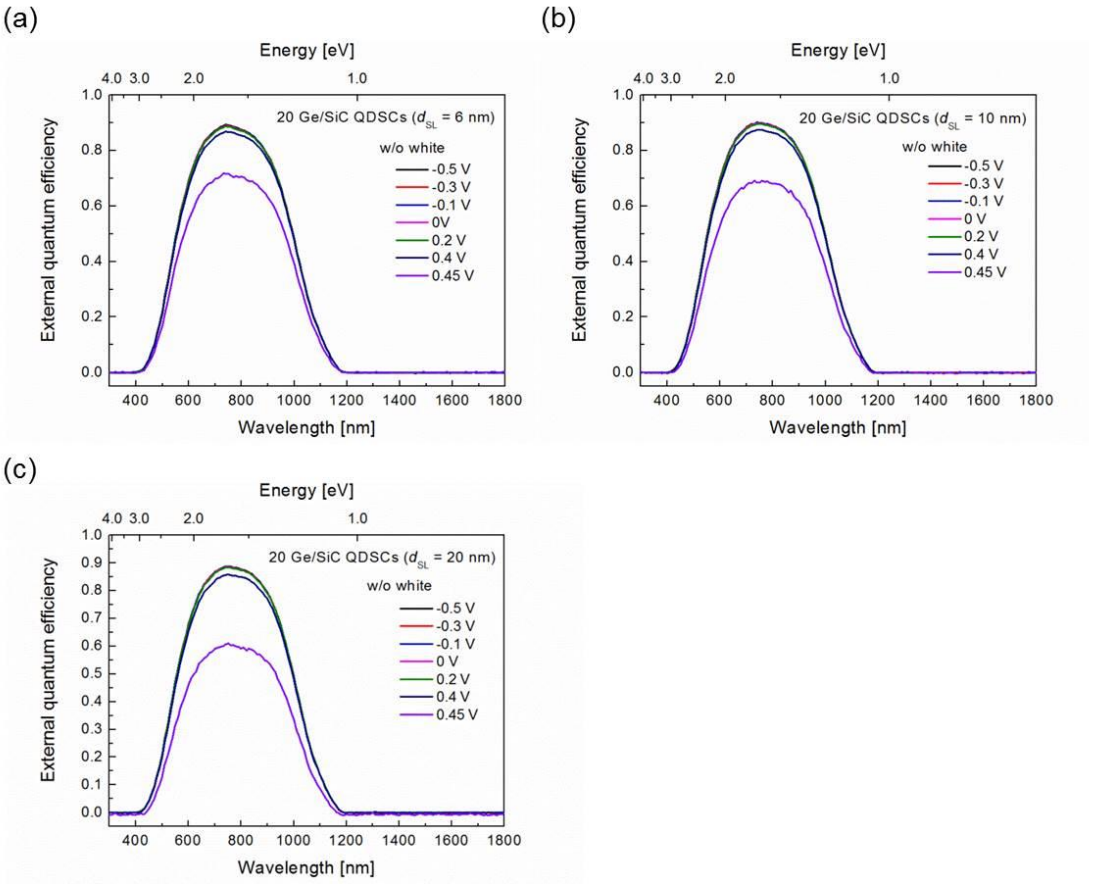

Fig. 6.20: EQE responses of 20-layer-stacked Ge/$Si_{0.9995}C_{0.0005}$ QDSCs with d_{SL} = (a) 6, (b) 10 and (c) 20 nm under different bias voltage.

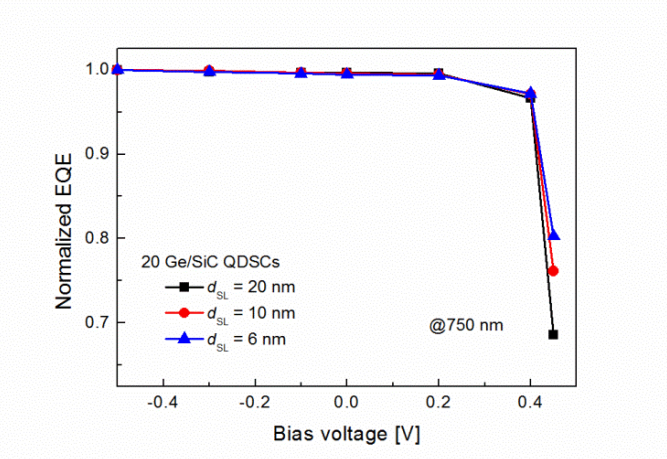

Fig. 6.21: Normalized EQE values of 20-layer-stacked Ge/$Si_{0.9995}C_{0.0005}$ QDSCs with different d_{SL} as a function of bias voltage.

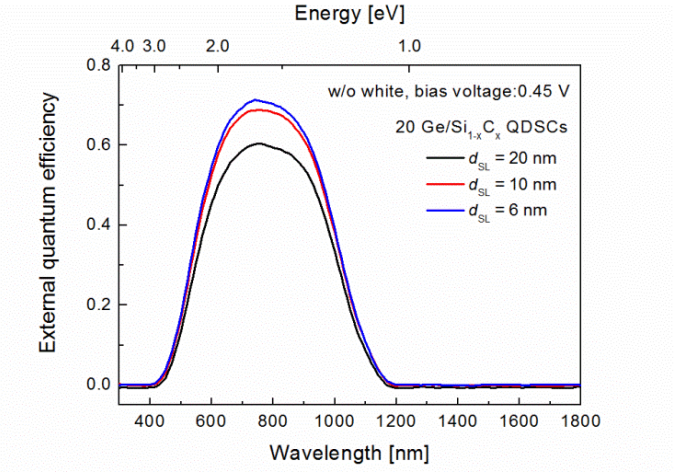

Fig. 6.22: EQE responses of 20-layer-stacked $Ge/Si_{0.9995}C_{0.0005}$ QDSCs with d_{SL} = 20, 10 and 6 nm at bias voltage of 0.45 V.

6.7. Summary

Fabrication and characterization of multi-stacked Ge/Si QDSCs 100-layer-stacked Ge/Si QDSCs were fabricated and slightly increased EQE response in longer wavelength up to 1300 nm was observed for 100-layer-stacked Ge/Si QDSCs. The solar cells performance, however, became worse. To clarify the degradation of solar cells properties, number of stacks was changed from 25 to 100 layers. The solar cells parameters decreased with increasing number of stacks. PL measurements and EQE measurements with bias voltage revealed that the degradation of solar cells caused by recombination in Ge QDs. Furthermore, effect of IR irradiation on the QDSCs was investigated and larger ΔEQE were obtained for 100-layer-stacked QDSCs in comparison with Si reference SCs due to enhancement of escape of carriers from Ge QD layer. Next, solar cells properties for 50-layer-stacked $Ge/Si_{0.9995}C_{0.0005}$ QDSCs were investigated. Improved transport properties of holes were observed for 50-layer-stacked $Ge/Si_{0.9995}C_{0.0005}$ QDSCs by EQE measurements under bias voltage and thus solar cells properties were improved slightly. Finally, the author studied on the effect of spacer layer thickness on the properties of 20-layer-stacked $Ge/Si_{0.9995}C_{0.0005}$ QDSCs. Though it is expected that the properties of solar cells are improved thanks to electric coupling between QDs for the sample with inter-dot spacing of 4 nm, the SC properties were independent of spacer layer thickness probably due to few photo-generated carriers using energy levels of Ge QDs and dominant recombination process in Ge QD layers.

References

[1] L. Korte, E. Conrad, H. Angermann, R. Stangl, M. Schmidt: Sol. Energy Mater. Sol. Cells **93** (2009) 905–910.

[2] H. Fujiwara and M. kondo: Appl. Phys. Lett. **90**, 013503 (2007).

[3] M. Tanaka, M. Taguchi, T. Matsuyama, T. Sawada, S. Tsuda, S. Nakano, H. Hanafusa, and Y. Kuwano: Jpn. J. Appl. Phys. **31** (1992) 3518-3522.

[4] T. Sugaya, Y. Kamikawa, S. Furue, T. Amano, M. Mori, and S. Niki: Sol. Energy. Mater. Sol. Cells 95 (2011) 163-166.

[5] R. Oshima, A. Takata, Y. Shoji, K. Akahane, and Y. Okada: Physica E **42** (2010) 2757-2760.

[6] S. M. Hubbard, C. D. Cress, C. G. Bailey, R. P. Raffaelle, S. G. Bailey, and D. M. Wilt: Appl. Phys. Lett. **92** (2008) 123512.

[7] S. A. Blockhin, A. V. Sakharov, A. M. Nadtochy, A. S. Pauysov, M. V. Maximov, N. N. Ledentsov, A. R. Kovsh, A. R. Kovsh, S. S. Mikhrin, V. M. Lantratov, S. A. Mintairov, N. A. Kaluzhiny, and M. Z. Shvatts: Semiconductors. **43** (2009) 514-518.

[8] Z. Liu, T. Zhou, L. Li, Y. Zuo, C. He, C. Li, C. Xue, B. Cheng, and Q. Wang: Appl. Phys. Lett. **103** (2013) 082101.

[9] A. Alguno, N. Usami, K. Ohdaira, W. Pan, M. Tayanagi, and K. Nakajima: Thin Solid Films **508** (2006) 402-405.

[10] T. Tayagaki, N. Usami, W. Pan, Y. Hoshi, K. Ooi, and Y. kanemitsu: Appl. Phys. Lett. **101** (2012) 133905.

[11] S. M. Sze and Kwok K. NG: *Physics of Semiconductor Devices* (Wiley,) 3rd edition, chapter 2.

[12] S. M. Sze and Kwok K. NG: *Physics of Semiconductor Devices* (Wiley,) 3rd edition, chapter 1.

Chapter 7. General Discussion

In this chapter, experimental results and conclusions obtained in each subject are overviewed and generally discussed in terms of growth, material properties and device performance. The purpose of this study is to examine the possibility of intermediate band solar cells utilizing quantum dots. To this end, there are three important interim target; first formation of dense, uniform and high quality nano-dots with a target diameter of ~30 nm, second the proof of formation of intermediate band by nano-dots and lastly the proof of operation of intermediate band solar cells.

For fabrication of Ge/Si QD-IBSCs, it was found that dense and uniform QDs with thinner spacer layer thickness are favored to absorb sufficient photons in QDs and form minibands. At first, we have developed a pulse growth method for dense and uniform self-assembled Ge/Si QDs. In general, Ge/Si QDs show density of 10^9 cm^{-2} and poor uniformity caused by bimodal size distribution of nano-dots. The bimodal size distribution arises from energetically favored shape of QDs depending on QD volume. Denser Ge/Si QDs were grown at lower temperature due to suppression of migration. At 500 °C and deposition rate of 0.2 Å/s, however, size distribution was still bimodal. We found that with increasing deposition rate bimodal size distribution disappeared and unimodal size distribution was observed at 2.8 Å/s. Higher deposition rate leads to higher concentration of adatoms on surface, which suppresses migration of adatoms. Hence, QDs with height of ~2 nm and lateral size of ~30 nm with high density of ~5×10^{10} cm^{-2} and high uniformity of 11% were obtained. The lateral QD size is much larger than height so the fabricated Ge QDs work quantm well like dots due to small carrier confinement energy of 13 meV in the lateral direction.

The author, next, fabricated multi-stacked Ge QDs in Si matrix. High quality Ge QDs with high density (areal density: ~5×10^{10} cm^{-2}) and better uniformity (fluctuation in lateral size: ~12 %) were fabricated by using pulse growth method composed of high deposition rate of 2.8 Å/s and growth

interruption for 5 seconds. In order to avoid mechanical strain in multi-stacked Ge/Si QDs, relatively thick (30 nm) Si spacer layer is needed for 100-layer stacked QDs without deterioration of crystal quality. We conclude that this newly developed growth method helps to fabricate highly-stacked Ge/Si QD structure when thicker spacer layer thickness is thicker than 30 nm. As far as the author knows, highly-stacked Ge/Si QDs without significant size change and deterioration of crystal quality is achieved for the first time.

Next, we grew $Si_{1-x}C_x$ layer on Si(001) substrates for strain-compensated, multi-stacked QDs with thin spacer layer thickness. Thinner spacer layer thickness in multi-stacked Ge/Si QD structure generates stronger strain fields induced by buried Ge QDs, resulting in an increase in QD size and aggregation of QDs. The compressive stress established by Ge QDs is compensated by tensile stress in $Si_{1-x}C_x$ spacer layer. In growth of $Si_{1-x}C_x$ layers on Si(001), although we changed C flux by increasing C sublimation cell temperature and ratio of C to Si flux by decreasing Si deposition rate, C incorporation was limited to x = 0.0005 possibly due to small thermal equilibrium solubility of C into Si of the order of 10^{17} atoms/cm^3.

Then, we fabricated Ge QDs on $Si_{0.9995}C_{0.0005}$ by employing the pulse growth technique. The nucleation process of Ge nano-dots on strained $Si_{1-x}C_x$ layer influence the optimum deposition rate for uniform QD formation and the deposition rate was reduced from 2.8 Å/s to 2.6 Å/s. The nucleation process could be influenced by restricted nucleation site induced by repulsion of Ge adatoms by C atoms. Furthermore, multi-stacked Ge/$Si_{0.9995}C_{0.0005}$ QDs showed deterioration of optical properties. The cross-sectional STEM images indicates the interface between Ge and $Si_{0.9995}C_{0.0005}$ was rough. Thereupon, we employed Si interlayers (ILs) in between Ge/$Si_{0.9995}C_{0.0005}$ interface to improve the interface roughness. The interface became smoother by sandwiching $Si_{1-x}C_x$ by 2 nm-thick Si ILs and thus the optical property was improved. It is thought that termination of C atoms by Si helps to grow multi-stacked Ge/$Si_{0.9995}C_{0.0005}$ QDs by smoothing Ge/$Si_{0.9995}C_{0.0005}$ interface. However, crystal quality

of Ge/$Si_{0.9995}C_{0.0005}$ QDs with 2 nm-thick Si ILs was not comparable to that of Ge/Si. The Si related peak became weak so further improvement is still necessary for better crystal quality.

Additionally, the effect of spacer layer thickness on multi-stacked Ge/$Si_{0.9995}C_{0.0005}$ QDs with Si ILs was studied. The introduction of $Si_{0.9995}C_{0.0005}$ layer prevented Ge QDs from significant increase in QD size as well as aggregation of QDs even at spacer layer thickness of 6 nm. This is due to both weaker strain fields induced by smaller Ge QDs and slightly compensated the strain fields, since smaller QDs create weaker strain fields. However, increase in QD size was still observed from spacer layer thickness less than 10 nm. PL peak energy of Ge QDs redshifted from 0.839 to 0.797 V with decreasing spacer layer thickness from 40 to 6 nm, i.e. the incremental difference of the peak shift was about 40 meV. From numerical calculation, the shift of quantized energy level roughly results in 20 meV by regarding the self-assembled QDs as quantum well, which is not consistent with the experimental value of 40 meV. Increased PL intensity was observed for the samples with spacer layer thickness of 6 nm, which is not related to decrease in density of QDs. This suggests increase in spatially direct transition caused by electric coupling between QDs. The type-II band lineup was confirmed for 20-layer-stacked Ge/$Si_{0.9995}C_{0.0005}$ QDs with 2 nm-thick Si ILs QDs. The larger slope of 5.62 $(meV)^{2/3}$ was observed for sample with 6 nm-thick spacer layer. Similar behavior is observed for electrically coupled InGaAs/GaAs QDs. The 6 nm-thick spacer layer equals to inter-dot spacing of 4 nm, since the height of Ge QDs was 2 nm. It is consistent with onset of minibands formation so the author believes that these results suggest minibands formation in growth direction. For strain compensation in Ge/$Si_{1-x}C_x$ QD structure, C content of about 3% is necessary at spacer layer thickness of 6 nm and its value is different from C content of 0.0005 in this work. To grow dense and uniform QDs with thin spacer layer thickness in group IV material system, following effort is required: better crystal quality, increase in C content of $Si_{1-x}C_x$ spacer layer, and strain engineering to prevent strain fields induced by each QD from superposition.

Finally, the Ge QDs were applied to solar cells. Extended EQE response was observed up to 1300 nm for 100-layer-stacked Ge/Si QDs, while EQE response in shorter wavelength decreased. From dependence of solar cells properties on number of stacks, EQE monotonically decreased. PL emission intensity from Ge QDs monotonically increased even in solar cells, which means crystal quality of multi-stacked Ge/Si QDs in solar cells is maintained. We thought that the J_{SC} of Ge/Si QDSCs, in particular highly-stacked Ge/Si QDSCs, were improved at reverse bias voltage due to enhancement of carrier collection, however it did not changed significantly, which suggests that it is difficult for photo-generated carriers to contribute to current density once carriers are trapped in Ge QDs. The built-in potential of the Ge/Si QDSCs were almost identical since doping concentration of n and p-layer was not changed as well as intrinsic layer thickness. Furthermore, dependence of EQE at several wavelengths on bias voltage was investigated and larger decreasing EQE observed at short wavelength than longer wavelength. Light with shorter wavelength generates carriers in around surface region. Our Ge/Si QD solar cells were n-i-p structures. Therefore, holes are mainly trapped and recombine in Ge QDs on the way to p-layer due to strong confinement energy of Ge QDs for holes.

50-layer-stacked Ge/$Si_{0.9995}C_{0.0005}$ QDSCs were fabricated and compared with 50-layer-stacked Ge/Si QDSCs. Although C content is few, the multi-stacked Ge/$Si_{0.9995}C_{0.0005}$ QDs were firstly fabricated as long as I know. The dependence of EQE on bias voltage was examined and the EQE decreased with increase in bias voltage. The decreasing rate of EQE was improved in Ge/$Si_{0.9995}C_{0.0005}$ QDSCs. Thus, the transport property was improved due to suppression of generation of aggregated Ge islands by the strain compensating $Si_{0.9995}C_{0.0005}$ spacer layer, however the solar cells properties was not significantly improved. We think that one of reasons for the degradation of Ge/Si QDSCs properties arises form obstruction of holes transport. From optical characterization, the multi-stacked Ge QDs were type-II band lineup, which leads to localization of holes in Ge QDs. The alternate

process of trapped holes in Ge QDs and thermal escape process from QDs results in obstruction of carriers transport like hopping conduction.

Furthermore, the effect of spacer layer thickness on solar cells properties was investigated. The parameters of solar cells, particularly short-circuit current density, are expected to be improved due to increase in photo-generated carriers via energy levels of Ge QDs, however the parameters of solar cells were hardly changed. The spacer layer thickness of 6 nm equals to inter-dot spacing of 4 nm since height of Ge QDs was 2 nm, which is thin enough to occur electric coupling between QDs. PL emissions peak of 1500-1600 nm from Ge QDs were observed for as-grown samples, however EQE response around 1550 nm were not observed, which suggests that few holes generated via energy levels of Ge QDs in addition to dominant recombination process caused by confinement of holes in Ge QDs. The author thinks that no pronounced evidence of IB-QDSCs results from weak absorption and dominant recombination process in Ge QDs owing to indirect bandgap semiconductors and strong confinement energy for holes.

Chapter 8. General Conclusion

The fabrication of Ge/Si QDs and Ge/$Si_{1-x}C_x$ QDs for dense and uniform Ge QDs with thinner spacer layer thickness in direction to p-n junction is performed by using solid-source molecular beam epitaxy (SS-MBE), and heterojunction Ge QD solar cells using hydrogenated amorphous Si (a-Si:H) are examined.

Self-assembled Ge QDs on Si with high density of 5×10^{10} cm^{-2} and better uniformity of 11% are grown at low growth temperature of 500 °C and high deposition rate of 2.8 Å/s due to suppression of migration. The height and lateral sized of the Ge QDs are about 2 nm and 30 nm. The flat shape Ge QDs are regarded as quantum well like dots, since the confinement energy in the direction to growth and lateral are roughly 600 meV and 13 meV, respectively.

The shape and crystal quality of multi-stacked Ge QDs with spacer layer thickness of 30 nm are successfully maintained up to 100-layer-stacks by the newly developed growth method consisting of high deposition rate of 2.8 Å/s and growth interruption for 5 seconds. 20-layer-stacked QDs until spacer layer thickness of 10 nm are grown without aggregated Ge islands. The PL peak energy follows third root of excitation power, which indicates that grown Ge/Si QDs possess type-II band lineup. The 20-layer-stacked with spacer layer thickness of 6 nm shows relatively weak PL emission from Ge QDs due to generation of aggregated Ge islands caused by exceeding critical value of the strain accumulated locally around Ge QDs. Hence, the new growth technique is possible to fabricate highly-stacked Ge/Si QDs with relatively thicker spacer layer owing to both weak strain fields induced by each QD and averaged strain fields by thicker spacer layer.

To fabricate multi-stacked Ge QDs with thinner spacer layer thickness for overlapping of wave functions of Ge QDs, we focused on the $Si_{1-x}C_x$ spacer layers which are capable of compensating the compressive stress arisen from Ge QDs by tensile stress in the spacer layer. 20-layer-stacked

$Ge/Si_{0.9995}C_{0.0005}$ QDs possessing spacer layer thickness of 6 nm are fabricated without aggregation of Ge QDs possibly due to both certain fraction of strain compensation and thinner smaller QD size. From optical characterization, the 20-layer-stacked $Ge/Si_{0.9995}C_{0.0005}$ QDs shows type-II band lineup. The redshifted PL peak energy and increased PL intensity are observed for spacer layer thickness of 6 nm. The increase in PL intensity was not related to decrease in areal density so it may results from increase in spatially direct transition accrued form electrically coupled QDs. Furthermore, larger increasing rate of PL peak energy for excitation power is observed for spacer layer thickness of 6 nm. Similar behavior is observed for InGaAs/GaAs QDs employing enough short inter-dot spacing to form miniband. The QD height is 2 nm for the samples with spacer layer thickness of 6 nm, which means the inter-dot spacing is 4 nm. It is possible to occur electric coupling between Ge QDs so the author believes that the wave function overlapping of Ge QDs occur for 20-layer-stacked $Ge/Si_{0.9995}C_{0.0005}$ QDs with spacer layer thickness of 6 nm.

Finally, we investigated how Ge QDs affect the solar cells properties by fabricating hetero-junction Ge QDSCs. 100-layer-stacked Ge/Si QDSCs show extended EQE response to 1300 nm owing to contribution from Ge QD layers. The short-circuit current density J_{SC} decrease with increase in number of stacks due to increased recombination of photo-generated carriers, whereas open circuit voltage V_{OC} was significantly decreased from 0.48 to 0.37 V by inserting Ge QDs and not so strongly depend on number of stacks. Hence, the V_{OC} in QDSCs is determined by quasi Fermi energy between CB of Si and VB of Ge QD probably due to thermal escape of holes in Ge QDs. Additionally, effect of infrared irradiation on solar cells was investigated. The Ge/Si QDSCs show larger ΔEQE defined by subtraction EQE value without IR from with IR possibly due to enhancement of escape process of holes in Ge QDs. Furthermore, transport properties of 50-layer-stacked Ge/Si and $Ge/Si_{0.9995}C_{0.0005}$ QDSCs were studied by EQE under bias voltage and it reveals that photo-generated holes are trapped by Ge QDs and recombine. The 50-layer-stacked $Ge/Si_{0.9995}C_{0.0005}$ QDSCs show better transport properties and hence solar cells properties are slightly improved. From these results, holes are trapped

by Ge QDs on the way to p-layer and thus recombination process become dominant in Ge/Si QDSCs. Furthermore, it was found that suppression of generation of large coalesced QDs can improve the solar cell property. Furthermore, effect of spacer layer thickness was studied for 20-layer-stacked $Ge/Si_{0.9995}C_{0.0005}$ QDSCs. Although inter-dot spacing of 4 nm is enough thin to occur electric coupling between QDs, the solar cells properties are independent of spacer layer thickness. PL emissions peak of 1500-1600 nm from Ge QDs are observed for as-grown Ge QD samples, however EQE response around 1550 nm are not observed, which indicates few holes generated via Ge QDs and recombination process is dominant. It is thought that no pronounced evidence results from weak absorption accrued form indirect material system and quantum well like Ge dots.

Further increase in number of stacks is necessary as well as decrease in spacer layer thickness to enhance absorption in Ge QD layers and stronger built-in potential for solar cells application, respectively. It, however, is difficult to achieve both increase in number of stacks and decrease in epitaxial layer thickness. So the author believes that QD materials with strong absorption coefficient and type-II band lineup are promising for QD solar cell applications. In a different method, installation of down and/or up-convertors in outside of solar cells could be better way to increase in J_{SC} without decrease in V_{OC}.

Achievement

List of Publications

1. "Strain-compensated Ge/$Si_{1-x}C_x$ quantum dots with Si mediating layers grown by molecular beam epitaxy", **K. Gotoh**, R. Oshima, T. Sugaya, I. Sakata, K. Matsubara, M. Kondo, Journal of Crystal Growth, vol 425, pp. 167-171, (2015).
2. "Effect of deposition rate on the characteristics of Ge quantum dots on Si(001) substrates", **K. Gotoh**, R. Oshima, T. Sugaya, I. Sakata, K. Matsubara, M. Kondo, Thin Solid Films, vol.557, pp.80-83, (2014).
3. "Optical and structural studies of highly uniform Ge quantum dots on Si(001) substrate grown by solid-source molecular beam epitaxy", **K. Gotoh**, R. Oshima, T. Sugaya, I. Sakata, K. Matsubara, M. Kondo, Journal of Crystal Growth, vol.378, pp.439-441, (2013).

Proceedings

1. "Fabrication of type-II self-assembled Ge/Si quantum dots for high efficiency solar cells", **K. Gotoh**, R. Oshima, T. Sugaya, I. Sakata, K. Matsubara, M. Kondo, 28th EUPVSEC proceedings, pp.147-150, (2013).

Conference Presentations

[International (Oral)]

1. "Studies on highly stacked Ge/Si quantum dot heterojunction solar cells grown with up to 100 stacked layers", **K. Gotoh**, R. Oshima, I. Sakata, K. Matsubara, T. Sugaya, M. Kondo, 25th International Photovoltaic Science and Engineering Conference Global Photovoltaic Conference 2015 Busan (Korea) (2015.11).

2. “Fabrication of type-II self-assembled Ge/Si quantum dots for use in high efficiency solar cells”, **K. Gotoh**, R. Oshima, T. Sugaya, I. Sakata, K. Matsubara, M. Kondo, Japanese-German Students Symposium on Material Science, Magdeburg (Germany), (2014. 3)
3. “Fabrication of Type-II Self-Assembled Ge/Si Quantum Dots for High Efficiency Solar Cells”, **K. Gotoh**, R. Oshima, T. Sugaya, I. Sakata, K. Matsubara, M. Kondo, 28th European PV Solar Energy Conference and Exhibition, Paris (France), (2013. 9-10)

[International (Poster)]

1. “Optical and structural studies on highly uniform Ge quantum dots on Si (001) substrate by solid source molecular beam epitaxy”, **K. Gotoh**, R. Oshima, T. Sugaya, I. Sakata, K. Matsubara, M. Kondo, The 18th international conference on Molecular Beam Epitaxy, Flagstaff (USA), (2014. 9)
2. “Effect of deposition rate on the characteristics of Ge quantum dots on Si (001) substrate”, **K. Gotoh**, R. Oshima, T. Sugaya, I. Sakata, K. Matsubara, M. Kondo, The 8th international conference on Silicon epitaxy and heterostructures, Fukuoka (Japan) (2013. 6)
3. “Optical and structural studies on highly uniform Ge quantum dots on Si (001) substrate by solid source molecular beam epitaxy”, **K. Gotoh**, R. Oshima, T. Sugaya, I. Sakata, K. Matsubara, M. Kondo, The 17th international conference on Molecular Beam Epitaxy, Nara (Japan), (2012. 9)

[Domestic (Oral in Japanese)]

1. 「歪み補償系積層 $Ge/Si_{1-x}C_x$ 自己形成量子ドットの構造評価」，**後藤和泰**，大島隆治，菅谷武芳，坂田功，松原浩司，近藤道雄，第 75 回応用物理学会秋季学術講演会，北海道，(2014.9)

2. 「太陽電池応用へ向けたタイプ II 型自己形成 Ge/Si 量子ドットの作製」，**後藤和泰**，大島隆治，菅谷武芳，坂田功，松原浩司，近藤道雄，SAT テクノロジー・ショーケース 2014，北海道，(2014.1)
3. 「タイプ II 型 Ge 量子ドットの近接化と太陽電池応用」，**後藤和泰**，大島隆治，菅谷武芳, 坂田功, 松原浩司, 近藤道雄，第 74 回応用物理学会秋季学術講演会，京都, (2013.9)
4. 「パルス成長法による高均一自己形成 Ge 量子ドットの高密度化」，**後藤和泰**，大島隆治, 菅谷武芳, 坂田功, 松原浩司, 近藤道雄，第 73 回応用物理学会秋季学術講演会，愛媛，(2012.9)
5. 「MBE 法による Si(001)基板上高均一 Ge 自己形成量子ドットの作製」，**後藤和泰**，大島隆治，菅谷武芳，坂田功，松原浩司，近藤道雄，第 59 回応用物理学会春季学術講演会，東京，(2012.3)

[Domestic (Poster in Japanese)]

1. 「タイプ II 型 Ge/Si 量子ドットを導入したヘテロ接合型太陽電池の作製」，**後藤和泰**，大島隆治，菅谷武芳，坂田功，松原浩司，近藤道雄，第 5 回薄膜太陽電池セミナー，名古屋，(2013.11)
2. 「Si(001)基板上自己形成 Ge 量子ドットの堆積速度依存性」，**後藤和泰**，大島隆治，菅谷武芳，坂田功，松原浩司，近藤道雄，第 59 回応用物理学会春季学術講演会，東京，(2013.3)
3. 「IV 族材料系量子ドット型太陽電池へ向けた Ge 自己形成量子ドットの作製」，**後藤和泰**，大島隆治，菅谷武芳，坂田功，松原浩司，近藤道雄，第 3 回薄膜太陽電池セミナー，埼玉，(2011.10)

Acknowledgement

This study was performed in Research Center for Photovoltaics (RCPV) of National Institute of Advanced Industrial Science and Technology (AIST).

In the first place, the author would like to thank Professor Michio Kondo for giving opportunity for this study and instructing me.

The author also would like to express my sincere appreciation to Professor Osamu Odawara and associate professor Hiroyuki Wada for helpful advices in seminar and supporting my school life.

The author would like to express gratitude for the help and support of research scientists in RCPV. In particular, I would like to express great thank for research scientist Ryuji Oshima for experimental help and instruction. Furthermore, I also would like to acknowledge leader of smart stack device team, Takeyoshi Sugaya, and member of research scientist Takeshi Tayagaki for experimental support and precious opinions. The author acknowledge leader of RCPV Koji Matsubara and research scientist Isao Sakata for helpful discussion. This thesis owes existence thanks to their contributions.

The author K.G. is a research fellow of Japan society for the Promotion of Science (JSPS) and part of this study is supported by JSPS.

Finally, the author would like to thank my mother, sister, and grandfather.